

Nearly Degenerate Majorana Dark Matter and Its Self-Interactions in a Gauged $U(1)_{L_\mu-L_\tau}$ Model

Kwei-Chou Yang^{1,*}

¹*Department of Physics and Center for High Energy Physics,
Chung Yuan Christian University, 200 Chung Pei Road, Taoyuan 32023, Taiwan*

We propose a model of nearly degenerate Majorana dark matter (DM) in a gauged $U(1)_{L_\mu-L_\tau}$ extension of the Standard Model. Spontaneous symmetry breaking generates a dominant Majorana mass via a strong Yukawa coupling, splitting the dark fermion into two nearly degenerate states. The lighter state (χ_-) is the DM candidate, with an allowed mass of ~ 10 GeV to several hundred GeV. Crucially, within the $10 \sim 75$ GeV mass range and a scalar mediator at the tens of MeV scale, this strong coupling dictates the thermal relic abundance and induces significant elastic self-interactions. These self-interactions naturally resolve small-scale structure anomalies, such as the core-cusp problem, while satisfying massive cluster constraints. Furthermore, we place stringent joint constraints on the scalar mass and the Higgs mixing angle α using the latest LZ 2025 direct detection data. The model's gauge boson Z' maintains early-Universe thermal equilibrium and accommodates the muon anomalous magnetic moment $(g-2)_\mu$, remaining consistent with updated cosmological and experimental bounds.

arXiv:2512.05694v2 [hep-ph] 2 Mar 2026

* kcyang@cycu.edu.tw

I. INTRODUCTION

The dark sector may possess a rich structure, potentially consisting of multiple particle states with extremely small mass differences—a scenario characterized by nearly degenerate dark matter. When interactions predominantly induce transitions between these closely spaced mass eigenstates, the framework is widely referred to as inelastic dark matter. This mechanism was originally proposed to reconcile discrepancies among early direct-detection experiments such as DAMA and CDMS [1, 2]. Since then, research on models featuring nearly degenerate dark states has expanded across a broader range of areas, including direct and indirect detection methods, particle physics experiments, and astronomical observations, as well as explanations and predictions of the Universe’s evolution [3–25].

A well-known example featuring such a small mass splitting is pseudo-Dirac fermion dark matter [6, 11, 14, 20, 22–24]. In a minimal $U(1)$ gauge extension, the dark sector typically comprises a Dirac fermion with mass m_D and a complex scalar. A weak Yukawa coupling f connects the dark fermions to the scalar. Upon spontaneous symmetry breaking (SSB) of the $U(1)$ symmetry, the scalar acquires a vacuum expectation value v_S , generating a small Majorana mass term $\sim f v_S$. Consequently, the original Dirac fermion splits into two nearly degenerate Majorana eigenstates with masses $m_D \pm f v_S$. However, producing a tiny mass splitting in this pseudo-Dirac scenario generally restricts the coupling f to be extremely small, severely limiting the phenomenological richness of the dark sector, particularly regarding DM self-interactions.

In this work, we propose a novel and phenomenologically rich model of nearly degenerate Majorana DM that naturally connects key astrophysical observations with various direct, indirect, and particle experimental constraints. In contrast to the pseudo-Dirac paradigm, our dark sector features fermions (χ, χ^c) with a very small Dirac mass m_D and a complex scalar S . Here, we introduce a strong Yukawa coupling f between the dark fermions and the scalar. After SSB, this large coupling generates a dominant Majorana mass $f v_S$, splitting the dark fermions into two nearly degenerate Majorana states with masses $f v_S \pm m_D$. The lighter Majorana eigenstate (χ_-) serves as the primary DM candidate, while the heavier state (χ_+) may also be present depending on its lifetime and the cosmic environment.

In our framework, the dark matter is significantly heavier than the light scalar mediator ($m_\chi \gg m_S$). Driven by the strong Yukawa coupling f , dark matter annihilations into the light S and Z' final states dominate the freeze-out process and dictate the relic abundance. Moreover, the light scalar induces strong dark matter self-interactions that transfer heat outward within galactic halos,

effectively alleviating core density problems [26–28].

Before symmetry breaking, our dark sector respects a $U(1)_{L_\mu-L_\tau}$ gauge symmetry. This represents the simplest Standard Model (SM) extension accommodating nearly degenerate Majorana dark matter while remaining anomaly-free. Since the SM muon and tau doublets carry opposite charges under this symmetry, the gauge boson Z' couples to them [29–42]. Historically, this interaction was proposed to address the $(g-2)_\mu$ anomaly. However, recent updates to the SM prediction [43] align well with experimental data [44–48], thereby imposing stringent upper bounds on the Z' mass and its coupling to muons. Consequently, we use these robust new limits to determine the allowed parameter space for our model, and we will review the current experimental constraints on this space in detail.

Crucially, despite these restricted, tiny gauge couplings for the dark sector and leptons ($\lesssim 10^{-3}$), S and Z' successfully remain in thermal equilibrium with the SM bath via $S \leftrightarrow Z'Z'$ and $Z' \leftrightarrow \nu_{\mu,\tau}\bar{\nu}_{\mu,\tau}$ until dark matter freeze-out. Consequently, thermalization does not require a large scalar mixing angle α with the SM Higgs. This naturally accommodates extremely small α values, which we evaluate against severe joint constraints on the (m_S, α) parameter space from recent LZ 2025 direct detection data [49]. Furthermore, high-scale kinetic mixing between the Z' and the photon ensures that, even after standard weak interactions decouple, the electromagnetic plasma (γ, e^\pm) temporarily maintains thermal contact with the neutrino sector via $e^+e^- \leftrightarrow Z'$. This extended equilibrium subsequently alters the effective number of relativistic species (N_{eff}), offering a potential pathway to alleviate the cosmological Hubble tension.

While both our framework and standard pseudo-Dirac models generate two nearly degenerate Majorana states after symmetry breaking, their underlying mass mechanisms and gauge interactions are fundamentally different. In pseudo-Dirac models, the dark matter mass is dominated by an initial Dirac term. This leads to gauge interactions governed by an inelastic vector current ($\bar{\chi}_+\gamma_\mu\chi_-$), which largely preserves macroscopic Dirac-like phenomenology. In contrast, the eigenmasses in our model are predominantly generated by the Majorana mass term following spontaneous symmetry breaking (SSB). Consequently, the Z' boson couples to the dark sector via an inelastic axial-vector current ($\bar{\chi}_+\gamma_\mu\gamma_5\chi_-$), a distinct signature of its true Majorana nature. To accurately reflect this dominant mass origin and the strictly off-diagonal axial-vector interactions, we refer to our framework as the nearly degenerate Majorana dark matter model.

Finally, our nearly degenerate mass spectrum heavily suppresses the decay width of the heavier state χ_+ . Unlike the specific pseudo-Dirac setup in Ref. [32], where the heavier state decays promptly due to a large mass splitting, our scenario necessitates a precise tracking of the χ_+

residual abundance and its macroscopic lifetime. Furthermore, we analyze the impact of gauge kinetic mixing generated at high energy scales on the effective number of relativistic species (N_{eff}), offering a potential pathway to alleviate the Hubble tension.

The rest of this paper is organized as follows. In Sec. II, we detail the nearly degenerate Majorana $U(1)_{L_\mu-L_\tau}$ model, with eigenstate derivations deferred to Appendix A. Sec. II C addresses the gauge mixing between the Z' and SM neutral bosons at both high-energy and one-loop levels. We also derive the resulting interaction Lagrangian, providing detailed calculations in Appendix B. Sec. III then defines the independent parameters of our framework.

Sec. IV explores the parameter space constrained by the $(g-2)_\mu$ measurement and other relevant experiments. In Sec. V, we examine the thermal evolution of the dark sector, focusing on the constraints when annihilations into SS , $Z'Z'$, and SZ' dominate. Sec. VI investigates the model's predictions for N_{eff} and its potential to alleviate the Hubble tension. Sec. VII analyzes how the mass splitting and the lifetime of the excited state affect its residual relic abundance.

Sec. VIII incorporates the Sommerfeld enhancement to evaluate its impact on the relic abundance and indirect detection signatures. In Sec. IX, we analyze the experimental bounds on the scalar mixing angle α . Sec. X discusses dark matter self-scattering and its role in addressing small-scale structure challenges. In Sec. XI, we review additional experimental probes capable of testing this nearly degenerate Majorana DM scenario. We conclude with a summary in Sec. XII. Further details and relevant formulas are included in the Appendices.

II. DESCRIPTION OF THE NEARLY DEGENERATE MAJORANA DARK MATTER MODEL

We consider a minimal extension of the nearly degenerate Majorana DM model for which the dark sector is gauged under a local $U(1)_{L_\mu-L_\tau}$ symmetry with a gauge boson Z' . Meanwhile, the SM μ and τ sectors can interact with the dark sector by exchanging the gauge boson Z' associated with the $L_\mu - L_\tau$ symmetry,

$$\mathcal{L} \supset -g_{\mu\tau} Z'_\mu J_{L_\mu-L_\tau}^\mu, \quad (1)$$

with

$$J_{L_\mu-L_\tau}^\mu = \bar{\mu}\gamma^\mu\mu - \bar{\tau}\gamma^\mu\tau + \bar{\nu}_{\mu L}\gamma^\mu\nu_{\mu L} - \bar{\nu}_{\tau L}\gamma^\mu\nu_{\tau L}, \quad (2)$$

where $g_{\mu\tau}$ is the gauge coupling constant associated with the Z' boson. Under the $U(1)_{L_\mu-L_\tau}$ symmetry, the muon and tau sectors carry charges of $+1$ and -1 , respectively. We assume the

	$SU(2)_L$	$U(1)_Y$	$U(1)_{L_\mu-L_\tau}: q_{L_d}$
$L_\mu = (\nu_\mu, \mu_L)$	2	-1/2	1
$L_\tau = (\nu_\tau, \tau_L)$	2	-1/2	-1
μ_R	1	-1	1
τ_R	1	-1	-1
ϕ_H	2	1/2	0
χ	1	0	q_d
ϕ_S	1	0	$2q_d$

TABLE I. Charge assignments, where the generic $U(1)_{L_\mu-L_\tau}$ charge is denoted as q_{L_d} .

dark sector contains a vector-like Dirac fermion χ and a Higgs-like complex scalar ϕ_S with the $U(1)_{L_\mu-L_\tau}$ charge assigned to be $+q_d$ and $+2q_d$, respectively. The charge assignments for all relevant particles are summarized in Table I.

In the following subsections, we will separately discuss (i) the mixing of the dark scalar and SM Higgs, (ii) the dark Majorana mass eigenstates and their interactions, and (iii) the possible kinetic mixing between Z' and SM neutral gauge bosons, Z and A (photon).

A. The Higgs sector

The Higgs portal may hint at the dark sector interacting with SM particles owing to mixing between the dark scalar ϕ_S and the SM Higgs doublet ϕ_H . The relevant Lagrangian is described by

$$\mathcal{L}_{\text{Higgs}} = (D_\mu \phi_H)^\dagger D^\mu \phi_H + (D_\mu \phi_S)^\dagger D^\mu \phi_S - V(\phi_H, \phi_S), \quad (3)$$

where $D_\mu \phi_{S,H} = (\partial_\mu + iq_{S,H} g_{\mu\tau} Z'_\mu) \phi_{S,H}$ with $U(1)_{L_\mu-L_\tau}$ charges $q_H = 0$ and $q_S = 2q_d$, and with $q_S g_{\mu\tau} \equiv 2g_\chi$. Here, the potential is given by

$$V(\phi_H, \phi_S) = -\mu_H^2 \phi_H^\dagger \phi_H + \lambda_H (\phi_H^\dagger \phi_H)^2 - \mu_S^2 \phi_S^\dagger \phi_S + \lambda_S (\phi_S^\dagger \phi_S)^2 + \lambda_{SH} (\phi_S^\dagger \phi_S) (\phi_H^\dagger \phi_H). \quad (4)$$

We consider $SU(2)_L \times U(1)_Y \times U(1)_{L_\mu-L_\tau}$ is spontaneously broken into $U(1)_{\text{QED}} \times Z_2$, where the Z_2 symmetry, under which $\chi_\pm \rightarrow -\chi_\pm$, stabilizes the lightest dark-sector Majorana fermion which becomes the dark matter candidate (which will be further discussed in the following subsection). The parameter requirements are as follows. The spontaneous symmetry breaking (SSB) requires $\mu_H^2 > 0$ and $\mu_S^2 > 0$. The vacuum stability needs $\lambda_H > 0$, $\lambda_S > 0$ and $\lambda_{SH} > -2\sqrt{\lambda_H \lambda_S}$. The conditions with scalar eigenmasses $m_S^2, m_H^2 > 0$ give $\lambda_{SH}^2 < 4\lambda_H \lambda_S$.

Writing $\phi_H = \exp(i\tau^a \zeta^a / v_H) \cdot (0, (\phi_h + v_H) / \sqrt{2})^T$ and $\phi_S = \exp(i\sigma / v_S) (\phi_s + v_S) / \sqrt{2}$, the three fields ζ^a and the field σ can be set as zero respectively through the unitarity transformation; the former three (ζ^a) have then become the longitudinal degrees of freedom (DoFs) of W^\pm and Z , while the latter one (σ) the longitudinal DoF of Z' . The vacuum expectation value v_S , for which its additional phase (or sign) can be absorbed by field redefinitions of the dark sector particles, is taken to be positive. Thus, $(D_\mu \phi_S)^\dagger D^\mu \phi_S$ will give rise to the Z' 's mass term, $m_{Z'}^2 Z'_\mu Z'^\mu / 2$ with $m_{Z'} = 2g_\chi v_S$.

We can then represent the post-SSB Higgs-sector Lagrangian in terms of the neutral fields (ϕ_s, ϕ_h) , where the mass term is

$$\frac{1}{2} (\phi_s, \phi_h) \mathcal{M}^2 \begin{pmatrix} \phi_s \\ \phi_h \end{pmatrix} \quad (5)$$

with

$$\mathcal{M}^2 = \begin{pmatrix} 2\lambda_S v_S^2 & \lambda_{SH} v_S v_H \\ \lambda_{SH} v_S v_H & 2\lambda_H v_H^2 \end{pmatrix}. \quad (6)$$

Diagonalizing the mass matrix, the two neutral fields can be further expressed by the corresponding mass eigenstates (S, H) ,

$$\begin{pmatrix} \phi_s \\ \phi_h \end{pmatrix} = \begin{pmatrix} \cos \alpha & \sin \alpha \\ -\sin \alpha & \cos \alpha \end{pmatrix} \begin{pmatrix} S \\ H \end{pmatrix}, \quad (7)$$

where the mixing angle α satisfies the condition,

$$\sin 2\alpha = \frac{v_S v_H \lambda_{SH}}{\sqrt{(\lambda_H v_H^2 - \lambda_S v_S^2)^2 + (\lambda_{SH} v_S v_H)^2}} = \frac{2v_S v_H \lambda_{SH}}{m_H^2 - m_S^2}, \quad (8)$$

and the eigenmasses squared (m_S^2, m_H^2) are given by

$$\begin{aligned} m_S^2 &= \lambda_H v_H^2 + \lambda_S v_S^2 - \sqrt{(\lambda_H v_H^2 - \lambda_S v_S^2)^2 + (\lambda_{SH} v_S v_H)^2}, \\ m_H^2 &= \lambda_H v_H^2 + \lambda_S v_S^2 + \sqrt{(\lambda_H v_H^2 - \lambda_S v_S^2)^2 + (\lambda_{SH} v_S v_H)^2}. \end{aligned} \quad (9)$$

In the paper, we use H to be the SM-like Higgs with mass $m_H = 125.25$ GeV [50]. The Lagrangian for S , which includes its self-interaction terms and interactions with the dark gauge field, is given by

$$\begin{aligned} \mathcal{L} \supset & \frac{1}{2} \partial_\mu S \partial^\mu S - \frac{1}{2} m_S^2 S^2 - \left(\frac{g_\chi m_S^2 c_\alpha^3}{m_{Z'}} + \frac{m_S^2 s_\alpha^3}{2v_H} \right) S^3 + \frac{g_\chi^2}{2m_{Z'}^2} (c_\alpha^2 m_S^2 + s_\alpha^2 m_H^2) c_\alpha^4 S^4 \\ & + 2c_\alpha^2 g_\chi^2 S^2 Z'^\mu Z'_\mu + 2c_\alpha g_\chi m_{Z'} S Z'^\mu Z'_\mu + \dots, \end{aligned} \quad (10)$$

where $c_\alpha \equiv \cos \alpha$ and $s_\alpha \equiv \sin \alpha$.

B. The dark sector part involving dark fermions

The interaction containing the dark sector fermion is given by

$$\mathcal{L}_\chi = i\bar{\chi}\gamma^\mu D_\mu\chi - m_D\bar{\chi}\chi - \frac{f}{\sqrt{2}}\bar{\chi}^c\chi\phi_S^* - \frac{f^*}{\sqrt{2}}\bar{\chi}\chi^c\phi_S, \quad (11)$$

where $m_D > 0$ corresponds to a Dirac mass, and $\chi^c \equiv C\bar{\chi}^T$ is the charge conjugate of χ . In Eq. (11), $D_\mu = \partial_\mu + ig_\chi Z'_\mu$ is the covariant derivative, where the dark gauge coupling is defined as $g_\chi = g_{\mu\tau} \times q_d$. In this study, we treat g_χ as a free parameter to account for its relative strength compared to the lepton sector coupling $g_{\mu\tau}$. We have assumed a single Yukawa coupling f for both the left- and right-handed chiral components of the dark fermion χ . Although a Dirac fermion generally allows for two independent couplings, y_N and $y_{\bar{N}}$ (corresponding to the $\bar{\chi}_R^c\chi_L$ and $\bar{\chi}_L^c\chi_R$ terms, respectively) as discussed in Ref. [32], we explicitly invoke a discrete parity symmetry, $\chi_L \leftrightarrow \chi_R$. This symmetry enforces $y_N = y_{\bar{N}} \equiv f$, which remains robust against radiative corrections due to the vector-like nature of the gauge interactions in this model.

After SSB, ϕ_S develops a vacuum expectation value given by $\langle\phi_S\rangle = v_S/\sqrt{2}$. The mass term for the dark fermion in the Lagrangian is given by

$$\mathcal{L}_m = \mathcal{L}_m^D + \mathcal{L}_m^M, \quad (12)$$

where the Dirac mass part is

$$\begin{aligned} -\mathcal{L}_m^D &= \frac{m_D}{2}(\bar{\chi}\chi + \bar{\chi}^c\chi^c) \\ &= \frac{m_D}{2}(\bar{\chi}_R\chi_L + \bar{\chi}_L\chi_R + \bar{\chi}_R^c\chi_L^c + \bar{\chi}_L^c\chi_R^c), \end{aligned} \quad (13)$$

and the Majorana mass part is

$$\begin{aligned} -\mathcal{L}_m^M &= \frac{fv_S}{2}(\bar{\chi}^c\chi + \bar{\chi}\chi^c) \\ &= \frac{fv_S}{2}(\bar{\chi}_R^c\chi_L + \bar{\chi}_L\chi_R^c + \bar{\chi}_L^c\chi_R + \bar{\chi}_R\chi_L^c). \end{aligned} \quad (14)$$

Here we take f to be positive and $fv_S \gg m_D$. Note that through this paper, we adopt the notations¹ $\chi_L^c \equiv (\chi^c)_L = (\chi_R)^c$ and $\chi_R^c \equiv (\chi^c)_R = (\chi_L)^c$. When the Majorana mass dominates ($fv_S \gg m_D$), the system splits into two nearly degenerate Majorana eigenstates with masses,

$$m_\pm = fv_S \pm m_D, \quad (15)$$

¹ In the literature, someones instead use $\chi_L^c \equiv (\chi_L)^c$ and $\chi_R^c \equiv (\chi_R)^c$.

which correspond to the physical Majorana fermions,

$$\chi_+ = \frac{1}{\sqrt{2}}(\chi_L + \chi_R + \chi_R^c + \chi_L^c) \quad \text{and} \quad \chi_- = \frac{1}{\sqrt{2}}(-\chi_L + \chi_R - \chi_R^c + \chi_L^c), \quad (16)$$

respectively. Appendix A contains the relevant derivation. Rewriting Eq. (11) in the mass basis, the Lagrangian \mathcal{L}_χ is given by

$$\begin{aligned} \mathcal{L}_\chi = & \frac{i}{2}(\bar{\chi}_+ \gamma_\mu \partial^\mu \chi_+ + \bar{\chi}_- \gamma_\mu \partial^\mu \chi_-) - \frac{1}{2}g_\chi Z'^\mu (\bar{\chi}_+ \gamma_\mu \gamma_5 \chi_- + \bar{\chi}_- \gamma_\mu \gamma_5 \chi_+) \\ & - \frac{1}{2}[m_+ \bar{\chi}_+ \chi_+ + m_- \bar{\chi}_- \chi_-] - \frac{f}{2}(S \cos \alpha + H \sin \alpha)(\bar{\chi}_+ \chi_+ + \bar{\chi}_- \chi_-). \end{aligned} \quad (17)$$

It is important to distinguish our framework from other $U(1)$ gauge extensions. In widely studied pseudo-Dirac scenarios [32], the dark matter mass is dominated by a large Dirac term ($m_D \gg f v_S$), leading to gauge interactions via an inelastic vector current. Conversely, recent literature on sub-GeV dark matter [51] explores a distinct phenomenological limit, where degenerate Majorana states interact with the dark photon solely via an elastic axial-vector current.

Our model operates in the inverse hierarchy: the dominant mass originates from the Majorana term generated by the SSB of ϕ_S , while a tiny Dirac mass induces a slight splitting ($f v_S \gg m_D \neq 0$). To accurately reflect this physics, we refer to our candidate as nearly degenerate Majorana dark matter, highlighting its dominant mass origin, the non-zero mass splitting, and the strictly off-diagonal nature of its axial-vector gauge interactions. This distinct mass origin drives two crucial phenomenological features. First, as shown in Eq. (17), the states couple to the Z' exclusively via a strictly off-diagonal, inelastic axial-vector current ($\bar{\chi}_+ \gamma_\mu \gamma_5 \chi_- + \text{h.c.}$). Because standard elastic gauge scattering is absent, the scalar portal becomes the primary avenue for coherent elastic direct detection, allowing us to place stringent constraints on the mixing angle α (Sec. IX). Second, while pseudo-Dirac setups require highly suppressed couplings to maintain a tiny splitting—thereby hindering large self-interactions—our large Majorana mass is governed by an unsuppressed Yukawa coupling f . This naturally accommodates robust dark matter self-interactions (Sec. X) without fine-tuning.

C. The gauge boson sector

Assuming a generic kinetic mixing between the Z' and the SM hypercharge gauge boson \hat{B} at a high-energy scale, electroweak symmetry breaking induces effective mixings with the neutral SM

bosons. The relevant gauge Lagrangian reads

$$\begin{aligned} \mathcal{L}_{\text{gauge}} = & -\frac{1}{4}\hat{Z}_{\mu\nu}\hat{Z}^{\mu\nu} - \frac{1}{4}\hat{F}_{\mu\nu}\hat{F}^{\mu\nu} - \frac{1}{4}\hat{Z}'_{\mu\nu}\hat{Z}'^{\mu\nu} + \frac{1}{2}m_Z^2\hat{Z}_\mu\hat{Z}^\mu + \frac{1}{2}m_{Z'}^2\hat{Z}'_\mu\hat{Z}'^\mu \\ & - \frac{1}{2}\epsilon_0^A\hat{Z}'_{\mu\nu}\hat{F}^{\mu\nu} - \frac{1}{2}\epsilon_0^Z\hat{Z}'_{\mu\nu}\hat{Z}^{\mu\nu}, \end{aligned} \quad (18)$$

where hatted fields denote interaction eigenstates, $m_{Z'} = 2g_\chi v_S$, and $\hat{V}_{\mu\nu} \equiv \partial_\mu\hat{V}_\nu - \partial_\nu\hat{V}_\mu$ for $\hat{V} \in \{\hat{Z}, \hat{A}, \hat{Z}'\}$. Originating from the gauge-invariant operator $-\frac{\epsilon}{2}\hat{Z}'_{\mu\nu}\hat{B}^{\mu\nu}$ [52], the bare parameters are related by $\epsilon_0^A = \epsilon \cos \theta_W$ and $\epsilon_0^Z = -\epsilon \sin \theta_W$. Consequently, $\epsilon_0^Z = -\epsilon_0^A \tan \theta_W$, leaving only one independent mixing parameter.

In addition to the residual mixing among the gauge fields, allowing the dark gauge boson to directly couple to μ and τ lepton sectors, these neutral gauge bosons coupled to SM and dark fermions are described by the Lagrangian,

$$\mathcal{L} \supset - (g_Z J_Z^\mu, e J_\gamma^\mu, g_{\mu\tau} J_{L_\mu-L_\tau}^\mu + g_\chi J_D^\mu) \hat{\mathbf{V}}_\mu, \quad (19)$$

where $\hat{\mathbf{V}}_\mu = (\hat{Z}_\mu, \hat{A}_\mu, \hat{Z}'_\mu)^T$ is a vector column formed by gauge fields, $J_Z^\mu = J_3^\mu - \sin^2 \theta_W J_\gamma^\mu$ is the neutral current with $J_3^\mu = \bar{\psi}\gamma^\mu P_L T^3 \psi$, $J_\gamma^\mu = \bar{\psi}\gamma^\mu Q \psi$ is the electromagnetic current with ψ being the SM fermion and Q being the corresponding electromagnetic charge operator, $g_Z \equiv e/(\sin \theta_W \cos \theta_W)$, and dark Majorana current $J_D^\mu = (1/2)(\bar{\chi}_+\gamma_\mu\gamma_5\chi_- + \bar{\chi}_-\gamma_\mu\gamma_5\chi_+)$. Here, $P_L = (1 - \gamma_5)/2$ is the left-handed projector and the eigenvalue of T^3 is $\pm 1/2$ for a left-handed doublet SM fermion or 0 for an isosinglet SM fermion.

However, \hat{Z}' can still mix with the photon \hat{A} and with the \hat{Z} boson at a one-loop level due to $m_\mu \neq m_\tau$ at low energy with the scale $\mu \lesssim m_\mu$. Thus, the Lagrangian relevant to the gauge mixing, involving the one-loop corrections, is described by

$$\mathcal{L}_{\text{mix}} = -\frac{1}{2}\epsilon_A\hat{Z}'_{\mu\nu}\hat{F}^{\mu\nu} - \frac{1}{2}\epsilon_Z\hat{Z}'_{\mu\nu}\hat{Z}^{\mu\nu}, \quad (20)$$

with $\epsilon_A = \epsilon_0^A + \epsilon_{\text{loop}}^A$ and $\epsilon_Z = \epsilon_0^Z + \epsilon_{\text{loop}}^Z$, where the one-loop mixing parameters below the m_μ scale are given by [32, 52–54]

$$\epsilon_{\text{loop}}^A = -\frac{eg_{\mu\tau}}{12\pi^2} \ln\left(\frac{m_\tau^2}{m_\mu^2}\right) \simeq -\frac{g_{\mu\tau}}{69}, \quad \epsilon_{\text{loop}}^Z = \left(-\frac{1}{4} + \sin^2 \theta_W\right) \frac{1}{\sin \theta_W \cos \theta_W} \epsilon_A', \quad (21)$$

with θ_W being the Weinberg angle which is satisfied with $\sin \theta_W = 0.231$ at the scale m_Z in the $\overline{\text{MS}}$ scheme [50].

To obtain the physical mass eigenstates, we diagonalize the kinetic and mass terms of the gauge fields. Following the procedure outlined in Appendix B, the interaction eigenstates $\hat{\mathbf{V}}_\mu$ are related to the physical states $\mathbf{V}_\mu = (Z_\mu, A_\mu, Z'_\mu)^T$ via the transformation $\hat{\mathbf{V}}_\mu = \mathbf{U}^{-1}\mathbf{V}_\mu$. Substituting this

relation into Eq. (19), the resultant Lagrangian describing the interactions of the physical gauge bosons coupled to the SM and dark currents is given by

$$\begin{aligned}
\mathcal{L} &\supset -(g_Z J_Z^\mu, e J_\gamma^\mu, g_{\mu\tau} J_{L_\mu-L_\tau}^\mu + g_\chi J_D^\mu) \mathbf{U}^{-1} \mathbf{V}_\mu \\
&= -e J_\gamma^\mu A_\mu - g_Z J_Z^\mu Z_\mu - g_{\mu\tau} J_{L_\mu-L_\tau}^\mu Z'_\mu - g_\chi J_D^\mu Z'_\mu \\
&\quad + \epsilon_A e J_\gamma^\mu Z'_\mu + \epsilon_Z \frac{m_Z^2}{m_Z^2 - m_{Z'}^2} (g_{\mu\tau} J_{L_\mu-L_\tau}^\mu + g_\chi J_D^\mu) Z_\mu - \epsilon_Z \frac{m_{Z'}^2}{m_Z^2 - m_{Z'}^2} g_Z J_Z^\mu Z'_\mu + \mathcal{O}(\epsilon_{A,Z}^2). \quad (22)
\end{aligned}$$

III. THE PARAMETERS

We adopt H to be the observed Higgs resonance with mass $m_H = 125.25$ GeV and vacuum expectation value $v_H = 246.22$ GeV [50]. Compared with the SM, the present model comprises 8 independent parameters:

$$m_-, \quad m_+ \equiv m_- + \delta m, \quad m_{Z'}, \quad m_S, \quad g_{\mu\tau}, \quad f, \quad \alpha, \quad \text{and} \quad \epsilon_0^A, \quad (23)$$

with $\delta m = 2m_D$. Note that the dark gauge coupling g_χ is not an independent parameter in this setup. From the mass relations in Eq. (15) and Eq. (18), it is determined by the Yukawa coupling f and the gauge boson mass $m_{Z'}$ via the relation:

$$g_\chi = \frac{f m_{Z'}}{m_+ + m_-} \simeq \frac{f m_{Z'}}{2m_-}, \quad (24)$$

where the approximation holds for the small mass splitting limit, $\delta m \ll m_-$.

Our analysis of the parameter space is guided by the following considerations: (i) We assume a small mass splitting, $\delta m \ll m_\mp, m_{Z'}$. (ii) The kinetic mixing parameter ϵ_A is defined as $\epsilon_A \simeq \epsilon_0^A + \epsilon_{\text{loop}}^A$, where ϵ_0^A represents the primordial kinetic mixing generated at high scales. Its phenomenological impact will be discussed in Sec. IV. (iii) To ensure dark matter remains in thermal equilibrium with the SM bath before freeze-out, we assume $m_S > 2m_{Z'}$. (iv) The relic abundance is primarily determined by the annihilation processes $\chi_\mp \chi_\mp \rightarrow SS, Z'Z'$ and $\chi_- \chi_+ \rightarrow SZ'$. This requirement fixes the coupling f for a given dark matter mass m_- . Consequently, g_χ is derived using Eq. (24). (v) We assume $m_S \ll m_\pm$ to enhance the self-interaction cross-section for solving small-scale structure problems. (vi) The scalar mixing angle α is constrained by various experimental searches, as analyzed in Sec. IX.

IV. CONSTRAINTS FROM $(g-2)_\mu$ AND KINETIC MIXING

Recently, the prediction for the muon anomalous magnetic moment has been updated by the Muon $g-2$ Theory Initiative [43]. This new assessment incorporates lattice QCD results for the

hadronic vacuum polarization, leading to a Standard Model prediction that is in better agreement with experimental data, unlike previous assessments [44–48] which favored a significant new physics contribution. Consequently, the difference between the experimental value and the Standard Model prediction is now given by

$$\Delta a_\mu \equiv a_\mu^{\text{exp}} - a_\mu^{\text{SM}} = (38 \pm 63) \times 10^{-11}. \quad (25)$$

In the $m_{Z'} \ll m_Z$ limit, the leading contribution to the muon anomalous magnetic moment is well approximated by [55]

$$\Delta a_\mu \simeq \frac{(g_{\mu\tau} + e\epsilon_A)^2}{4\pi^2} \int_0^1 dx \frac{m_\mu^2 x^2 (1-x)}{m_{Z'}^2 (1-x) + m_\mu^2 x^2}, \quad (26)$$

where the effective kinetic mixing ϵ_A incorporates both the primordial ϵ_0^A and an irreducible μ/τ loop-induced shift, yielding $e\epsilon_A \simeq e\epsilon_0^A - 0.0044g_{\mu\tau}$ (see Appendix C for full expressions).

Recent theoretical updates [43] align the SM prediction of $(g-2)_\mu$ with experimental data, imposing a strict upper bound on Δa_μ . As summarized in Fig. 1, this new 2σ limit (solid red line) leaves a broad viable parameter space. Specifically, the region $m_{Z'} \lesssim 200$ MeV is bounded primarily by neutrino trident production at CCFR [56, 57] (gray shaded region), whereas BABAR searches for $Z' \rightarrow \mu^+\mu^-$ [58] dominate at heavier masses. Crucially, the resolution of the $(g-2)_\mu$ anomaly reopens the $m_{Z'} > 200$ MeV regime, which was previously ruled out by the tension between the old $(g-2)_\mu$ favored band and BABAR exclusions.

We now turn to the constraints arising from the kinetic mixing between the dark sector and the photon. As introduced in Sec. II C, the mixing parameter receives contributions from both the irreducible one-loop vacuum polarization, $\epsilon_{\text{loop}}^A \simeq -g_{\mu\tau}/69$, and any primordial kinetic mixing ϵ_0^A generated at high scales. While often assumed to be negligible, a non-zero ϵ_0^A can interfere with the loop-induced mixing, significantly altering the phenomenological bounds.

The constraints from White Dwarf (WD) cooling [59, 60] and Borexino [32, 61], arising essentially from the effective kinetic mixing between the Z' and the photon, are depicted as blue boundaries in Fig. 1 under the assumption of vanishing primordial kinetic mixing ($\epsilon_0^A = 0$). Taking the interference between these two contributions into account, the standard bounds on $g_{\mu\tau}$ can be analytically generalized as:

$$g_{\mu\tau} \times \left| 1 - \frac{69\epsilon_0^A}{g_{\mu\tau}} \right|^{1/2} \leq 6.1 \times 10^{-4} \times \frac{m_{Z'}}{12 \text{ MeV}}. \quad (27)$$

This inequality shows that if the primordial mixing ϵ_0^A cancels the loop contribution (i.e., $\epsilon_0^A \approx g_{\mu\tau}/69$), the effective mixing is suppressed, allowing for a much larger $g_{\mu\tau}$ than the standard

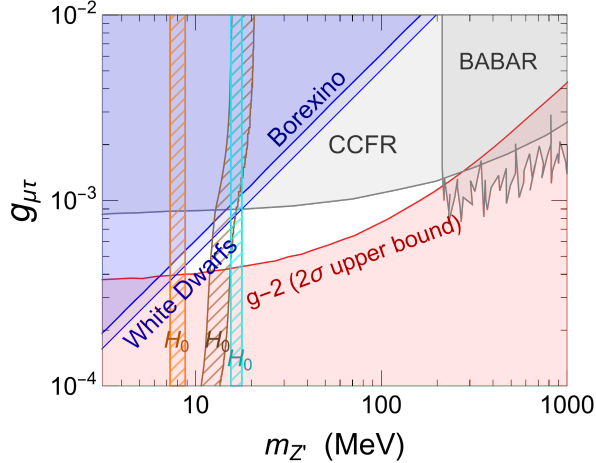


FIG. 1. The parameter space of the gauged $U(1)_{L_\mu-L_\tau}$ model. Gray shaded regions indicate exclusions from CCFR [56, 57] and BABAR [58], while constraints from WD cooling [59, 60] and Borexino [32, 61] are indicated by blue boundaries (assuming vanishing primordial kinetic mixing, $\epsilon_0^A = 0$). The solid red line represents the updated $(g-2)_\mu$ 2σ upper bound [43]; the region below this line is allowed by the new data. The hatched bands indicate the Hubble-tension preferred region ($3.12 \lesssim N_{\text{eff}} \lesssim 3.33$) for kinetic mixings $|\epsilon_A| = 10^{-7}$ (orange), $g_{\mu\tau}/69$ (brown), and 0 (cyan), appearing in that order from left to right at $g_{\mu\tau} = 10^{-4}$. The domain to the left of these bands yields $N_{\text{eff}} > 3.33$ and is disfavored by Planck 2018 constraints [62].

bound suggests. Crucially, even if the condition $e\epsilon_A \ll g_{\mu\tau}$ is satisfied, small kinetic mixing effects from high-energy scales can significantly alter the constraints derived from both WD cooling and Borexino data. This interference effect effectively relaxes the constraints compared to the standard bounds ($\epsilon_0^A = 0$) shown in Fig. 1.

In Fig. 1, the hatched areas, corresponding to $3.12 \lesssim N_{\text{eff}} \lesssim 3.33$, represent the parameter space that helps alleviate the disagreement between cosmological and local Hubble constant measurements, known as the Hubble tension (H_0). This preferred range is supported by analyses combining Planck data with local H_0 measurements [62]. The orange, brown, and cyan hatched bands represent the scenarios with $|\epsilon_A| = 10^{-7}$, $g_{\mu\tau}/69$, and 0, respectively (appearing in this order from left to right at $g_{\mu\tau} = 10^{-4}$). The parameter space to the left of these bands yields $N_{\text{eff}} > 3.33$, which is disfavored by Planck 2018 constraints (TT, TE, EE+lowE+lensing+BAO at 95% CL) [62]. A detailed analysis of N_{eff} will be given in Sec. VI.

V. BOLTZMANN EQUATIONS AND THERMAL FREEZE-OUT

In this section, we will estimate the freeze-out parameter $x_f = m_-/T_{f_0}$ and the related DM annihilation cross section that can result in the present-day relic abundance, where T_{f_0} is the DM freeze-out temperature. We consider the nearly degenerate case $\delta m \ll m_{\pm}$. After freeze-out, the lifetime of χ_+ is determined by its 3-body decay channels, $\chi_+ \rightarrow \chi_- \nu_\mu \bar{\nu}_\mu$ and $\chi_- \nu_\tau \bar{\nu}_\tau$, depending on the values of δm and the coupling constant g_χ . The heavier Majorana fermion χ_+ could also be a dark matter candidate if its lifetime is comparable to or longer than the Universe's age. Similar to the case of coannihilations discussed in Ref. [63], the final dark matter abundance is described by the sum of number densities of all dark sector Majorana fermions,

$$n = n_{\chi_+} + n_{\chi_-}, \quad (28)$$

of which the evolution follows the Boltzmann equation,

$$\frac{dn}{dt} + 3Hn = - \sum_{i,j=\chi_{\pm}} \sum_X \langle \sigma v \rangle_{i,j \rightarrow X} \left(n_i n_j - n_i^{\text{eq}} n_j^{\text{eq}} \right), \quad (29)$$

with $X \equiv$ all possible final states. Addressing small-scale issues requires significant self-interactions among dark matter particles, facilitated by light S particles that are strongly coupled to dark matter via a large coupling constant. Therefore, we consider that the DM freeze-out process is governed by the combined annihilation channels into scalars ($\chi_{\mp}\chi_{\mp} \rightarrow SS$) and gauge bosons ($\chi_{\mp}\chi_{\mp} \rightarrow Z'Z'$ and $\chi_- \chi_+ \rightarrow Z'S$). During this epoch, S maintains its thermal equilibrium density at the same temperature as the SM bath primarily via the reactions $S \leftrightarrow Z'Z'$ and $Z' \leftrightarrow \text{SM SM}$, meaning $n_S = n_S^{\text{eq}}$, until after χ_+ and χ_- freeze-out². This property has been applied in Eq. (29).

In our analysis, the requirement of reproducing the observed relic abundance fixes the Yukawa coupling f (and consequently determines g_χ via Eq. (24)) for a given dark matter mass. Although our numerical calculation includes all the aforementioned channels, we will show that the scalar channel $\chi_{\mp}\chi_{\mp} \rightarrow SS$ typically plays the primary role, while the channels involving Z' in the final state provide subdominant but non-negligible contributions. These Majorana annihilation cross sections, along with the related thermally averaged cross section formulas, are listed in Appendix E. Because we have $\delta m \ll m_{\chi_{\pm}}$, the freeze-out parameter x_f^+ for χ_+ closely matches $x_f^- \equiv x_f$, allowing us to use the approximation,

$$\frac{n_{\chi_{\pm}}}{n} \simeq \frac{n_{\chi_{\pm}}^{\text{eq}}}{n^{\text{eq}}}. \quad (30)$$

² The decay widths of Z' and S , including the Higgs decaying into dark sector particles, are listed in Appendix D

Thus, we write the Boltzmann equation as

$$\frac{dn}{dt} + 3Hn = -\langle\sigma_{\text{eff}}v\rangle (n^2 - (n^{\text{eq}})^2), \quad (31)$$

where

$$\langle\sigma_{\text{eff}}v\rangle = \sum_{i,j=\chi_{\pm}} \sum_X \langle\sigma v\rangle_{i,j\rightarrow X} \frac{n_i^{\text{eq}} n_j^{\text{eq}}}{n^{\text{eq}} n^{\text{eq}}}. \quad (32)$$

We rewrite Eq. (31) in terms of the yield $Y = n/s$, which represents the ratio of n to the entropy density of the Universe, as

$$\frac{dY}{dx} = -\frac{m_-}{x^2} \left(\frac{\pi}{45G}\right)^{1/2} g_*^{1/2} \langle\sigma_{\text{eff}}v\rangle (Y^2 - (Y^{\text{eq}})^2), \quad (33)$$

where $Y^{\text{eq}} = n^{\text{eq}}/s$, and $g_*^{1/2} \equiv \tilde{h}_{\text{eff}}/g_{\text{eff}}^{1/2}$ with $\tilde{h}_{\text{eff}} \equiv h_{\text{eff}}[1 + (1/3)(d \ln h_{\text{eff}}/d \ln T)]$. Here, h_{eff} and g_{eff} are the effective degrees of freedom (DoFs) for the Universe's total entropy and energy density, respectively, with

$$s = h_{\text{eff}}(T) \frac{2\pi^2}{45} T^3, \quad \rho = g_{\text{eff}}(T) \frac{\pi^2}{30} T^4. \quad (34)$$

In our analysis, we adopt the effective degrees of freedom associated with a QCD phase transition temperature of $T_{\text{QCD}} = 150$ MeV [64].

We follow the method outlined in Refs. [65, 66] to determine the freeze-out parameter x_f and the appropriate coupling constant f related to the DM annihilation cross section that yields the current relic abundance. We define $T_{\text{fo}} (= m_-/x_f)$ as the temperature where $Y - Y^{\text{eq}} = \delta \cdot Y^{\text{eq}}$, ensuring that $d\delta/dx \ll 1$ and that δ is approximately 1. Next, we derive the approximation from Eq. (33), given by

$$\left(1 - \frac{27}{8x} - \frac{\delta_m x}{2} - \frac{29\delta_m}{16}\right) \approx x^{-1/2} e^{-x} \delta(\delta + 2) \sqrt{\frac{45}{\pi^5}} \frac{g_*^{1/2} M_{\text{pl}} m_-}{h_{\text{eff}}} g_- \langle\sigma_{\text{eff}}v\rangle, \quad (35)$$

at $x = x_f$. Here, g_- denotes the internal degrees of freedom of the Majorana fermion χ_- , $M_{\text{pl}} \equiv (8\pi G)^{-1/2}$ signifies the reduced Planck mass, and $\delta_m = m_+/m_- - 1 = \delta m/m_-$. Since x_f logarithmically depends on δ , we set $\delta = 1$ for the analysis.

The freeze-out process is dominated by annihilation $\chi_{\mp}\chi_{\mp} \rightarrow SS, Z'Z'$ and $\chi_- \chi_+ \rightarrow Z'S$, approximating the effective cross section as

$$\begin{aligned} \langle\sigma_{\text{eff}}v\rangle &\simeq \frac{1}{4} \left(\langle\sigma v\rangle_{\chi_- \chi_- \rightarrow SS, Z'Z'} (1 + x \delta_m) + \langle\sigma v\rangle_{\chi_+ \chi_+ \rightarrow SS, Z'Z'} (1 - x \delta_m) \right) + \frac{1}{2} \langle\sigma v\rangle_{\chi_- \chi_+ \rightarrow Z'S} \\ &\simeq \frac{1}{2} \left(\langle\sigma v\rangle_{\chi_- \chi_- \rightarrow SS} + \langle\sigma v\rangle_{\chi_- \chi_- \rightarrow Z'Z'} + \langle\sigma v\rangle_{\chi_- \chi_+ \rightarrow Z'S} \right). \end{aligned} \quad (36)$$

Neglecting the contributions proportional to $\delta_m, m_{Z'}^2/m_-^2, m_S^2/m_-^2$ and x^{-3} , we have the thermally averaged cross sections:

$$\langle\sigma v\rangle_{\chi_{\mp}\chi_{\mp}\rightarrow SS} \simeq \frac{9f^4}{64\pi m_-^2}x^{-1} - \frac{51f^4}{64\pi m_-^2}x^{-2}, \quad (37)$$

$$\begin{aligned} \langle\sigma v\rangle_{\chi_{\mp}\chi_{\mp}\rightarrow Z'Z'} &\simeq \frac{g_{\chi}^4}{16\pi m_-^2} \left\{ 1 + 3\frac{f^2 m_-^2}{g_{\chi}^2 m_{Z'}^2} \left[\left(1 - \frac{8}{3}d + \frac{8}{3}d^2\right) \left(\frac{1}{x} + \frac{3}{x^2}\right) - (5 - 12d + 12d^2) \frac{1}{x} \right] \right\} \\ &\simeq \frac{f^4}{64\pi m_-^2} (x^{-1} - 3x^{-2}), \end{aligned} \quad (38)$$

$$\begin{aligned} \langle\sigma v\rangle_{\chi_{-}\chi_{+}\rightarrow Z'S} &\simeq \frac{\delta m^2 g_{\chi}^2 f^2}{32\pi m_{-}^4} + \frac{g_{\chi}^2 f^2}{4\pi m_{Z'}^2} x^{-1} \\ &\simeq \frac{f^4}{16\pi m_-^2} x^{-1}, \end{aligned} \quad (39)$$

where $d = g_{\chi} m_- / (f m_{Z'})$. In the present nearly degenerate Majorana DM model, we have $d \approx 1/2$ due to $2g_{\chi} m_- \approx f m_{Z'}$. All of these thermally averaged cross sections are p -wave dominant. It is important to note that the channels with Z' final states (Eqs. (38) and (39)) receive significant enhancement factors proportional to $(f m_- / g_{\chi} m_{Z'})^2$ in their p -wave terms. Here, we have neglected the results for $\chi_{\mp}\chi_{\pm} \rightarrow \mu^+\mu^-, \nu_{\mu}\bar{\nu}_{\mu}, \tau^+\tau^-, \nu_{\tau}\bar{\nu}_{\tau}$, of which their cross sections are much smaller than the other channels in the interesting region. The detailed expressions for the annihilation cross sections are given in Appendix E.

It is noteworthy that in our nearly degenerate Majorana DM framework, the hierarchy of these annihilation channels differs significantly from the pseudo-Dirac DM model [32]. As derived above, the relative contributions to the thermally averaged cross section rigidly follow the ratio $\langle\sigma v\rangle_{\chi_{\mp}\chi_{\mp}\rightarrow SS} : \langle\sigma v\rangle_{\chi_{\mp}\chi_{\mp}\rightarrow Z'Z'} : \langle\sigma v\rangle_{\chi_{-}\chi_{+}\rightarrow Z'S} \approx 9 : 1 : 4$. Consequently, the p -wave SS channel remains highly significant and provides the leading contribution to the total annihilation rate, in contrast to pseudo-Dirac DM scenarios where the s -wave $Z'S$ channel typically drives the freeze-out process.

We integrate³ Eq. (33) from freeze-out x_f to x_0 , with yields Y_f and Y_0 , respectively, considering that Y^{eq} is insignificant compared to Y . Here $x_0 = m_- / T_0$, with T_0 indicating the photon bath temperature below which DM self-interactions become too weak to maintain thermal equilibrium among themselves. The potential corrections arising from the Sommerfeld effect will be addressed separately in Sec. VIII. For $x > x_0$, the DM particles become free-streaming and non-thermal. However, they still follow a Maxwell-Boltzmann distribution, $f_{\text{MB}} \propto \exp[p^2 / (2m_{\text{DM}} T_{\text{DM}})]$, because the momentum redshifts as $p \propto a^{-1}$, and the DM temperature scales as $T_{\text{DM}} = T^2 / T_{kd} \propto a^{-2}$.

³ This discussion is general and does not distinguish between χ_+ or χ_- . To differentiate them, one must further consider the decoupling of χ_+ from χ_- when the annihilation rate of $\chi_+\chi_+ \rightarrow \chi_-\chi_-$ drops below the Hubble expansion rate, followed by the non-equilibrium decay of χ_+ to χ_- . See Sec. VII for more details.

Consequently, we get

$$-\int_{Y_f}^{Y_0} \frac{dY}{Y^2} \approx m_- \left(\frac{\pi}{45G} \right)^{1/2} \left(\int_{x_f}^{x_{kd}} g_*^{1/2} \langle \sigma_{\text{eff}} v \rangle \frac{dx}{x^2} + \int_{x_{kd}}^{x_0} g_*^{1/2} \langle \sigma_{\text{eff}} v \rangle \frac{dx}{x^2} \right), \quad (40)$$

where $x_{kd}(= m_-/T_{kd})$ represents the value of x at the temperature when DM kinetically decouples from the bath. Between x_f and x_{kd} , DM particles remain in kinetic equilibrium with the SM bath through elastic collisions, especially $\chi_{\pm} S \leftrightarrow \chi_{\pm} S$ even after freeze-out (refer to Appendix F for a detailed discussion); in other words, we have $T_{\text{DM}} = T$. Both S and Z' stay in thermal equilibrium with the (ν_{μ}, ν_{τ}) bath through interactions such as $S \leftrightarrow Z' Z'$ and $Z' \leftrightarrow \nu_{\mu} \bar{\nu}_{\mu}, \nu_{\tau} \bar{\nu}_{\tau}$. Additionally, as will be explained in Sec. VI and shown in Fig. 4, the process $Z' \leftrightarrow e^+ e^-$ maintains $T = T_{\nu_{\mu}}$ until the temperature drops below m_e . It is observed that χ_{\pm} , with masses ranging from a few GeV to several hundred GeV, kinetically decouple from the scalar field S at a temperature (T_{kd}) roughly between 210 and 250 MeV. All relevant details are available in Appendix F. When $T < T_{kd}$, the dark matter's temperature T_{DM} instead decreases as $a^{-2} \propto T^2$, i.e., $T_{\text{DM}} = T^2/T_{kd}$.

Since the annihilation rate of dark matter is nearly negligible at $x = x_0$, we can use Y_0 as its current value. The left side of Eq. (40) is roughly Y_0^{-1} because $Y_f \gg Y_0$, while the integral on the right side is mainly influenced by the region near x_f , making it insensitive to the value of x_0 . The DM relic abundance [50] is related to Y_0 with

$$\Omega_{\text{DM}} \simeq \frac{m_- Y_0 s_0}{\rho_c} \simeq 0.1200/h^2, \quad (41)$$

where $\rho_c = 1.0537 \times 10^{-5} h^2 (\text{GeV}/c^2) \text{cm}^{-3}$ is the critical density with $h \simeq 0.674$, and $s_0 = 2891.2 \text{ cm}^{-3}$ is the entropy density today. From Eqs. (35) and (40), we numerically compute x_f and the coupling constant f as functions of m_- using the DM relic abundance detailed in Eq. (41). We examine the scenario where $m_{\pm} \gg m_{Z'}$ and the scalar S is located in the range of $12 \text{ MeV} \lesssim m_S \lesssim 400 \text{ MeV}$, while also fulfilling the condition $m_S \gtrsim 2m_{Z'}$. The outcomes are illustrated in Fig. 2 for $m_- \in (1, 1000) \text{ GeV}$. For a comparative analysis, when δ is ± 0.5 , we find that the uncertainty in f is roughly less than 1%, meaning the corresponding error of $\langle \sigma v \rangle_{\chi-\chi \rightarrow SS}$ is below 5%.

In our analysis, the coupling f is fixed by the relic density requirement, $\Omega_{\text{DM}} h^2 \simeq 0.12$. Since the annihilation cross section scales as $\langle \sigma_{\text{eff}} v \rangle \propto f^4/m_-^2$, a constant relic density implies $f \propto m_-^{1/2}$. Using the relation in Eq. (24), the derived dark gauge coupling behaves as $g_{\chi} \propto m_{Z'} m_-^{-1/2}$.

In Fig. 3, we present the numerical results for the derived g_{χ} as a function of the DM mass m_- . The left panel shows the case for fixed gauge boson masses $m_{Z'} = 10, 50, 100 \text{ MeV}$. Here, g_{χ} decreases as m_- increases, following the $m_-^{-1/2}$ scaling. It also shows that for a lighter Z' ,

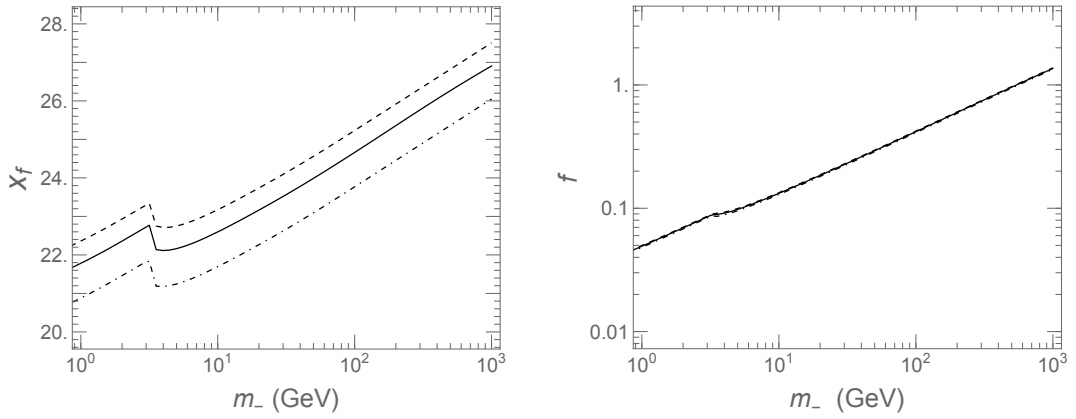


FIG. 2. Left panel: x_f as a function of m_- . Right panel: The coupling constant f that can produce the correct DM relic density as a function of m_- . The solid curve corresponds to $\delta = 1$, while the dashed and dotdashed curves are for $\delta = 1.5$ and 0.5 , respectively. The unsmooth part of the curves is due to the QCD phase transition at $T_{\text{QCD}} = 150$ MeV.

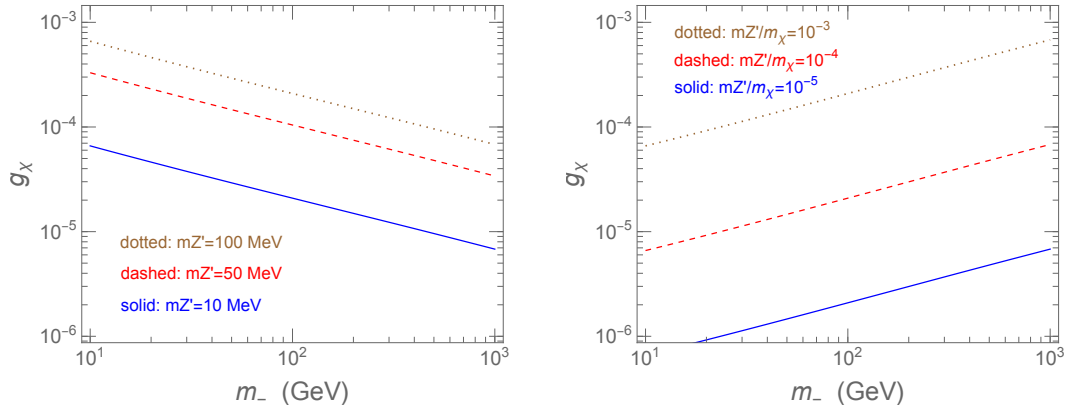


FIG. 3. The derived dark gauge coupling $g_\chi (\simeq f m_{Z'}/2m_-)$ as a function of the DM mass m_- . The **left panel** shows the results for fixed gauge boson masses $m_{Z'} = 10$ (solid blue), 50 (dashed red), and 100 MeV (dotted brown). The **right panel** assumes fixed mass ratios of $m_{Z'}/m_- = 10^{-5}$ (solid blue), 10^{-4} (dashed red), and 10^{-3} (dotted brown). In both cases, the Yukawa coupling f is determined by the relic density constraint (with $\delta = 1$) as shown in Fig. 2.

a smaller gauge coupling is required. The right panel illustrates the case where the mass ratio $m_{Z'}/m_-$ is kept constant. In this scenario, g_χ is directly proportional to f and thus grows as $m_-^{1/2}$. The results show that for the parameter space of interest, the derived gauge coupling g_χ generally remains small ($g_\chi \lesssim 10^{-3}$), while the Yukawa coupling f is adjusted to satisfy the observed relic

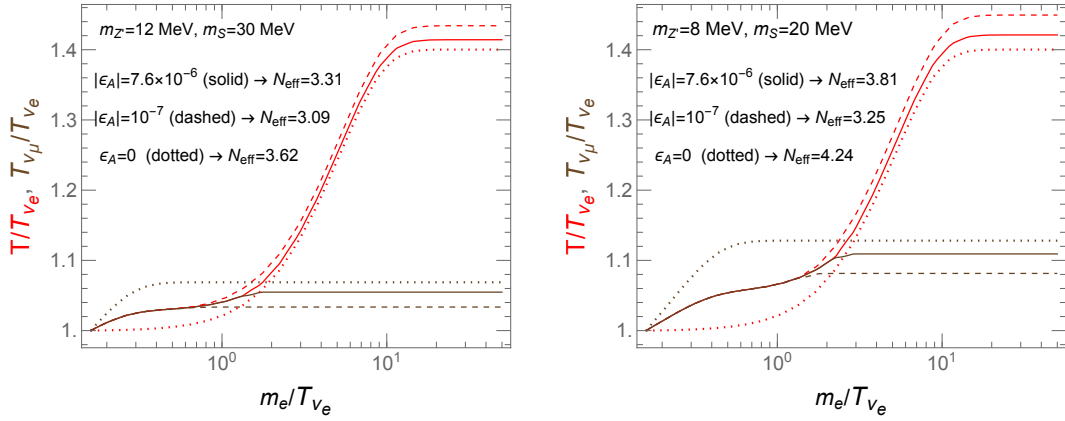


FIG. 4. The evolution of the ratios T/T_{ν_e} (red) and T_{ν_μ}/T_{ν_e} (brown) for $|\epsilon_A| = 7.6 \times 10^{-6}$ (solid line), 10^{-7} (dashed line), and 0 (dotted line), with $m_{Z'} = 12$ MeV and $m_S = 30$ MeV in the left panel, and $m_{Z'} = 8$ MeV and $m_S = 20$ MeV in the right panel. The resulting N_{eff} value is also given.

density.

VI. CONSTRAINT FROM EFFECTIVE NUMBER OF RELATIVISTIC SPECIES AND HUBBLE TENSION

During thermal evolution, the decay rates of $S \rightarrow Z'Z'$ and $Z' \rightarrow \nu_\mu \bar{\nu}_\mu, \nu_\tau \bar{\nu}_\tau$, are greater than the Hubble expansion rate. As a result, S and Z' remain in thermal equilibrium with μ - and τ -neutrinos, maintaining a zero chemical potential even after neutrinos decouple from photons. However, due to residual kinetic mixing between Z' and the electromagnetic field, Z' can decay into an e^+e^- pair, with the decay width,

$$\Gamma_{Z' \rightarrow e^+e^-} = \frac{\alpha \epsilon_A^2 m_{Z'}}{3} \left(1 + \frac{2m_e^2}{m_{Z'}^2}\right) \left(1 - \frac{4m_e^2}{m_{Z'}^2}\right)^{1/2}. \quad (42)$$

Since the DoFs of S and Z' are ultimately integrated into the SM bath, these effects can impact the effective number of relativistic species, N_{eff} . This parameter is defined based on the total radiation energy density, ρ_t , and the photon density, ρ_γ , as

$$\frac{\rho_t}{\rho_\gamma} = 1 + N_{\text{eff}} \frac{7}{8} \left(\frac{4}{11}\right)^{4/3}. \quad (43)$$

Before electron neutrino-photon decoupling, all neutrinos stay in thermal equilibrium with photon-coupled particles through weak interactions with e^\pm and via $Z' \leftrightarrow e^+e^-$. About one second after the Big Bang, when the weak interaction rate falls below the expansion rate of the

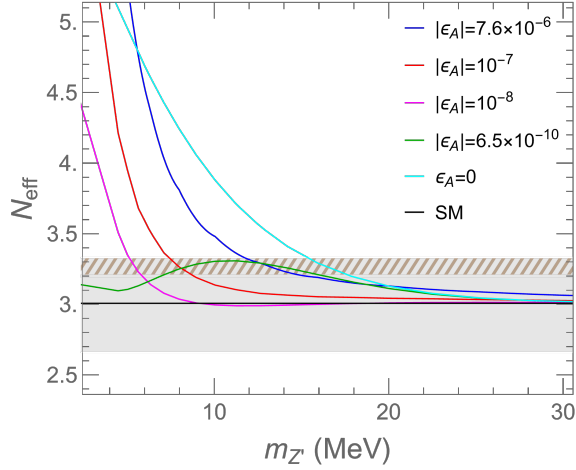


FIG. 5. N_{eff} as a function of $m_{Z'}$. The solid curves correspond to model predictions with $|\epsilon_A| = 0, 7.6 \times 10^{-6}, 10^{-7}, 6.5 \times 10^{-10},$ and 10^{-8} (from top to bottom at $m_{Z'} = 7$ MeV). The horizontal line indicates the SM value. The gray and hatched regions show the 95% CL allowed range ($N_{\text{eff}} = 2.99^{+0.34}_{-0.33}$) from Planck 2018 [62]. The hatched brown sub-region ($3.12 \lesssim N_{\text{eff}} \lesssim 3.33$) is favored by local H_0 measurements to alleviate the Hubble tension, with the lower bound corresponding to the 1σ preference ($N_{\text{eff}} \approx 3.27 \pm 0.15$ [62]).

universe, its corresponding temperature is estimated to be around $T \approx 3.2$ MeV [34]. From this point forward, interactions between the two groups of particles— (γ, e^\pm) and $(\nu_\mu, \nu_\tau, S, Z')$ —mainly originate from $Z' \leftrightarrow e^+e^-$, which results in the transfer of entropy between them. To clarify, we define three temperatures: T , T_{ν_e} , and T_{ν_μ} , corresponding to the sets (γ, e^\pm) , (ν_e) , and $(\nu_\mu, \nu_\tau, S, Z')$, respectively. When the temperature drops below approximately 3.2 MeV, we can estimate the neutrino-to-photon temperature ratio and N_{eff} by analyzing the separate evolution of the comoving entropy densities, as described in Ref. [32]:

$$\frac{1}{a^3} \frac{d}{dt} (s_\gamma(T)a^3 + 2s_e(T)a^3) = \frac{1}{T} (\langle \Gamma_{Z' \rightarrow e^+e^-} \rangle_{T_{\nu_\mu}} \rho_{Z'}(T_{\nu_\mu}) - \langle \Gamma_{Z' \rightarrow e^+e^-} \rangle_T \rho_{Z'}(T)), \quad (44)$$

$$\begin{aligned} \frac{1}{a^3} \frac{d}{dt} (2s_{\nu_\mu}(T_{\nu_\mu})a^3 + 2s_{\nu_\tau}(T_{\nu_\mu})a^3 + s_S(T_{\nu_\mu})a^3 + s_{Z'}(T_{\nu_\mu})a^3) \\ = -\frac{1}{T_{\nu_\mu}} (\langle \Gamma_{Z' \rightarrow e^+e^-} \rangle_{T_{\nu_\mu}} \rho_{Z'}(T_{\nu_\mu}) - \langle \Gamma_{Z' \rightarrow e^+e^-} \rangle_T \rho_{Z'}(T)), \end{aligned} \quad (45)$$

$$a^3 \frac{d}{dt} (2s_{\nu_e}(T_{\nu_e})a^3) = 0, \quad (46)$$

where the evolution of the scale factor a is determined by the Hubble rate,

$$\frac{\dot{a}}{a} = \frac{\sqrt{\rho_\gamma(T) + 2(\rho_e(T) + \rho_{\nu_e}(T_{\nu_e}) + \rho_{\nu_\mu}(T_{\nu_\mu}) + \rho_{\nu_\tau}(T_{\nu_\mu})) + \rho_S(T_{\nu_\mu}) + \rho_{Z'}(T_{\nu_\mu})}}{\sqrt{3}M_{\text{pl}}}, \quad (47)$$

and the thermally averaged width of Z' at temperature T_i is given by

$$\langle \Gamma_{Z' \rightarrow e^+e^-} \rangle_{T_i} = \Gamma_{Z'} \frac{K_1(m_{Z'}/T_i)}{K_2(m_{Z'}/T_i)}, \quad (48)$$

with $K_{1,2}$ the modified Bessel functions of the second kind. Here, s_i and ρ_i denote the entropy density and thermal equilibrium energy density (at zero chemical potential) of species i , respectively, both of which account for the internal spin degrees of freedom. For details of their forms, please refer to Appendix B of Ref. [32]. The factor of "2" preceding them accounts for its antiparticle. In Eqs. (44) and (45), detailed balance [67] is invoked to parameterize the energy transfer rate of the inverse decay $e^+e^- \rightarrow Z'$ in terms of the thermally averaged decay rate of Z' evaluated at temperature T .

Figure 4 shows the behavior of temperature ratios T/T_{ν_e} and T_{ν_μ}/T_{ν_e} using different values for the kinetic mixing parameter $|\epsilon_A| = 7.6 \times 10^{-6}$ (which corresponds to using $\epsilon_A = -[eg_{\mu\tau}/(12\pi^2)] \ln(m_\tau^2/m_\mu^2)$ with $g_{\mu\tau} = 5.2 \times 10^{-4}$), 10^{-7} , and 0, with $m_{Z'} = 12$ MeV and $m_S = 30$ MeV, while in the right panel, $m_{Z'} = 8$ MeV and $m_S = 20$ MeV. For a Z' - γ kinetic mixing parameter $|\epsilon_A| > 10^{-8}$, the $Z' \leftrightarrow e^+e^-$ interaction helps equilibrate the (γ, e^\pm) and $(\nu_\mu, \nu_\tau, S, Z')$ baths, maintaining $T = T_{\nu_\mu}$ until $T < m_e$. As the temperature drops, entropy from S and Z' is shared between these two baths. A larger $|\epsilon_A|$ extends the equilibrium period, causing T_{ν_μ}/T_{ν_e} to increase and T/T_{ν_e} to decrease.

On the other hand, for $|\epsilon_A| < 10^{-8}$, the baths decouple at a temperature of approximately 3.2 MeV, below which weak interactions cannot maintain temperature equilibrium among them. In this condition, an even smaller $|\epsilon_A|$ results in less entropy being transferred to the (γ, e^\pm) bath, while the eaten S and Z' further increase T_{ν_μ} when $T < m_e$.

In Fig. 5, we plot the resulting N_{eff} versus $m_{Z'}$ during the later stage of the Big Bang Nucleosynthesis (BBN) epoch, where we have adopted $m_S = 2m_{Z'} + 5$ MeV. The obtained N_{eff} is insensitive to m_S for our consideration of $m_S > 2m_{Z'}$. In Figs. 1 and 5, the hatched region corresponds to $3.12 \lesssim N_{\text{eff}} \lesssim 3.33$. While standard Λ CDM predicts $N_{\text{eff}}^{\text{SM}} \simeq 3.046$, an elevated value of N_{eff} is known to be positively correlated with the Hubble constant H_0 in CMB analyses, thereby reducing the tension with local measurements [68, 69]. Specifically, including a prior from local H_0 measurements favors $N_{\text{eff}} \approx 3.27 \pm 0.15$. However, we note that increasing N_{eff} is not a complete solution to all cosmological tensions. As pointed out in Ref. [62] (see Fig. 35 therein), an increase in N_{eff} tends to increase the amplitude of matter fluctuations, σ_8 , which may exacerbate the tension with weak lensing surveys that prefer a lower S_8 (or σ_8). Therefore, the parameter space highlighted here should be interpreted as alleviating the H_0 tension, with the caveat that

the σ_8 tension requires a more comprehensive discussion beyond the scope of this minimal model.

Under the constraint of $N_{\text{eff}} < 3.33$ from Planck (TT, TE, EE + lowE + lensing + BAO at 95% CL) [62], we find $m_{Z'} \gtrsim 12$ MeV for $|\epsilon_A| = 7.6 \times 10^{-6}$, and $m_{Z'} \gtrsim 7.5$ MeV for $|\epsilon_A| = 10^{-7}$. For much smaller $|\epsilon_A|$, *e.g.*, 6.5×10^{-10} , an even wider mass range, $6.9 \text{ MeV} < m_{Z'} < 16.9 \text{ MeV}$, can help relax the Hubble tension, whereas for $\epsilon_A = 0$, the favored value shifts to higher masses. Before proceeding, it is worth noting that neutrino oscillations imply rapid changes in neutrino flavor, which may equilibrate the temperatures $T_{\nu_e} \simeq T_{\nu_\mu}$. Such effects might further slightly alter the N_{eff} [34].

VII. EXCITED STATE LIFETIME, FRACTION, AND MASS SPLITTING CONSTRAINTS

For nearly degenerate DM, where the mass splitting $\delta m \equiv m_+ - m_- \ll m_\pm$, the decay of the excited state χ_+ into the ground state χ_- occurs primarily via the three-body channels $\chi_+ \rightarrow \chi_- \nu_\mu \bar{\nu}_\mu$ and $\chi_+ \rightarrow \chi_- \nu_\tau \bar{\nu}_\tau$, mediated by an off-shell Z' boson. Assuming $m_{Z'} \gg \delta m$, the decay width can be approximated as

$$\Gamma_{\chi_+} \simeq \frac{g_{\mu\tau}^2 g_\chi^2 (\delta m)^5}{10\pi^3 m_{Z'}^4}, \quad (49)$$

which is independent of m_- . The lifetime of the excited state, $\tau_+ = \Gamma_{\chi_+}^{-1}$, plays a critical role in the cosmological history. Based on the analysis in Sec. IV and Sec. V, the coupling constants are constrained to be small; specifically, we typically find $g_{\mu\tau} \lesssim 10^{-3}$ from experimental bounds and $g_\chi \sim 10^{-4}$ from the relic density requirement. Taking conservative benchmark values of $g_{\mu\tau} = 10^{-4}$ and $g_\chi = 10^{-4}$, we constrain the parameter space of δm versus $m_{Z'}$ to ensure a safe decay lifetime, as illustrated in Fig. 6.

Regarding the cosmological constraints, in the region where $\tau_+ < 1$ s, the decay of χ_+ occurs before neutrino decoupling, preventing any deviation from standard BBN predictions [70]. For the region where the lifetime is long ($\tau_+ \gg 1$ s), we estimate the impact on N_{eff} using an instantaneous injection approximation. Even in the extreme case where the decay occurs as late as the matter-radiation equality epoch ($T \sim 0.8$ eV) or the recombination epoch ($T \sim 0.3$ eV), the injected energy density from the small mass splitting (typically $\delta m \lesssim 10$ keV in this long-lived region) is minimal. Assuming $\delta m/m_- \sim 10^{-6}$, this results in a shift of the effective number of neutrino species $\Delta N_{\text{eff}} \sim 10^{-6} - 10^{-7}$, which is orders of magnitude below the sensitivity of current and future CMB experiments. Thus, the scenario is cosmologically safe.

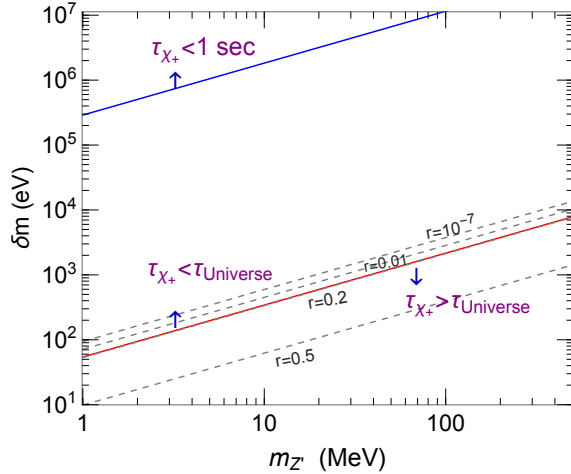


FIG. 6. Contours of the excited state lifetime τ_+ and the relic abundance fraction r (dashed lines) in the $(m_{Z'}, \delta m)$ plane. The upper solid blue line corresponds to $\tau_+ = 1$ s (approximate onset of BBN), while the lower solid red line indicates a lifetime equal to the age of the Universe ($\tau_+ \simeq 13.8$ Gyr). The gauge and dark couplings are fixed at benchmark values $g_{\mu\tau} = 10^{-4}$ and $g_\chi = 10^{-4}$. The region above the blue line represents scenarios where χ_+ decays rapidly before BBN, whereas the region below the red line corresponds to a effectively stable χ_+ .

We now estimate the relic abundance fraction of the excited state, defined as $r \equiv n_{\chi_+}/(n_{\chi_+} + n_{\chi_-})$. Before freeze-out, chemical equilibrium is maintained through inelastic scattering processes such as $\chi_\pm\chi_\pm \leftrightarrow SS, Z'Z'$ and $\chi_-\chi_+ \leftrightarrow Z'S$. Since the mass splitting is negligible compared to the freeze-out temperature ($\delta m \ll T_{fo}$), the number densities of the excited and ground states are initially equal at the time of chemical decoupling (t_{fo}), i.e., $n_{\chi_+}(t_{fo}) \simeq n_{\chi_-}(t_{fo})$.

Subsequently, as χ_+ decays into χ_- , the evolution of the comoving number density is governed by

$$d(a^3 n_{\chi_+}) \simeq -\frac{a^3 n_{\chi_+}}{\tau_+} dt. \quad (50)$$

The solution to this decay equation is

$$n_{\chi_+} = n_{\chi_+,fo} \left(\frac{a_{fo}}{a}\right)^3 e^{-(t-t_{fo})/\tau_+}, \quad (51)$$

where a_{fo} denotes the scale factor at the freeze-out time t_{fo} . Correspondingly, the comoving number density of the ground state χ_- increases as it receives the decay products

$$n_{\chi_-} = n_{\chi_-,fo} \left(\frac{a_{fo}}{a}\right)^3 + n_{\chi_+,fo} \left(\frac{a_{fo}}{a}\right)^3 \left(1 - e^{-(t-t_{fo})/\tau_+}\right). \quad (52)$$

Combining these with the initial Boltzmann distribution at freeze-out,

$$n_{\chi_{\pm}}(T_{\text{fo}}) = g_{\pm} \left(\frac{m_{\pm} T_{\text{fo}}}{2\pi} \right)^3 e^{-m_{\pm}/T_{\text{fo}}}, \quad (53)$$

where $g_+ = 2$ and $g_- = 2$ represent the internal degrees of freedom for χ_+ and χ_- , respectively, we derive the time evolution of the excited state fraction,

$$r(t) = \frac{n_{\chi_+}}{n_{\chi_+} + n_{\chi_-}} \simeq \frac{e^{-(t-t_{\text{fo}})/\tau_+}}{1 + e^{\delta m/T_{\text{fo}}}} \simeq \frac{1}{2} e^{-(t-t_{\text{fo}})/\tau_+}. \quad (54)$$

Here, we have used the property: $n_{\chi_{\pm}} \propto a^{-3}$ after freeze-out.

Fig. 6 presents the contours for r values of 0.5, 0.2, 0.01, and 10^{-7} at the present epoch. The residual fraction depends critically on the mass splitting δm ; a smaller splitting implies a longer lifetime and thus a larger residual fraction. In the limit $\delta m \ll T_{\text{fo}}$, the exponential Boltzmann factor is unity, yielding a primordial fraction of $r \simeq 0.5$. Consequently, in the region where the excited state is effectively stable ($\tau_+ \gg \tau_{\text{univ}}$), the present-day dark matter comprises an equal mixture of χ_+ and χ_- . Conversely, where $\tau_+ \ll \tau_{\text{univ}}$, the excited population has decayed, leaving χ_- as the sole dark matter component.

In Sec. X, we analyze how different values of δm influence the average dark matter self-interaction, as shown in Figs. 11 and 12. Sec. XI will further discuss the inelastic DM scattering signal related to δm and evaluate its detectability in direct detection experiments or neutron-star capture. Because the upscattering process can be subject to significant Sommerfeld enhancement, a regenerated population of χ_+ is expected to gradually accumulate near the dense centers of galaxies or clusters, offering potential implications for late-time astrophysical phenomena. Thus, Sec. XI will investigate the possibility of increasing the χ_+ number density at galaxy centers through inelastic upscattering.

VIII. SOMMERFELD EFFECTS ON THERMAL RELIC ABUNDANCE AND DARK MATTER ANNIHILATION

The Sommerfeld enhancement can significantly affect dark matter annihilation rates, potentially altering both the thermal relic density and indirect detection signals. Because dark matter particles can exchange a ladder of light scalar mediators (S) with a relatively large Yukawa coupling f prior to annihilation, the cross section can be substantially boosted. Here, we evaluate the impact of these non-perturbative effects on the relic density and indirect detection individually.

A. Dark matter relic density

In Sec. V, we estimated the dark matter yield Y neglecting Sommerfeld effects. However, as the dark matter particles become non-relativistic, the exchange of light scalars may induce a Sommerfeld enhancement. The thermal average of the effective annihilation cross-section is given by

$$\langle \sigma_{\text{eff}} v \rangle = \int S_1 \cdot (\sigma_{\text{eff}} v) f_r(v) dv, \quad (55)$$

where, from Eqs. (37), (38), (39) and Appendix E, the tree-level effective p-wave cross section is given by

$$(\sigma_{\text{eff}} v) \simeq \frac{7f^4}{384\pi m_{\mp}^2} v^2. \quad (56)$$

Here, S_1 is the Sommerfeld enhancement factor associated with the $\ell = 1$ (p -wave) partial wave state. The relative velocity distribution of the dark matter particles in the center-of-mass frame, $f_r(v)$, follows the Maxwell-Boltzmann distribution

$$f_r(v) = \sqrt{\frac{2}{\pi}} \frac{v^2}{v_0^3} e^{-\frac{v^2}{2v_0^2}} = \sqrt{\frac{2}{\pi}} \left(\frac{x_-}{2}\right)^{3/2} v^2 e^{-\frac{x_- v^2}{4}}, \quad (57)$$

where $v_0 = \sqrt{2T_{\text{DM}}/m_-}$ is the most probable velocity and $x_- = m_-/T_{\text{DM}}$. While the p -wave cross section is velocity-suppressed ($\sigma v \propto v^2$) at low temperatures, the Sommerfeld factor S_1 could partially lift this suppression, potentially requiring a readjustment of the coupling f to satisfy the observed relic density.

Summing the ladder diagrams in the calculation increases the square of the scattering amplitude by a so-called Sommerfeld factor. Considering the DM annihilation process in the center-of-mass frame, the initial DM particles are \vec{p} and $-\vec{p}$, while the final S particles possess momenta of \vec{p}' and $-\vec{p}'$. Generally, a full amplitude, A , that includes the Sommerfeld effect, is represented by an integral involving the wave function $\phi_{\vec{p}}^*(\vec{r})$ and the bare scattering amplitude, A_0 [71, 72],

$$A(\vec{p}, \vec{p}') = \int d^3r \phi_{\vec{p}}^*(\vec{r}) \int \frac{d^3q}{(2\pi)^3} e^{i\vec{q}\cdot\vec{r}} A_0(\vec{q}, \vec{p}'), \quad (58)$$

where we can further expand A , A_0 , and $\phi_{\vec{p}}^*(\vec{r})$ in partial waves,

$$A(\vec{p}, \vec{p}') = \sum_{\ell} A_{\ell}(\vec{p}, \vec{p}') = \sum_{\ell} p^{\ell} p'^{\ell} P_{\ell}(\hat{p} \cdot \hat{p}') a_{\ell}, \quad (59)$$

$$A_0(\vec{q}, \vec{p}') = \sum_{\ell} A_{0,\ell}(\vec{q}, \vec{p}') = \sum_{\ell} q^{\ell} p'^{\ell} P_{\ell}(\hat{q} \cdot \hat{p}') a_{0,\ell}, \quad (60)$$

$$\phi_{\vec{p}}^*(\vec{r}) = \frac{1}{p} \sum_{\ell} i^{\ell} (2\ell + 1) e^{i\delta_{\ell}} P_{\ell}(\hat{p} \cdot \hat{r}) \frac{\chi_{p,\ell}(\alpha_f m_- r)}{r C_{\ell}}, \quad (61)$$

with $\alpha_f = f^2/(4\pi)$ and the symbols with hats denoting the corresponding unit vectors. Here, the wave function $\chi_{p,\ell}$ satisfies the differential equation,

$$\frac{1}{m_-} \frac{d^2}{dr^2} \chi_{p,\ell} - \frac{\ell(\ell+1)}{m_- r^2} \chi_{p,\ell} + \frac{p^2}{m_-} \chi_{p,\ell} - V(r) \chi_{p,\ell} = 0, \quad (62)$$

where in the coordinate space the DM interaction through the exchange of S can be described by the Yukawa potential,

$$V(r) = -\frac{\alpha_f e^{-m_S r}}{r}. \quad (63)$$

Using the dimensionless variable $x = \alpha_f m_- r$, we can express Eq. (62) as

$$\frac{d^2}{dx^2} \chi_{p,\ell} - \frac{\ell(\ell+1)}{x^2} \chi_{p,\ell} + a^2 \chi_{p,\ell} + \frac{e^{-x/b}}{x} \chi_{p,\ell} = 0, \quad (64)$$

where

$$a = \frac{v}{2\alpha_f}, \quad b = \frac{\alpha_f m_-}{m_S}. \quad (65)$$

Following a similar derivation as in Refs. [71, 72], we obtain the ℓ -wave partial amplitude from Eq. (58),

$$A_\ell(\vec{p}, \vec{p}') \simeq \sqrt{S_\ell} A_0(\vec{p}, \vec{p}'), \quad (66)$$

where the Sommerfeld enhancement is given by

$$S_\ell = \left| \frac{(2\ell+1)!!}{C_\ell} \left(\frac{2\alpha_f}{v} \right)^{\ell+1} \right|^2. \quad (67)$$

The constant C_ℓ can be determined by

$$C_\ell^2 = [\chi_{p,\ell}(x)^2 + \chi_{p,\ell}(x - \pi/2)^2]_{|x \rightarrow \infty}. \quad (68)$$

In this paper, we consider that the DM relic density is dominated by the p -wave annihilations (see Eqs. (37)-(39)). Thus, the relevant Sommerfeld factor is given by

$$S_1 = \left| \frac{3}{C_1} \left(\frac{2\alpha_f}{v} \right)^2 \right|^2. \quad (69)$$

In Sec. V, we neglected the Sommerfeld effect, which is only significant at low velocities. The integration in Eq. (40) is dominated by a narrow region near $x = x_f$, where the dark matter particles are mildly non-relativistic. To quantify this effect, we compare the ratio of the integrand at various relative velocities to its value at $x = x_f$,

$$\frac{g_*^{1/2}(T) \langle \sigma_{\text{eff}} v \rangle(x) / (2x^2)}{g_*^{1/2}(T_{\text{fo}}) \langle \sigma_{\text{eff}} v \rangle(x_f) / (2x_f^2)}. \quad (70)$$

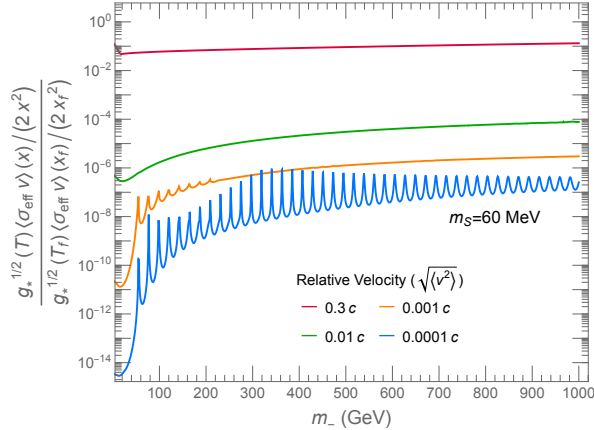


FIG. 7. The ratio of the Sommerfeld-enhanced integrand at different rms relative velocities $\sqrt{\langle v^2 \rangle}$ normalized to its value at freeze-out ($x = x_f$). The curves correspond to $\sqrt{\langle v^2 \rangle}/c = 0.3, 0.01, 0.001$, and 0.0001 (ordered from top to bottom), with the scalar mass fixed at $m_S = 60$ MeV.

These comparisons are shown in Fig. 7, examining the integrand at various relative velocities. Here, we use velocity v instead of the temperature parameter x , since dark matter becomes more non-relativistic as temperature decreases; they are related by

$$\langle v^2 \rangle = \begin{cases} \frac{6}{x}, & \text{for } x < x_{kd}, \\ \frac{6x_{kd}}{x^2} \left(\frac{h_{\text{eff}}(T)}{h_{\text{eff}}(T_{kd})} \right)^{2/3}, & \text{for } x > x_{kd}. \end{cases} \quad (71)$$

As the velocity decreases (or as x increases), the integrand drops rapidly, and this pattern continues even after considering the Sommerfeld effect. It is important to note that when the temperature falls below a certain threshold, the DM self-interaction weakens, preventing thermal equilibrium. During this period, the DM particles move freely and are non-thermal but still follow the Maxwell-Boltzmann distribution. Fig. 7 hints that for p -wave DM annihilation, even in a non-thermal state, the Sommerfeld correction has minimal impact on the relic density estimate. Therefore, including this effect does not affect the relic density results.

B. Indirect searches and constraints

Before dark matter annihilation, incident particles with low relative velocity exchange a ladder of light mediators (known as Sommerfeld enhancement effect), vastly boosting the annihilation rate. In Fig. 8, we display the p -wave Sommerfeld factor and the corresponding $\chi_- \chi_- \rightarrow SS, Z' Z'$ annihilation cross section for various non-relativistic relative velocities. Note that for a standard

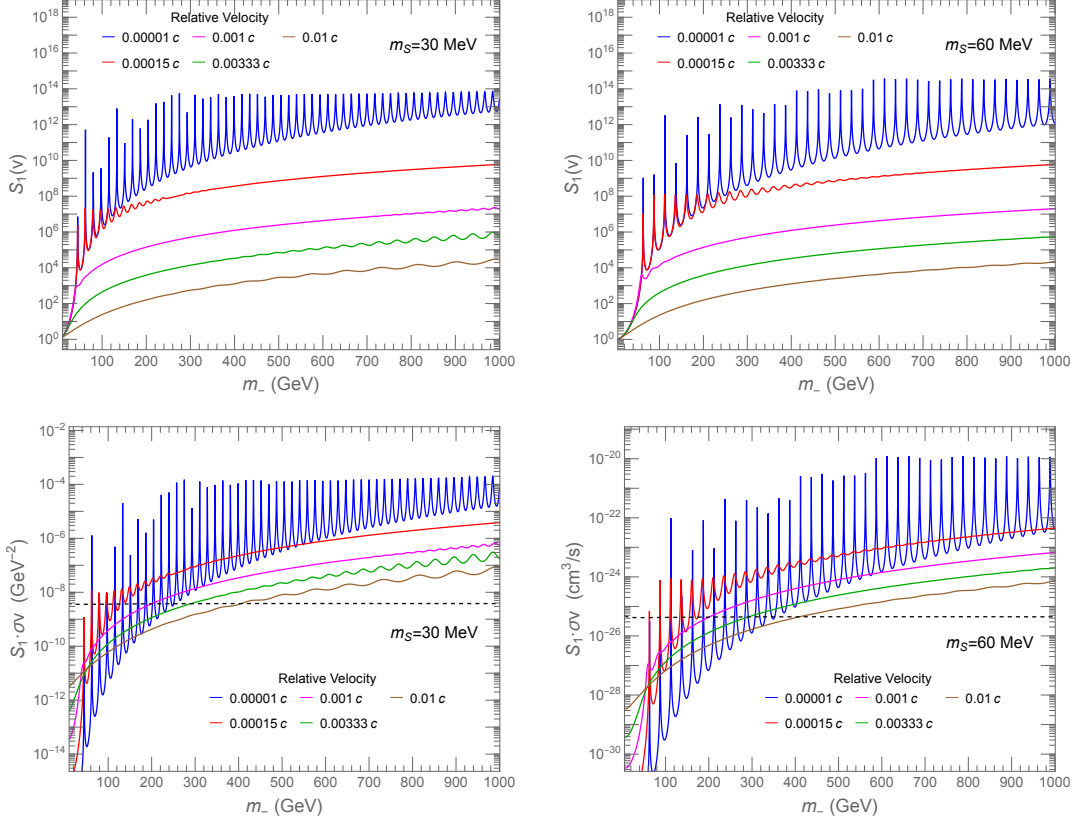


FIG. 8. Top panels: The Sommerfeld enhancement factor as a function of m_- for relative velocities $v/c = 0.00001, 0.00015, 0.001, 0.00333,$ and 0.01 . The curves are ordered from top to bottom based on their peak values within the $m_- < 1000$ GeV range. Bottom panels: The corresponding annihilation cross sections for the same set of velocities. The black dashed line indicates the $\langle\sigma_{\text{eff}}v\rangle$ value at freeze-out for the thermal relic density. The mediator mass is $m_S = 30$ MeV (left) and 60 MeV (right).

s -wave Majorana WIMP, the observed relic abundance typically requires $\langle\sigma v\rangle \sim 2 \times 10^{-26}$ cm³/s. In this section, we proceed under the assumption that dark matter is composed entirely of χ_- . If χ_+ accounts for 50%, the value of $S_1 \cdot \langle\sigma v\rangle$ in Fig. 8 will become approximately 0.7 times that of the pure χ_- case due to the statistical weighting of the available annihilation channels.

In comparison with the indirect detection constraints shown in Fig. 9, we display the annihilation cross section averaged over the velocity distribution within each small-scale structure of the Universe. The benchmark parameters are $m_{Z'}/m_S = 0.4$ with $m_S = 30$ MeV (left panel) and 60 MeV (right panel). Here, we adopt the most probable velocities of 30, 220, 700, and 1190 km/s, which correspond to the typical scales of the dwarf galaxies, local Milky Way, galaxy groups, and galaxy clusters, respectively. The regions excluded by Super-Kamiokande (yellow) [73–75],

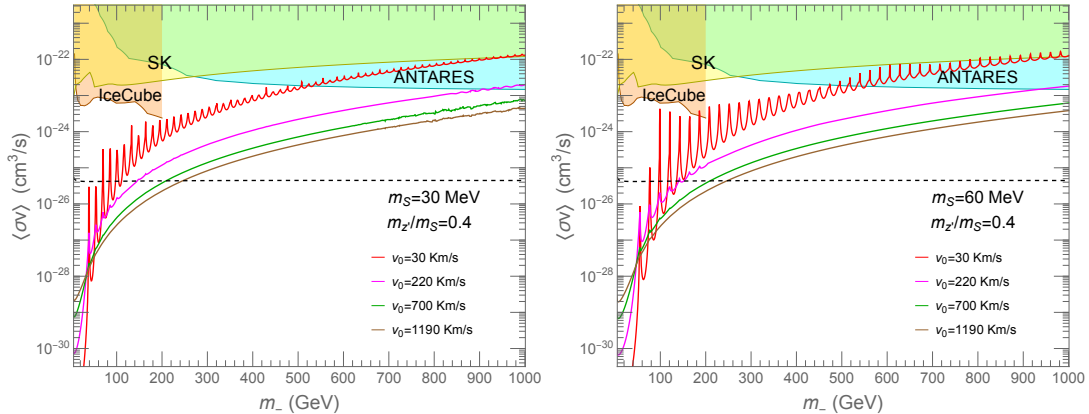


FIG. 9. Velocity-averaged annihilation cross sections for $\chi_-\chi_- \rightarrow SS, Z'Z'$ across different astrophysical scales. The curves represent most probable velocities of $v_0 = 30, 220, 700,$ and 1190 km/s (typical of dwarf galaxies, the local Milky Way, galaxy groups, and galaxy clusters), ordered from top to bottom at $m_- = 500$ GeV. Constraints from Super-Kamiokande (yellow), IceCube (orange), and ANTARES (cyan) apply only to the local Milky Way prediction (magenta curve, $v_0 = 220$ km/s). Benchmark inputs are $m_{Z'}/m_S = 0.4$ with $m_S = 30$ MeV (left) and 60 MeV (right). The black dashed line indicates the canonical cross section $\langle\sigma_{\text{eff}}v\rangle$ required for the thermal relic density.

ANTARES (cyan) [76, 77], and IceCube (orange) [78] are compared only to the magenta curve ($v_0 = 220$ km/s), which represents the prediction for the local Milky Way. These indirect searches for dark matter are constrained by the excess upper limit of high-energy muon neutrinos from the center of the Milky Way. Unlike Ref. [32], which assumes p -wave annihilations safely evade neutrino telescope bounds, our explicit inclusion of the Sommerfeld enhancement significantly boosts the late-time cross section, allowing ANTARES to exclude the heavy mass regime $m_- > 900$ GeV. This model is consistent with existing constraints for indirect detection of dark matter mass, which ranges from several GeV to hundreds of GeV. The details of these experiments, which indirectly search for dark matter, will be discussed in Appendix G.

IX. EXPERIMENTAL CONSTRAINTS ON THE MIXING ANGLE α

While a vanishing scalar-Higgs mixing angle ($\alpha = 0$) was assumed in Ref. [32] for simplicity, our study explores the more general scenario where $\alpha \neq 0$. In this section, we comprehensively investigate the phenomenological constraints on the (m_S, α) parameter space, arising from both particle physics experiments (Sec. IX A) and direct detection searches (Sec. IX B).

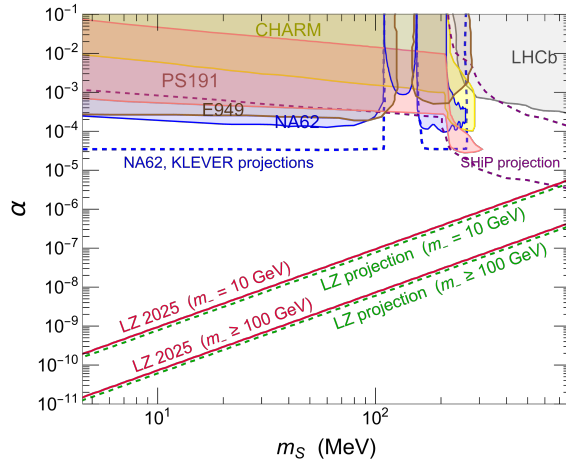


FIG. 10. Current 90% CL exclusion limits and future projections for the Higgs mixing angle α as a function of the scalar mass m_S in the sub-GeV region. Solid-colored areas with boundaries indicate parameter space excluded by particle physics experiments [79–87], while dashed boundaries show expected sensitivity projections [80, 88–92]. The robust joint constraints derived from the latest LZ 2025 direct detection results [49], as well as the future LZ projections [93], are denoted for two representative dark matter masses: $m_- = 10$ GeV and $m_- \geq 100$ GeV.

A. Particle physics experiments

Experimental signatures involving a light S in the final state are potentially detectable. Consequently, searches for missing energy from the long-lived scalar S escaping detectors, or displaced vertices in beam-dump experiments, are highly relevant [79–92]. In our model, this sub-GeV scalar S can mix with the SM Higgs boson, enabling its production in rare meson decays at colliders and fixed-target experiments. The main search for a sub-GeV scalar focuses on $K \rightarrow \pi S$, with the branching ratio depending on $\sin^2 \alpha$.

Fig. 10 shows the current experimental limits on the mixing angle in relation to the sub-GeV m_S , including reinterpretations of earlier beam-dump experiments, CHARM [79, 80] and PS191 [81–84].

The E949 [85] and NA62 [86] experiments have placed limits on a long-lived scalar S by measuring $K^+ \rightarrow \pi^+ \bar{\nu} \nu$. In this model, a weakly interacting S can be produced in the decay $K^+ \rightarrow \pi^+ S$, sharing similar experimental characteristics with the main background process $K^+ \rightarrow \pi^+ \bar{\nu} \nu$. In the 110–155 MeV range, the relevant decay chain is $K^+ \rightarrow \pi^+ \pi^0 (\gamma)$ followed by $\pi^0 \rightarrow$ invisible, which involves radiative photons in the final state. Assuming S escapes detection, NA62 has established

constraints on $\mathcal{B}(K^+ \rightarrow \pi^+ S)$ based on the 90% upper limit for the $\pi^0 \rightarrow$ invisible channel [87].

The KLEVER project aims to measure the branching ratio of the rare decay $K_L \rightarrow \pi^0 \nu \nu$ with 20% accuracy [88]. It complements the NA62 experiment, which is expected to measure the charged mode $K^+ \rightarrow \pi^+ \bar{\nu} \nu$ with about 10% precision by the end of LHC Run 3. [88, 89]. In Fig. 10, these projections are shown assuming $\mathcal{B}(K^+ \rightarrow \pi^+ S) \sim 2 \times 10^{-12}$. The SHiP experiment can reconstruct final states with two charged tracks. We also present the projected sensitivity of SHiP for a scalar decaying into two charged particles [90, 91], as reanalyzed by Winkler [80].

B. Direct detections

In our model, direct detection imposes stringent limits on the mixing angle α , which can surpass beam-dump bounds. Here, we focus on coherent elastic scattering with the target nucleus via t -channel scalar (S, h) exchange, leaving inelastic Z' interactions to Sec. XI. Conventionally, experimental limits are reported as the normalized spin-independent cross section on a single nucleon, σ_{SI}^N , which is given by

$$\sigma_{\text{SI}}^N = \left(\frac{m_{\mp} m_N}{m_{\mp} + m_N} \right)^2 \frac{f_N^2 f^2 \sin^2 2\alpha}{16\pi v_H^2} \left(\frac{1}{m_S^2} - \frac{1}{m_h^2} \right)^2 \quad (72)$$

$$\simeq \frac{\mu_{\chi N}^2 f_N^2 f^2 \sin^2 2\alpha}{16\pi v_H^2 m_S^4} \quad \text{for } m_S \ll m_h, \quad (73)$$

where $\mu_{\chi N}$ is the DM-nucleon reduced mass, m_N is the nucleon mass, v_H is the Higgs vacuum expectation value, and $f_N \simeq 0.3$ is the effective nucleon coupling [94].

Because the cross section exhibits a strong inverse-quartic dependence on the scalar mediator mass ($\sigma_{\text{SI}}^N \propto 1/m_S^4$), direct detection experiments place severe joint constraints on the (m_S, α) parameter space, demanding a highly suppressed mixing angle particularly for lighter S . Furthermore, although $\mu_{\chi N}$ saturates for $m_- \gg m_N$, the cross section retains a dependence on the dark matter mass through the coupling f , which scales as $f \propto m_-^{1/2}$ to satisfy the thermal relic density constraint (i.e., $\sigma_{\text{SI}}^N \propto f^2 \propto m_-$). For sufficiently large dark matter masses ($m_- \gtrsim 100$ GeV), this linear growth in the theoretical cross section ($\sigma_{\text{SI}}^N \propto m_-$) is perfectly canceled by the linear scaling of the experimental limit ($\sigma_{\text{limit}} \propto m_-$). Consequently, the upper bound on the mixing angle α becomes essentially independent of m_- , rendering the limits robust and universal in the heavy mass regime.

Figure 10 displays these stringent upper bounds on α as a function of m_S , based on the recent results from the LUX-ZEPLIN (LZ) experiment (LZ 2025) [49]. While results from PandaX-4T

[95] and XENONnT [96] provide competitive but slightly less stringent constraints, LZ 2025 currently serves as the leading representative benchmark. Since the resolution of small-scale structure problems typically favors $m_- \sim 10$ GeV (see Sec. X), we select $m_- = 10$ GeV and $m_- \geq 100$ GeV as two representative benchmarks. This comparison illustrates the sensitivity of the results to the dark matter mass, noting that the limits saturate for $m_- \geq 100$ GeV. As depicted in the figure, the LZ 2025 results set an overwhelmingly more stringent limit on α than colliders or fixed-target experiments across the entire sub-GeV region. For instance, at $m_S = 50$ MeV with $m_- \geq 100$ GeV, the mixing angle is severely restricted to $\alpha \lesssim 10^{-10}$. The projected sensitivity for the future LZ upgrade [93] is also shown by the dashed lines for comparison.

X. SELF-SCATTERINGS OF DARK MATTER AND THE SMALL-SCALE STRUCTURE PROBLEMS

Self-interacting dark matter (SIDM) was introduced to address small-scale structure challenges that conflict with collisionless cold dark matter (CDM) predictions, particularly the core-cusp and too-big-to-fail problems [26, 27, 97].

Dark matter self-interactions transfer heat toward the central regions of halos, flattening the core density profile. Lowering the central density of Milky Way subhalos addresses the "too big to fail" problem, while the resulting flattened density cores in low-mass galaxies naturally explain their observed rotation curves, resolving the core-cusp issue. Although the scarcity of satellite galaxies (the "missing satellites" problem) is now primarily attributed to baryonic feedback, self-interactions can still impact the subhalo mass function [26]. More importantly, SIDM provides a robust mechanism to explain the observed structural diversity of galaxies. Depending on the halo formation history, galaxies with the same maximum circular velocity can exhibit significant variations in their central densities, leading to the diverse internal rotation curves observed in similar-mass galaxies [26, 28].

In this model, DM particles mainly interact through the exchange of a scalar particle, S . As they become nonrelativistic, these scattering processes can be described by the attractive Yukawa potential given in Eq. (63). The potential strength is characterized by the dark fine-structure constant $\alpha_f = f^2/(4\pi)$, where the coupling constant f (shown in Fig. 2) is fixed to generate the correct DM relic density. The $\chi_-\chi_+$ scattering amplitude can be expressed as a sum over partial

waves,

$$f(\theta) = \sum_{\ell=0}^{\infty} f_{\ell}(\theta) \equiv \frac{2}{m_{-v}} \sum_{\ell=0}^{\infty} (2\ell + 1) e^{i\delta_{\ell}} P_{\ell}(\cos \theta) \sin \delta_{\ell}, \quad (74)$$

where θ represents the scattering angle in the center-of-mass frame. The resulting differential cross section is given by

$$\left(\frac{d\sigma}{d\Omega} \right)_{-+} = |f(\theta)|^2. \quad (75)$$

When two identical, unpolarized particles interact, such as the $\chi_{-}\chi_{-}$ and $\chi_{+}\chi_{+}$ pairs, the result includes a spin-singlet state with a symmetric spatial wave function and a spin-triplet state with an antisymmetric spatial wave function. Considering that the spin-singlet state has a statistical weight of 1/4 and the spin-triplet state has a weight of 3/4, and that $f_{\ell}(\pi - \theta) = (-1)^{\ell} f_{\ell}(\theta)$, the differential cross section for scattering of the $\chi_{-}\chi_{-}$ pair is

$$\left(\frac{d\sigma}{d\Omega} \right)_{--} = \frac{1}{2} \left(\left| \sum_{\text{even}} f_{\ell}(\theta) \right|^2 + 3 \left| \sum_{\text{odd}} f_{\ell}(\theta) \right|^2 \right), \quad (76)$$

while for the $\chi_{+}\chi_{+}$ pair, it is

$$\left(\frac{d\sigma}{d\Omega} \right)_{++} \simeq \left(\frac{d\sigma}{d\Omega} \right)_{--}, \quad \text{for } \delta m \ll m_{-}, \quad (77)$$

including a factor of 1/2 to prevent double-counting of identical initial states. In these expressions, the phase shifts δ_{ℓ} encode the dependence on the model parameters, specifically the coupling f and the mediator mass m_S . These shifts are determined by solving the radial Schrödinger equation Eq. (64) with the attractive Yukawa potential $V(r) = -\frac{\alpha_f}{r} e^{-m_S r}$, where the dark fine-structure constant is $\alpha_f = f^2/4\pi$. By matching the numerical solution of the wavefunction to its asymptotic form, following the method outlined in Ref. [98], we extract the value of δ_{ℓ} for each partial wave.

Our focus is on astronomical phenomena arising from dark matter self-scattering. These phenomena involve DM particles interacting with the DM background, causing them to lose momentum in the forward direction or energy perpendicular to their trajectory. The former is associated with the transfer cross-section σ_T , and the latter with the viscosity cross-section σ_V . In this paper, we analyze related issues using the transfer cross-section. When χ_{-} is scattered by χ_{+} , the transfer cross-section is

$$\sigma_{\text{T}}^{-+} = 2\pi \int_{-1}^1 \left(\frac{d\sigma}{d\Omega} \right)_{-+} (1 - \cos \theta) d \cos \theta. \quad (78)$$

Conversely, when χ_{+} is scattered by χ_{-} , the result is $\sigma_{\text{T}}^{+-} = \sigma_{\text{T}}^{-+}$. These scatterings involve two distinguishable particles. However, for scattering between indistinguishable particles, such as

$\chi_-\chi_-$ and $\chi_+\chi_+$, because the differential cross section remains unchanged under $\theta \leftrightarrow \pi - \theta$, the definition of the transfer cross section that describes the momentum reduction rate along the direction of motion due to scattering should be modified accordingly [99, 100], with

$$\sigma_{\text{T}}^{++} = \sigma_{\text{T}}^{--} = 4\pi \int_0^1 \left(\frac{d\sigma}{d\Omega} \right)_{--} (1 - \cos\theta) d\cos\theta. \quad (79)$$

Moreover, for a dark matter system involving both χ_+ and χ_- , the average transfer cross section is

$$\begin{aligned} \sigma_{\text{T}} &= (1-r)^2 \sigma_{\text{T}}^{--} + r^2 \sigma_{\text{T}}^{++} + r(1-r) \sigma_{\text{T}}^{-+} + r(1-r) \sigma_{\text{T}}^{+-} \\ &\simeq (1-2r+2r^2) \sigma_{\text{T}}^{--} + 2r(1-r) \sigma_{\text{T}}^{-+} \quad \text{for } \delta m \ll m_-, \end{aligned} \quad (80)$$

where r is the number fraction of χ_+ in all dark matter, as defined in Eq. (54). The average transfer cross section is weighted by the number density fractions of the interacting species. The quantum mechanical effects of identical initial states are properly incorporated, as shown in Eq. (76). This averaged definition (Eq. (80)) is consistent with the treatments in Refs. [32, 101, 102] for the limiting cases of $r = 0$ and $r = 0.5$.

A successful self-interacting DM model must accommodate the diverse structures of DM halos across vastly different astrophysical scales. To resolve small-scale controversies, the cross section is typically required to be around $\sigma_{\text{T}}/m_- \sim \mathcal{O}(1-10) \text{ cm}^2/\text{g}$ at the scales of dwarf spheroidal galaxies [26, 103, 104] and low-surface-brightness (LSB) spirals [28]. Conversely, at the scales of massive galaxy clusters and groups, the cross section must be significantly smaller—typically restricted to $\sigma_{\text{T}}/m_- \lesssim 0.1 - 0.5 \text{ cm}^2/\text{g}$ for clusters, and $\sigma_{\text{T}}/m_- \lesssim 1.1 \text{ cm}^2/\text{g}$ for groups—to remain consistent with various astronomical estimates, halo shape analyses, and cluster collision observations [26–28, 105–111]. Our model naturally achieves this requisite velocity dependence through resonant Sommerfeld enhancement.

To further investigate the kinetic properties of the model, we select specific dark matter mass values—corresponding to the resonance peaks identified in the left panels—that best align with observational constraints for presentation. The resulting velocity-weighted cross sections, $\langle \sigma_{\text{T}} v \rangle / m_-$, are illustrated as a function of the average relative velocity $\langle v \rangle$ in the right panels of Fig. 11 (for the scenario with $r = 0.5$). To obtain these curves, we assume that the relative velocities of dark matter particles follow a Maxwell-Boltzmann distribution, as given by Eq. (57), and calculate the statistical average of the velocity-weighted cross section. Under this distribution, the average collision velocity $\langle v \rangle$ on the horizontal axis is related to the most probable velocity v_0 by $\langle v \rangle = 2\sqrt{2/\pi}v_0$. As clearly illustrated in the figures, $\langle \sigma_{\text{T}} v \rangle / m_-$ exhibits a profound dependence on $\langle v \rangle$ due to the underlying resonant structures.

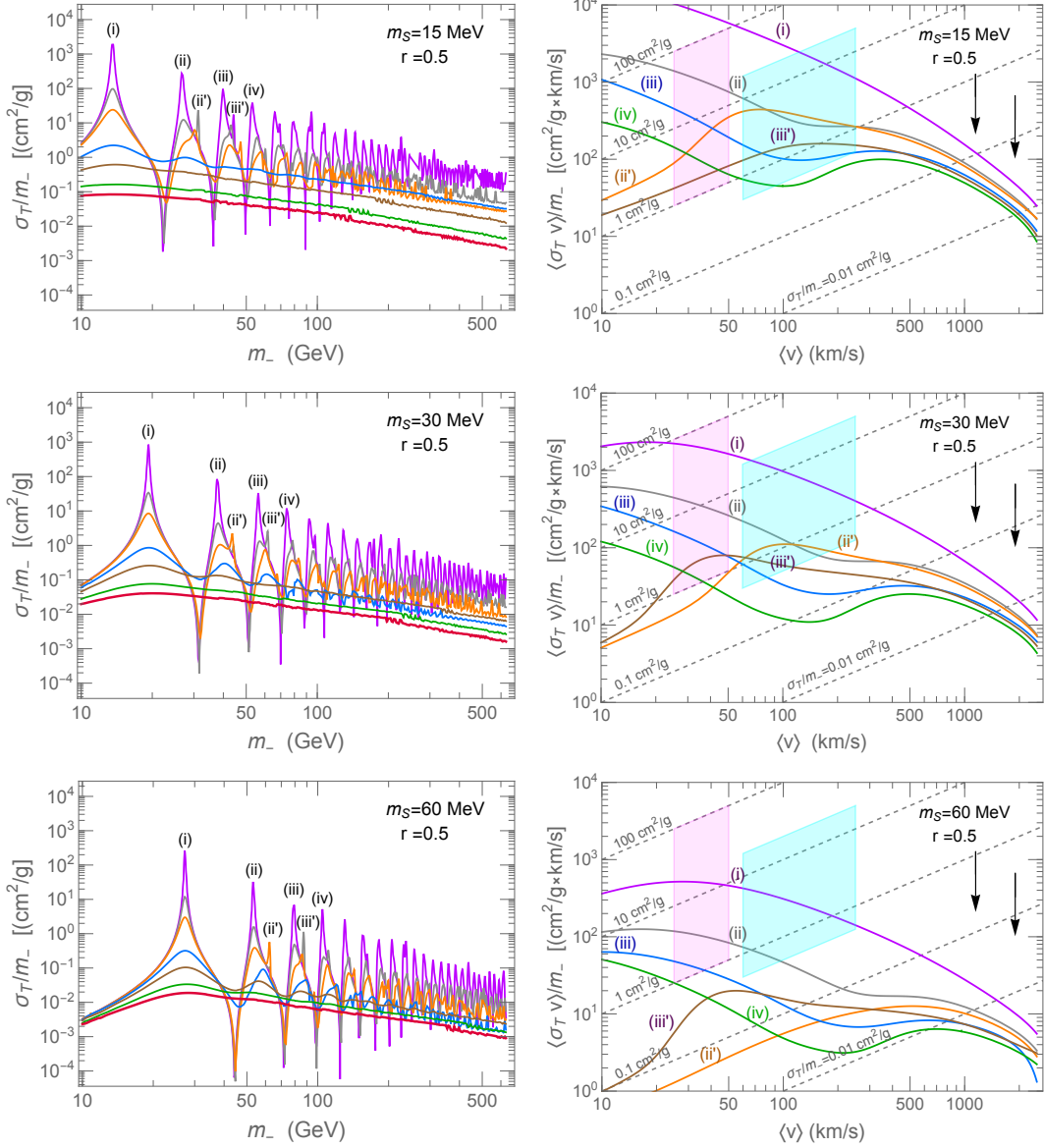


FIG. 11. Left panels: The transfer cross section per unit mass σ_T/m_- as a function of the dark matter mass m_- for various mediator masses m_S , assuming $r = 0.5$. Right panels: The velocity-weighted cross section $\langle\sigma_T v\rangle/m_-$ vs. the average relative velocity $\langle v\rangle$. The solid curves, labeled (i)-(iv) and (ii')-(iii'), correspond respectively to the primary and secondary resonant masses identified in the left panels. Diagonal dashed lines represent contours of constant σ_T/m_- . We compare the results with updated astrophysical constraints and theoretically favored regions: the stringent upper limits on galaxy groups ($\sigma_T/m_- \lesssim 1.1$ cm^2/g) and massive clusters ($\sigma_T/m_- \lesssim 0.35$ cm^2/g) indicated by downward arrows [106]; the parameter space favored by LSB spiral galaxies (central shaded box) [28]; and the broad favored region for dwarf galaxies encompassing both standard core formation [26] and the onset of gravothermal collapse/diversity [103, 104] (left shaded region).

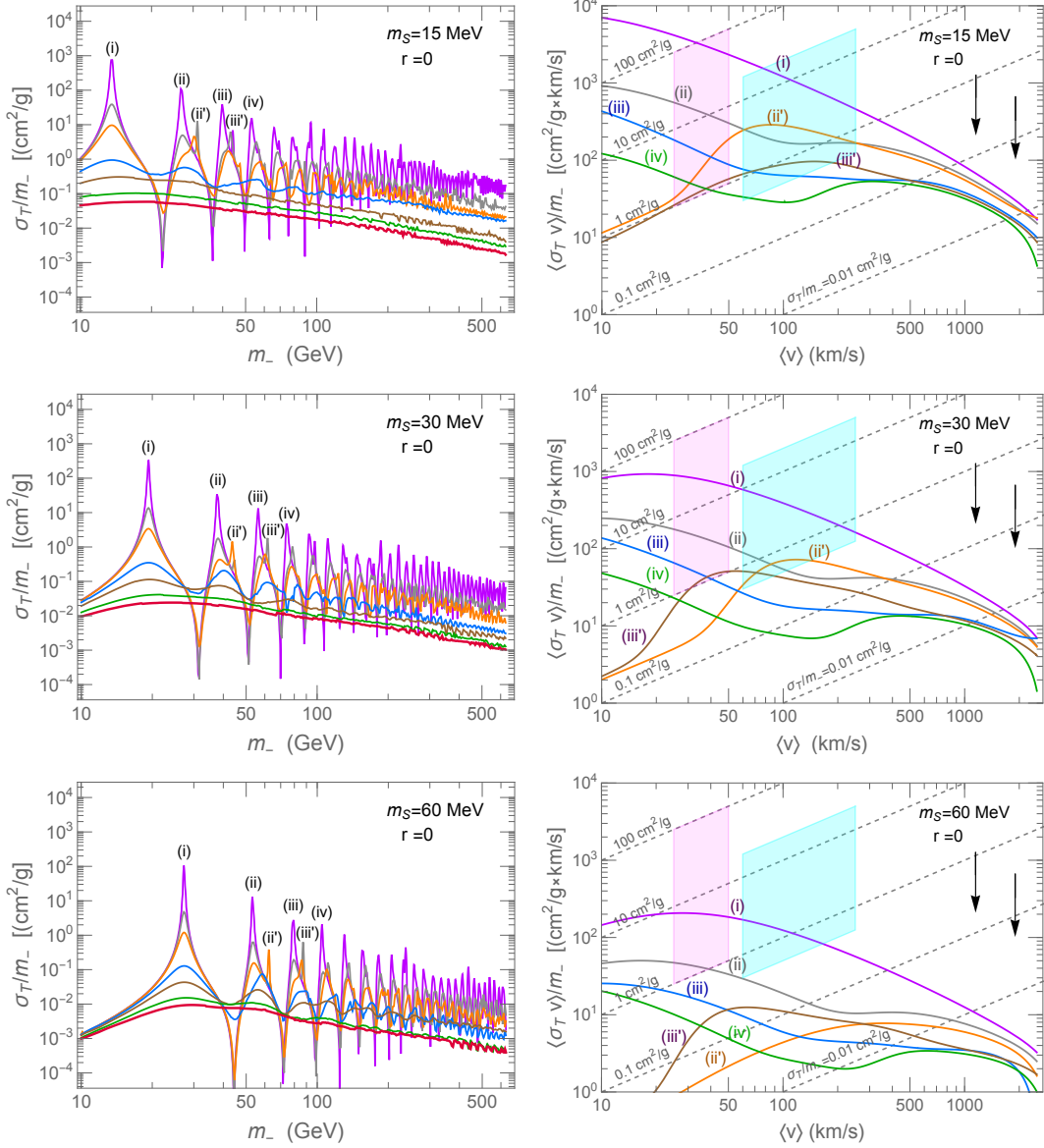


FIG. 12. Same as Fig. 11, but for $r = 0$. The overall kinematic behavior is similar to the $r = 0.5$ case, but the effective cross sections are suppressed by a relative factor of approximately 0.4, which subsequently requires tuning closer to the exact resonance peaks to satisfy the dwarf-scale favored regions.

The motivation for plotting this specific rate stems from the dynamics of halo core formation. As pointed out in Ref. [28], the inner density ρ of a galaxy halo is intrinsically linked to its age t_{age} . Within the characteristic radius of a thermalized core, the condition $\langle \sigma_T v \rangle \rho / m_- \cdot t_{\text{age}} \gtrsim 1$ holds, indicating that each dark matter particle has, on average, undergone at least one scattering event since formation. Here, the transfer cross section σ_T is strictly used to appropriately account for

the forward momentum loss. Because the characteristic DM velocities vary by orders of magnitude across different galactic systems—from dwarf galaxies to massive clusters—the efficacy of this scattering rate, and hence the DM self-interaction, must strongly depend on velocity.

A detailed analysis of the kinematic behavior reveals distinct features between the primary resonances (e.g., curves (i)-(iv)) and the secondary resonances (e.g., curves (ii') and (iii')). For the primary resonant masses, the cross section increases significantly as $\langle v \rangle$ decreases from cluster scales down to dwarf scales. Interestingly, for certain primary resonances (such as those in the $m_S = 30$ and 60 MeV scenarios), the velocity-weighted cross section $\langle \sigma_T v \rangle / m_-$ reaches a local maximum around $\langle v \rangle \sim 20\text{--}25$ km/s and exhibits a slight decrease as $\langle v \rangle$ approaches 10 km/s. It is worth noting that while the rate $\langle \sigma_T v \rangle / m_-$ shows this non-monotonic behavior, the intrinsic cross section σ_T / m_- remains monotonically increasing as $\langle v \rangle$ decreases, crossing the constant σ / m contours. In contrast, for secondary resonances, the cross section tends to saturate and approaches a constant value at $\langle v \rangle \rightarrow 10$ km/s.

In the dwarf galaxy regime ($\langle v \rangle \sim 30\text{--}50$ km/s), satisfying the canonical values for standard core formation [26, 28] requires the model parameters to be tuned near these discrete resonance peaks. The mediator mass, m_S , plays a crucial role in determining the density of these available peaks. For a lighter mediator ($m_S \sim 15\text{--}30$ MeV), the resonance peaks are more densely distributed along the dark matter mass spectrum. Consequently, within the range of $m_- \approx 20\text{--}75$ GeV, there are numerous distinct resonant values that successfully fall within the favored region (shaded areas). Notably, for lighter resonant dark matter ($10 \text{ GeV} \lesssim m_- \lesssim 40 \text{ GeV}$) coupled with a relatively light mediator ($m_S \lesssim 30$ MeV), the cross section can reach values as high as $\sigma_T / m_- \sim 10 \text{ cm}^2/\text{g}$. This enhancement aligns with the requirements for initiating gravothermal collapse, providing a natural explanation for the observed diversity in Milky Way satellites [103, 104].

Conversely, for a heavier mediator ($m_S \sim 60$ MeV), the resonance peaks become much sparser. To satisfy the canonical core formation constraints in this scenario, the dark matter mass cannot take arbitrary values; it must be strictly fine-tuned to the specific vicinity of the sparse primary resonances, namely $m_- \approx 26.9, 53.7, \text{ or } 79.4$ GeV, while simultaneously avoiding the stringent upper limits at galaxy group and cluster scales ($\langle v \rangle \gtrsim 1000$ km/s) [106].

Finally, we illustrate the scenario for $r = 0$ in Fig. 12. While the qualitative velocity dependence mirrors that of the $r = 0.5$ case, the magnitude of the effective cross section is uniformly suppressed by a factor of approximately 0.4. As a result of this overall suppression, meeting the aforementioned observational and theoretical thresholds [27] generally requires tuning the dark matter mass even closer to the exact resonance peaks, or shifting towards lower mediator masses. In summary, the

desired velocity-dependent trend—large cross sections at dwarf scales and suppressed values at cluster scales—becomes more pronounced and easier to achieve without extreme fine-tuning when a much smaller mediator mass (m_S) is used, or when the proportion of χ_+ particles in the dark sector (i.e., a higher r value) is larger.

XI. DISCUSSIONS

Below, we examine potential experimental signatures and observational consequences that may further probe and test the viability of this model.

$\mu N \rightarrow \mu N Z'$

This model suggests that Z' bosons could be generated via the bremsstrahlung process $\mu N \rightarrow \mu N Z'$ when a high-energy muon beam strikes a fixed target. For instance, the NA64 μ experiment, employing a 160 GeV muon beam, projects that with 10^{11} muons on target (MOTs), its 90% C.L. upper limit for the gauge coupling $g_{\mu\tau}$ could be reduced to below 3×10^{-4} for $m_{Z'} = 1 - 300$ MeV [112]. Additionally, Fermilab's M^3 (Muon Missing Momentum) experiment aims to investigate a similar parameter space in its Phase 1 projection [113]. Given the recent update on the SM prediction, which essentially resolves the longstanding $(g - 2)_\mu$ anomaly, the allowed $L_\mu - L_\tau$ contribution is no longer restricted to a narrow favored band but is instead simply bounded by an upper limit. Consequently, the projected sensitivities of these future experiments will be crucial for thoroughly exploring this much broader viable parameter space.

Spin-dependent inelastic scattering via Z' exchange

The direct detection of the inelastic DM discussed here primarily depends on the dark sector gauge coupling g_χ , the kinetic mixing parameter ϵ_A , and the inelastic mass splitting δm . To evaluate the collision rate between dark matter and target nuclei in direct detection experiments, we consider the inelastic scattering cross section of dark matter with nucleons. The relevant Lagrangian, derived from Eq. (22), is

$$\mathcal{L} \supset -g_\chi J_D^\mu Z'_\mu + \epsilon_A e J_\gamma^\mu Z'_\mu - \epsilon_Z \frac{m_{Z'}^2}{m_Z^2 - m_{Z'}^2} g_Z J_Z^\mu Z'_\mu. \quad (81)$$

Since $m_{Z'}$ is much smaller than m_Z , the third term is safely negligible. The electromagnetic current J_γ^μ is further reformulated from the quark level to the nucleon level [114], yielding

$$\epsilon_A e J_\gamma^\mu \rightarrow \epsilon_A e \bar{p} \gamma_\mu p, \quad (82)$$

which indicates that Z' couples solely to protons. Consequently, Z' mediates spin-dependent (SD) inelastic scattering between the Majorana dark matter and protons. This interaction can be

categorized into two types: exothermic inelastic scattering ($\chi_{+p} \rightarrow \chi_{-p}$) [115, 116] and endothermic inelastic scattering ($\chi_{-p} \rightarrow \chi_{+p}$) [116]. The differential cross section for $\chi_{\pm p} \rightarrow \chi_{\mp p}$ is given by

$$\sigma_{\chi_{\pm p}}^{\text{SD}} \simeq g_{\chi}^2 \epsilon_A^2 e^2 \left(v^2 \frac{(3m_{Z'}^2 \mp 40\delta m m_p) m_p^2}{2\pi m_{Z'}^6} \pm \frac{3\delta m m_p}{\pi m_{Z'}^4} \right) \quad (83)$$

where v is the velocity of the incident dark matter. For a scattering event with recoil energy E_R to be kinematically allowed, the incoming dark matter velocity must exceed a minimum threshold v_{min} , given by

$$v_{\text{min}} = \sqrt{\frac{1}{2m_p E_R} \left(\frac{m_p E_R}{\mu_{\chi p}} \mp \delta m \right)}, \quad (84)$$

with $\mu_{\chi p}$ as the reduced mass of the two colliding particles.⁴

While Eq. (84) strictly limits the available kinematic phase space, Eq. (83) explicitly shows that the scattering cross section itself is further suppressed, approaching zero in the limits $\delta m \rightarrow 0$ and $v \rightarrow 0$. More importantly, since the dark sector coupling is constrained to be very small ($g_{\chi} \lesssim 10^{-3}$, as derived in Sec. V) and the kinetic mixing ϵ_A is tightly bounded (as constrained by cosmology and loop-induced relations discussed earlier), the resulting event rate is expected to be overwhelmingly small, lying well below the sensitivity of current and near-future direct detection experiments.

In the pseudo-Dirac model [32], accommodating the past $(g-2)_{\mu}$ anomaly and self-interactions requires a large mass splitting ($\sim \mathcal{O}(1)$ GeV), which kinematically forbids SD scattering. Conversely, our axial-vector interaction heavily velocity-suppresses the SD rate, naturally evading limits despite a tiny mass splitting.

Inelastic capture of dark matter in neutron stars

Neutron stars typically contain significant fractions of muons, with the muon-to-neutron number ratio ranging from 1% to 10% [118–120]. The rate at which a neutron star captures dark matter depends on the differential cross section of inelastic dark matter scattering off these muons ($\chi_{\pm\mu} \rightarrow \chi_{\mp\mu}$), mediated via t -channel Z' exchange. Dark matter particles are captured once their velocity falls below the escape velocity, v_{esc} , analogous to the capture mechanisms in the Sun or Earth [121–124].

For a dark matter particle initially traveling with velocity v far from the neutron star, its differential scattering cross section in the non-relativistic limit, after falling into the gravitational

⁴ In experimental studies of dark matter interactions, it is necessary to account for the entire target nucleus, replacing the proton mass with the nuclear mass. Furthermore, the nuclear form factor [114, 117] must be incorporated into the calculation of the scattering rate, which intricately depends on the momentum transfer. Nevertheless, the simplified estimates here still provide valuable kinematic insights.

potential and colliding with a muon, can be written as

$$\begin{aligned} & \frac{d\sigma}{dE_R}(\chi_{\mp}\mu \rightarrow \chi_{\pm}\mu) \\ & \simeq \frac{g_{\chi}^2 g_{\mu\tau}^2}{4\pi w^2} \frac{m_{\mu}}{(2E_R m_{\mu} + m_{Z'}^2)^2} \left[\frac{E_R}{m_{\mu}} \left(1 - 2\frac{m_{\mu}}{m_{-}} - \frac{m_{\mu}^2}{m_{-}^2} \right) + 2\frac{\delta m}{m_{\mu}} \left(1 + \frac{m_{\mu}}{m_{-}} \right) + 2w^2 \right], \end{aligned} \quad (85)$$

in the muon rest frame, where E_R is the recoil energy of the muon, $w = \sqrt{v^2 + v_{\text{esc}}^2}$, and the minimum velocity required for the process to occur must satisfy

$$v_{\text{min}}^2 = w_{\text{min}}^2 - v_{\text{esc}}^2 = \left(\sqrt{\frac{1}{2m_{\mu}E_R}} \left(\frac{m_{\mu}E_R}{\mu_{\chi\mu}} \mp \delta m \right) \right)^2 - v_{\text{esc}}^2, \quad (86)$$

with $\mu_{\chi\mu}$ the reduced mass of the two incident particles, χ_{-} (or χ_{+}) and μ .

Ref. [125] explored the neutron star capture of Dirac dark matter and its potential detection strategies. In our framework, comparing Eq. (85) with the findings in Ref. [125] reveals that the differential cross section for Majorana DM is significantly smaller, being parametrically suppressed by factors such as E_R/m_{μ} , $\delta m/m_{\mu}$, and w^2 . As a result, the prospects of detecting this specific dark matter candidate using compact stars remain quite limited.

Inelastic upscattering across different galaxy systems

In a galaxy or cluster system that has reached dynamical equilibrium through virialization, the characteristic temperature near its center may exceed the dark matter mass splitting (δm). According to Ref. [14], the relatively high DM temperature near the center of the Milky Way allows χ_{-} to be kinetically upscattered into the χ_{+} state. Assuming an initially negligible χ_{+} abundance, the number density of χ_{+} evolves toward an equilibrium state denoted by

$$n_{\chi_{+}} \simeq n_{\chi_{-}} \min(n_{\chi_{-}} \langle \sigma v \rangle_{\chi_{-}\chi_{-} \rightarrow \chi_{+}\chi_{+}} t_{\text{mw}}, e^{-\delta m/T_{\text{mw}}}), \quad (87)$$

where t_{mw} represents the age of the Milky Way and T_{mw} is the local temperature. Once the upscattering process thermalizes the χ_{+} population, the detailed balance condition yields $n_{\chi_{-}} \langle \sigma v \rangle_{\chi_{+}\chi_{+} \rightarrow \chi_{-}\chi_{-}} t \gtrsim e^{\delta m/T_{\text{mw}}}$.

Finally, the presence of the nearly degenerate χ_{+} state opens unique, albeit challenging, avenues for indirect detection. While the local χ_{+} population can be replenished through Sommerfeld-enhanced upscattering ($\chi_{-}\chi_{-} \rightarrow \chi_{+}\chi_{+}$) in dense galactic environments, detecting their subsequent annihilations (e.g., $\chi_{+}\chi_{-} \rightarrow Z'S$) is highly nontrivial. Any visible signals resulting from the cascade decays of S (such as into $e^{+}e^{-}$ or $\gamma\gamma$ via Higgs mixing) would have to be disentangled from the primary $\chi_{-}\chi_{-} \rightarrow SS$ background. A detailed analysis of these complex indirect detection signatures is left for a dedicated future study.

XII. SUMMARY

We have investigated a nearly degenerate Majorana dark matter model based on a $U(1)_{L_\mu-L_\tau}$ gauge extension of the Standard Model. Following SSB, two nearly degenerate Majorana dark matter particles, χ_- and χ_+ , are formed. The $U(1)_{L_\mu-L_\tau}$ gauge boson, Z' , gains mass through symmetry breaking and interacts with muons, taus, and their corresponding neutrinos. While this interaction was historically proposed to explain the observed past deviation in the muon anomalous magnetic moment $(g-2)_\mu$, recent updates to the Standard Model prediction have essentially resolved this anomaly. Consequently, the $L_\mu - L_\tau$ contribution is now tightly constrained by new upper limits. Remarkably, our model's parameters naturally accommodate these stringent bounds while remaining fully consistent with a wide array of experimental, cosmological, and astronomical data.

The Z' gauge boson acts as a portal, interacting with particles in the dark sector. Due to SSB, the dark sector fermions split into the two Majorana states (χ_\pm) with masses ranging from about 10 GeV to hundreds of GeV. A tiny Dirac mass term introduces a small mass splitting (δm) between them. The scalar particle S , which drives the spontaneous symmetry breaking in the dark sector, has a mass around the MeV scale and is crucial for the thermal evolution, relic abundance, and self-interaction of dark matter. The main features and findings of this model are summarized below:

- **Updated $(g-2)_\mu$ constraints:** We have examined the parameter space in light of the updated $(g-2)_\mu$ results [43]. The reduced Δa_μ value implies that the $L_\mu - L_\tau$ model remains a robust scenario, provided the gauge coupling $g_{\mu\tau}$ is sufficiently small. This smaller coupling comfortably satisfies the stringent bounds from neutrino trident production (CCFR) and collider searches (BABAR). Regarding other low-energy constraints (such as white dwarf cooling and Borexino), they impose restrictions on $g_{\mu\tau}$ and $m_{Z'}$ via kinetic mixing. However, since these mixing effects may be influenced by primordial contributions from higher energy scales (Sec. II C), the reliability of these limits in the $m_{Z'} \sim 10$ MeV region (Fig. 1) is highly sensitive to the underlying UV physics. Future fixed-target experiments like NA64 μ and M³ will be crucial to thoroughly investigate the much broader parameter space allowed by the new $(g-2)_\mu$ upper bounds (Sec. XI).
- **Thermal history and Hubble tension:** During the early thermal evolution, S and Z' remain in equilibrium with ν_μ and ν_τ . Because Z' can mix with photons at the one-loop

level, its decay $Z' \rightarrow e^+e^-$ helps maintain thermal balance with the SM electromagnetic bath. About one second after the Big Bang, this decay process facilitates entropy transfer between the neutrino and electromagnetic sectors (Sec. VI). This dynamic alters the effective number of relativistic species (N_{eff}) (Fig. 5) and offers a mechanism to alleviate the cosmological Hubble tension (Fig. 1).

- Freeze-out dynamics:** The dark matter relic abundance is governed by annihilations into scalars and gauge bosons ($\chi_{\mp}\chi_{\mp} \rightarrow SS, Z'Z'$ and $\chi_{-}\chi_{+} \rightarrow SZ'$), with the scalar channel playing the dominant role. A relatively large coupling constant f between DM and S ensures the correct relic density (Sec. V) and drives significant DM self-interactions. Our analysis demonstrates that the derived dark sector gauge coupling g_{χ} generally remains very small ($g_{\chi} \lesssim 10^{-3}$).
- Inelastic upscattering and detection prospects:** The Sommerfeld-enhanced upscattering in dense halos can locally replenish the excited state χ_{+} . While distinguishing its subsequent annihilation signals from the dominant χ_{-} background presents a significant observational challenge, it provides a unique phenomenological feature of the nearly degenerate mass spectrum.
- Neutrino limits from Sommerfeld enhancement:** Although the late-time dark matter annihilations ($\chi_{\mp}\chi_{\mp} \rightarrow SS, Z'Z'$ and $\chi_{-}\chi_{+} \rightarrow SZ'$) are generally p -wave suppressed, the exchange of light S particles induces a significant Sommerfeld enhancement across all these channels (Sec. VIII B). To derive the neutrino limits, we focus on the baseline scenario where the current dark matter relic is predominantly χ_{-} . By comprehensively accounting for the cascade decays of the produced S and Z' bosons from the $\chi_{-}\chi_{-} \rightarrow SS$ and $Z'Z'$ processes, we confront our theoretical neutrino spectra with the stringent upper limits from neutrino telescopes like Super-Kamiokande, ANTARES, and IceCube (Fig. 9).
- Constraints on the Higgs portal:** The scalar S can couple to SM particles via a small mixing angle α with the SM Higgs boson. Since the spin-independent scattering cross section between dark matter and nucleons is highly sensitive to the scalar mediator mass (scaling roughly as α^2/m_S^4), direct detection experiments place strict joint constraints on the (m_S, α) parameter space. By exploring various experimental limits (Sec. IX), we find that the recent results from the LZ experiment (LZ 2025) currently impose the most stringent bounds, requiring a severely suppressed mixing angle α particularly for lighter scalar masses (Fig. 10).

- **Self-interactions and small-scale structure:** In the DM mass range of $10 \sim 75$ GeV, with the scalar mass m_S at the tens of MeV scale, the velocity-weighted transfer cross section $\langle \sigma_T v \rangle / m_-$ exhibits a profound dependence on the average collision velocity due to resonant enhancements (Figs. 11 and 12). This velocity-dependent self-interacting DM model elegantly explains the diversity of DM halos. At the scale of dwarf spheroidal and low surface brightness galaxies, the cross section reaches $\sigma_T / m_- \sim \mathcal{O}(1 - 10)$ cm²/g, resolving the core-cusp problem and explaining halo diversity. Simultaneously, the cross section is naturally suppressed at larger scales, comfortably satisfying the stringent upper limits for galaxy groups ($\lesssim 1.1$ cm²/g) and massive clusters ($\lesssim 0.35$ cm²/g) (Sec. X).

Acknowledgments. This work was partly supported by the National Center for Theoretical Sciences and the National Science and Technology Council of Taiwan under grant number NSTC 113-2112-M-033-005.

Appendix A: Derivation of the nearly degenerate Majorana eigenstates after SSB

After SSB, the mass term of the dark fermions is given by

$$\mathcal{L}_m = \mathcal{L}_m^D + \mathcal{L}_m^M, \quad (\text{A1})$$

where the Dirac mass part is

$$\begin{aligned} -\mathcal{L}_m^D &= \frac{m_D}{2} (\bar{\chi}\chi + \bar{\chi}^c\chi^c) \\ &= \frac{m_D}{2} (\bar{\chi}_R\chi_L + \bar{\chi}_L\chi_R + \bar{\chi}_R^c\chi_L^c + \bar{\chi}_L^c\chi_R^c), \end{aligned} \quad (\text{A2})$$

and the Majorana mass part with $fv_S \equiv m_M$ is

$$\begin{aligned} -\mathcal{L}_m^M &= \frac{m_M}{2} (\bar{\chi}^c\chi + \bar{\chi}\chi^c) = \frac{m_M}{2} (\bar{\chi}_R^c\chi_L + \bar{\chi}_L\chi_R^c) + \frac{m_M}{2} (\bar{\chi}_L^c\chi_R + \bar{\chi}_R\chi_L^c) \\ &= \frac{m_M}{2} (\bar{\chi}_L + \bar{\chi}_R^c) (\chi_L + \chi_R^c) + \frac{m_M}{2} (\bar{\chi}_R + \bar{\chi}_L^c) (\chi_R + \chi_L^c). \end{aligned} \quad (\text{A3})$$

In the absence of m_D , the dark fermion can be decomposed into two exactly degenerate Majorana states, $\chi_1 = \chi_L + \chi_R^c$ and $\chi_2 = \chi_R + \chi_L^c$, which can be defined up to an arbitrary rotation. In the

basis $\mathbf{X} = (\chi_1, \chi_2)^T$, the mass Lagrangian can be recast into a 4×4 matrix form:⁵

$$-\mathcal{L}_m = \underbrace{\begin{pmatrix} \overline{\chi_L} & \overline{\chi_R^c} & \overline{\chi_L^c} & \overline{\chi_R} \end{pmatrix}}_{\overline{\mathbf{X}}} \begin{pmatrix} 0 & 1 & 0 & 0 \\ 1 & 0 & 0 & 0 \\ 0 & 0 & 0 & 1 \\ 0 & 0 & 1 & 0 \end{pmatrix} \underbrace{\begin{pmatrix} m_M & 0 & m_D & 0 \\ 0 & m_M & 0 & m_D \\ m_D & 0 & m_M & 0 \\ 0 & m_D & 0 & m_M \end{pmatrix}}_{\mathbf{M}} \underbrace{\begin{pmatrix} \chi_L \\ \chi_R^c \\ \chi_L^c \\ \chi_R \end{pmatrix}}_{\mathbf{X}}. \quad (\text{A5})$$

We diagonalize the mass matrix \mathbf{M} by a unitary transformation, $\mathbf{U}_D \mathbf{M} \mathbf{U}_D^\dagger = \mathbf{D}$, where $\mathbf{D} = \text{diag}(m_M - m_D, m_M - m_D, m_M + m_D, m_M + m_D)$. The physical eigenstates can be read from

$$\mathbf{X}_D = \mathbf{U}_D \mathbf{X} = \frac{1}{\sqrt{2}} \begin{pmatrix} 0 & -1 & 0 & 1 \\ -1 & 0 & 1 & 0 \\ 0 & 1 & 0 & 1 \\ 1 & 0 & 1 & 0 \end{pmatrix} \begin{pmatrix} \chi_L \\ \chi_R^c \\ \chi_L^c \\ \chi_R \end{pmatrix} = \frac{1}{\sqrt{2}} \begin{pmatrix} \chi_R - \chi_R^c \\ -\chi_L + \chi_L^c \\ \chi_R + \chi_R^c \\ \chi_L + \chi_L^c \end{pmatrix}. \quad (\text{A6})$$

The first two elements of \mathbf{X}_D sum to χ_- , and the last two elements sum to χ_+ , given by

$$\chi_- = \frac{1}{\sqrt{2}}(-\chi_L + \chi_R - \chi_R^c + \chi_L^c) \quad \text{and} \quad \chi_+ = \frac{1}{\sqrt{2}}(\chi_L + \chi_R + \chi_R^c + \chi_L^c), \quad (\text{A7})$$

with masses $m_M - m_D$ and $m_M + m_D$, respectively.

Appendix B: Diagonalization of the gauge boson sector

Considering the possible kinetic mixings among the neutral gauge fields at low energy scale $\mu \lesssim m_\mu$, the neutral gauge boson sector of Lagrangian is given by

$$\begin{aligned} \mathcal{L}_{\text{gauge}} = & -\frac{1}{4} \hat{Z}_{\mu\nu} \hat{Z}^{\mu\nu} - \frac{1}{4} \hat{F}_{\mu\nu} \hat{F}^{\mu\nu} - \frac{1}{4} \hat{Z}'_{\mu\nu} \hat{Z}'^{\mu\nu} + \frac{1}{2} m_Z^2 \hat{Z}_\mu \hat{Z}^\mu + \frac{1}{2} m_{Z'}^2 \hat{Z}'_\mu \hat{Z}'^\mu \\ & - \frac{1}{2} \epsilon_A \hat{Z}'_{\mu\nu} \hat{F}^{\mu\nu} - \frac{1}{2} \epsilon_Z \hat{Z}'_{\mu\nu} \hat{Z}^{\mu\nu}, \end{aligned} \quad (\text{B1})$$

where hatted fields denote interaction eigenstates. To eliminate the kinetic mixing, we transform to a canonical basis $\tilde{\mathbf{V}}_\mu = (\tilde{Z}_\mu, \tilde{A}_\mu, \tilde{Z}'_\mu)^T$ via $\tilde{\mathbf{V}}_\mu = \zeta \hat{\mathbf{V}}_\mu$, where $\hat{\mathbf{V}}_\mu = (\hat{Z}_\mu, \hat{A}_\mu, \hat{Z}'_\mu)^T$, and

$$\zeta = \begin{pmatrix} 1 & 0 & \epsilon_Z \\ 0 & 1 & \epsilon_A \\ 0 & 0 & 1 - \frac{\epsilon_Z^2}{2} - \frac{\epsilon_A^2}{2} \end{pmatrix} + \mathcal{O}(\epsilon_{A,Z}^3). \quad (\text{B2})$$

⁵ Alternatively, we can write the mass Lagrangian as a 2×2 matrix,

$$-\mathcal{L}_m = \begin{pmatrix} \overline{\chi_R^c} & \overline{\chi_R} \end{pmatrix} \begin{pmatrix} m_M & m_D \\ m_D & m_M \end{pmatrix} \begin{pmatrix} \chi_L \\ \chi_L^c \end{pmatrix} + \text{h.c.}, \quad (\text{A4})$$

to find the Majorana mass eigenstates.

In terms of $\tilde{\mathbf{V}}_\mu$, the mass term in Eq. (18) can be written as $\mathcal{L}_{\text{gauge}}^{\text{mass}} = (1/2)\tilde{\mathbf{V}}_\mu^T(\zeta^{-1})^T\mathbf{M}\zeta^{-1}\tilde{\mathbf{V}}_\mu$, where $\mathbf{M} = \text{diag}(m_Z, 0, m_{Z'})$. We can then diagonalize the mass matrix to be $\xi^T((\zeta^{-1})^T\mathbf{M}\zeta^{-1})\xi = \mathbf{M}_{ph}$, where

$$\xi = \begin{pmatrix} 1 - \frac{\epsilon_Z^2 m_Z^4}{2(m_Z^2 - m_{Z'}^2)^2} & 0 & \frac{\epsilon_Z m_Z^2}{m_Z^2 - m_{Z'}^2} \\ 0 & 1 & 0 \\ -\frac{\epsilon_Z m_Z^2}{m_Z^2 - m_{Z'}^2} & 0 & 1 - \frac{\epsilon_Z^2 m_Z^4}{2(m_Z^2 - m_{Z'}^2)^2} \end{pmatrix} + \mathcal{O}(\epsilon_{A,Z}^3), \quad (\text{B3})$$

and diagonalized mass matrix is

$$\mathbf{M}_{ph} = \begin{pmatrix} m_Z^2 + \frac{\epsilon_Z^2 m_Z^4}{m_Z^2 - m_{Z'}^2} & 0 & 0 \\ 0 & 0 & 0 \\ 0 & 0 & m_{Z'}^2(1 + \epsilon_A^2) - \frac{\epsilon_Z^2 m_Z^4}{m_Z^2 - m_{Z'}^2} \end{pmatrix} + \mathcal{O}(\epsilon_{A,Z}^3). \quad (\text{B4})$$

Finally, the physical mass eigenstates relate to the original basis via $\mathbf{V}_\mu = (Z_\mu, A_\mu, Z'_\mu)^T = \mathbf{U}\hat{\mathbf{V}}_\mu$, with the transformation matrix given by

$$\mathbf{U} = \xi^{-1}\zeta = \begin{pmatrix} 1 - \frac{\epsilon_Z^2 m_Z^4}{2(m_Z^2 - m_{Z'}^2)^2} & 0 & -\frac{\epsilon_Z m_{Z'}^2}{m_Z^2 - m_{Z'}^2} \\ 0 & 1 & \epsilon_A \\ \frac{\epsilon_Z m_{Z'}^2}{m_Z^2 - m_{Z'}^2} & 0 & 1 - \frac{\epsilon_A^2}{2} - \frac{\epsilon_Z^2 m_{Z'}^4}{2(m_Z^2 - m_{Z'}^2)^2} \end{pmatrix} + \mathcal{O}(\epsilon_{A,Z}^3). \quad (\text{B5})$$

The interaction Lagrangian in Eq. (19) is written in terms of the interaction eigenstates $\hat{\mathbf{V}}_\mu$, which are related to the physical mass eigenstates V_μ by $\hat{\mathbf{V}}_\mu = \mathbf{U}^{-1}\mathbf{V}_\mu$. To the leading order in $\epsilon_{A,Z}$, the inverse matrix \mathbf{U}^{-1} is given by

$$\mathbf{U}^{-1} \simeq \begin{pmatrix} 1 & 0 & \frac{\epsilon_Z m_Z^2}{m_Z^2 - m_{Z'}^2} \\ 0 & 1 & -\epsilon_A \\ -\frac{\epsilon_Z m_{Z'}^2}{m_Z^2 - m_{Z'}^2} & 0 & 1 \end{pmatrix}. \quad (\text{B6})$$

Appendix C: Explicit formulas for the muon anomalous magnetic moment

From Eq. (22), the Lagrangian for the muon current coupling with the gauge bosons, relevant to the contributions to Δa_μ , is given by

$$\begin{aligned} \mathcal{L} \supset & - (g_{\mu\tau} + e\epsilon_A + \epsilon_Z r_{ZZ'} g_V g_Z) \bar{\mu} \gamma^\mu \mu Z'_\mu - \epsilon_Z r_{ZZ'} g_A g_Z \bar{\mu} \gamma^\mu \gamma_5 \mu Z'_\mu \\ & - (g_Z g_V - \epsilon_Z (1 + r_{ZZ'}) g_{\mu\tau}) \bar{\mu} \gamma^\mu \mu Z_\mu - g_Z g_A \bar{\mu} \gamma^\mu \gamma_5 \mu Z_\mu, \end{aligned} \quad (\text{C1})$$

where $g_V = -1/4 + \sin^2 \theta_W$, $g_A = 1/4$, and $r_{ZZ'} = m_{Z'}^2 / (m_Z^2 - m_{Z'}^2)$. Using the generic formulas for neutral vector bosons coupling to muons [55], the total contribution to the anomaly in this model is evaluated as

$$\begin{aligned} \Delta a_\mu = & \frac{(g_{\mu\tau} + e\epsilon_A + \epsilon_Z r_{ZZ'} g_V g_Z)^2}{4\pi^2} \frac{m_\mu^2}{m_{Z'}^2} I_V(m_{Z'}) + \frac{(\epsilon_Z r_{ZZ'} g_A g_Z)^2}{4\pi^2} \frac{m_\mu^2}{m_{Z'}^2} I_A(m_{Z'}) \\ & + \frac{(g_Z g_V - \epsilon_Z (1 + r_{ZZ'}) g_{\mu\tau})^2}{4\pi^2} \frac{m_\mu^2}{m_Z^2} I_V(m_Z) + \frac{(g_Z g_A)^2}{4\pi^2} \frac{m_\mu^2}{m_Z^2} I_A(m_Z), \end{aligned} \quad (\text{C2})$$

with

$$I_V(m_0) = \int_0^1 dx \frac{m_0^2 x^2 (1-x)}{m_0^2 (1-x) + m_\mu^2 x^2}, \quad (\text{C3})$$

$$I_A(m_0) = \int_0^1 dx \frac{m_0^2 x (1-x)(x-4) - 2x^3 m_\mu^2}{m_0^2 (1-x) + m_\mu^2 x^2}. \quad (\text{C4})$$

Using the relation $\epsilon_Z = -\epsilon_A \tan \theta_W$ and considering the limit $r_{ZZ'} \ll 1$ (i.e., $m_{Z'}^2 \ll m_Z^2$), the dominant contribution comes from the ϵ_A term while the ϵ_Z contribution is suppressed. This leads to the simplified expression as

$$\Delta a_\mu \simeq \frac{(g_{\mu\tau} + e\epsilon_A)^2}{4\pi^2} \int_0^1 dx \frac{m_\mu^2 x^2 (1-x)}{m_{Z'}^2 (1-x) + m_\mu^2 x^2}. \quad (\text{C5})$$

Appendix D: Decay widths

$$\Gamma_{S \rightarrow Z' Z'} = \frac{(g_\chi \cos \alpha)^2}{8\pi} \frac{m_S^3}{m_{Z'}^2} \left(1 - \frac{4m_{Z'}^2}{m_S^2}\right)^{1/2} \left(1 - \frac{4m_{Z'}^2}{m_S^2} + \frac{12m_{Z'}^4}{m_S^4}\right), \quad (\text{D1})$$

$$\Gamma_{Z' \rightarrow f \bar{f}} = \begin{cases} \frac{g_{\mu\tau}^2}{12\pi} m_{Z'} \left(1 + \frac{2m_f^2}{m_{Z'}^2}\right) \left(1 - \frac{4m_f^2}{m_{Z'}^2}\right)^{1/2} \theta(m_{Z'} - 2m_f), & \text{for } f = \mu \text{ or } \tau, \\ \frac{g_{\mu\tau}^2}{24\pi} m_{Z'}, & \text{for } f = \nu_\mu \text{ or } \nu_\tau, \end{cases} \quad (\text{D2})$$

$$\Gamma_{Z' \rightarrow e^+ e^-} = \frac{\alpha \epsilon_A^2 m_{Z'}}{3} \left(1 + \frac{2m_e^2}{m_{Z'}^2}\right) \left(1 - \frac{4m_e^2}{m_{Z'}^2}\right)^{1/2}, \quad (\text{D3})$$

$$\Gamma_{H \rightarrow \chi_\pm \chi_\pm} = \frac{f^2 \sin^2 \alpha}{16\pi m_H^2} (m_H^2 - 4m_\pm^2)^{3/2} \theta(m_H - 2m_\pm), \quad (\text{D4})$$

$$\Gamma_{H \rightarrow SS} = \frac{1}{128\pi m_H^2 v_S^2 v_H^2} (m_H^2 + 2m_S^2)^2 (m_H - 4m_S^2)^{1/2} (v_H \cos \alpha + v_S \sin \alpha)^2 \sin^2 2\alpha, \quad (\text{D5})$$

$$\Gamma_{H \rightarrow Z' Z'} = \frac{(g_\chi \sin \alpha)^2}{8\pi} \frac{m_H^3}{m_{Z'}^2} \left(1 - \frac{4m_{Z'}^2}{m_H^2}\right)^{1/2} \left(1 - \frac{4m_{Z'}^2}{m_H^2} + \frac{12m_{Z'}^4}{m_H^4}\right). \quad (\text{D6})$$

Appendix E: Cross sections relevant to the DM relic abundance

The thermally averaged annihilation cross section for the process $ij \rightarrow k\ell$ at temperature T is represented by [63]

$$\langle\sigma v\rangle_{ij\rightarrow k\ell} = \frac{g_i g_j T}{8\pi^4 n_i^{\text{eq}}(T) n_j^{\text{eq}}(T)} \int_{(m_i+m_j)^2}^{\infty} \sigma_{ij\rightarrow k\ell} p_{ij}^2 \sqrt{s} K_1\left(\frac{\sqrt{s}}{T}\right) ds, \quad (\text{E1})$$

where K_n is the modified Bessel function of the second kind, and the Mandelstam variable s is the square of the center-of-mass energy. The momentum of particle i (or j) in the center-of-mass frame is

$$p_{ij} = \frac{[s - (m_i + m_j)^2]^{1/2} [s - (m_i - m_j)^2]^{1/2}}{2\sqrt{s}}, \quad (\text{E2})$$

and the equilibrium number density of i at temperature T is given by

$$n_i^{\text{eq}}(T) = \frac{T}{2\pi^2} g_i m_i^2 K_2\left(\frac{m_i}{T}\right), \quad (\text{E3})$$

with g_i being its internal degrees of freedom.

Expanding the cross section in powers of the relative velocity v , $(\sigma v)_{ij\rightarrow k\ell} = a + bv^2 + cv^4 + \dots$, the thermal average in the $m_i \approx m_j$ limit yields [65]:

$$\langle\sigma v\rangle_{ij\rightarrow k\ell} = a + 6b \frac{T}{m_i} + (18b + 60c) \left(\frac{T}{m_i}\right)^2 + \dots. \quad (\text{E4})$$

1. $\chi_{\mp}\chi_{\mp} \rightarrow SS$

The cross section for $\chi_{\mp}\chi_{\mp} \rightarrow SS$, proceeding via t - and u -channel χ_{\pm} exchanges and the s -channel S contribution, is given by

$$\begin{aligned} \sigma_{\chi_{\mp}\chi_{\mp} \rightarrow SS} &= \frac{f^2 c_{\alpha}^2 \sqrt{s - 4m_S^2}}{32\pi s m_Z^2 \sqrt{s - 4m_{\mp}^2} (\Gamma_S^2 m_S^2 + (s - m_S^2)^2)} \\ &\times \left[- \frac{f^2 c_{\alpha}^2 m_Z^2 ((\Gamma_S^2 - 2s)m_S^2 + m_S^4 + s^2) (2m_{\mp}^2 (s - 8m_S^2) + 16m_{\mp}^4 + 3m_S^4)}{m_{\mp}^2 (s - 4m_S^2) + m_S^4} \right. \\ &+ \frac{f c_{\alpha} m_Z}{\sqrt{s - 4m_{\mp}^2} \sqrt{s - 4m_S^2} (s - 2m_S^2)} \left(\log \frac{s + \sqrt{s - 4m_{\mp}^2} \sqrt{s - 4m_S^2} - 2m_S^2}{s - \sqrt{s - 4m_{\mp}^2} \sqrt{s - 4m_S^2} - 2m_S^2} \right) \\ &\times \left(f c_{\alpha} m_Z (\Gamma_S^2 m_S^2 + (s - m_S^2)^2) (s^2 - 4m_S^2 (4m_{\mp}^2 + s) + 16sm_{\mp}^2 - 32m_{\mp}^4 + 6m_S^4) \right. \\ &\left. \left. - 12g_{\chi} c_{\alpha}^3 m_{\mp} m_S^2 (s^2 - 3sm_S^2 + 2m_S^4) (s - 8m_{\mp}^2 + 2m_S^2) \right) \right] \end{aligned}$$

$$\left. -24fg_\chi c_\alpha^4 m_\mp m_S^2 m_Z (s - m_S^2) + 18g_\chi^2 c_\alpha^6 m_S^4 (s - 4m_\mp^2) \right], \quad (\text{E5})$$

where $c_\alpha \equiv \cos \alpha$, and s is the Mandelstam invariant mass squared of two incident particles. Here, we have used the triple coupling to calculate the s -channel amplitude,

$$\mathcal{L} \supset \frac{1}{6} g_{SSS} SSS + \dots, \quad \text{with } g_{SSS} \simeq -\frac{6g_\chi c_\alpha^3 m_S^2}{m_{Z'}}. \quad (\text{E6})$$

Considering two annihilating particles in the non-relativistic limit, the cross section is approximated as

$$(\sigma v)_{\chi_\mp \chi_\mp \rightarrow SS} \simeq \frac{3f^4}{128\pi m_\mp^2} \left[v^2 - \frac{13}{15} v^4 + \mathcal{O}\left(\frac{m_S^2}{m_\mp^2}, v^6\right) \right]. \quad (\text{E7})$$

2. $\chi_\mp \chi_\mp \rightarrow Z' Z'$

The cross-section is given by

$$\begin{aligned} \sigma_{\chi_\mp \chi_\mp \rightarrow Z' Z'} &= \frac{g_\chi^2 \sqrt{s - 4m_{Z'}^2} (s - 2(m_\mp^2 - m_\pm^2 + m_{Z'}^2))^2}{32\pi m_{Z'}^4 ((s - m_S^2)^2 + \Gamma_S^2 m_S^2) s \sqrt{s - 4m_\mp^2} (2(m_\mp^2 - m_\pm^2 + m_{Z'}^2) - s)^3} \\ &\times \left\{ \frac{(s - 2(m_\mp^2 - m_\pm^2 + m_{Z'}^2))}{m_\mp^4 - 2(m_\pm^2 + m_{Z'}^2)m_\mp^2 + sm_\pm^2 + (m_\pm^2 - m_{Z'}^2)^2} \left[g_\chi^2 \Gamma_S^2 m_S^2 [3m_\mp^8 - 12m_\pm^2 m_\mp^6 + 6m_{Z'}^2 m_\mp^6 \right. \right. \\ &+ 28m_\pm m_{Z'}^2 m_\mp^5 + 18m_\pm^4 m_\mp^4 - 13m_{Z'}^4 m_\mp^4 - 6m_\pm^2 m_{Z'}^2 m_\mp^4 - 20m_\pm m_{Z'}^4 m_\mp^3 - 56m_\pm^3 m_{Z'}^2 m_\mp^3 \\ &- 12m_\pm^6 m_\mp^2 - 4m_{Z'}^6 m_\mp^2 + 2m_\pm^2 m_{Z'}^4 m_\mp^2 - 6m_\pm^4 m_{Z'}^2 m_\mp^2 - 8m_\pm m_{Z'}^6 m_\mp - 20m_\pm^3 m_{Z'}^4 m_\mp \\ &+ 28m_\pm^5 m_{Z'}^2 m_\mp + 3m_\pm^8 + 8m_\pm^8 - 4m_\pm^2 m_{Z'}^6 - 13m_\pm^4 m_{Z'}^4 - 2s^2 m_\pm^2 (m_\mp + m_\pm)^2 + 6m_\pm^6 m_{Z'}^2 \\ &- 2s((m_\mp^2 + 2m_\pm m_\mp - m_\pm^2)m_{Z'}^4 - 2(m_\mp + m_\pm)^2(m_\mp^2 + 3m_\pm^2)m_{Z'}^2 + m_\mp(m_\mp + 2m_\pm)(m_\mp^2 - m_\pm^2)^2] \\ &- g_\chi^2 (m_S^2 - s)^2 [-3m_\mp^8 + 12m_\pm^2 m_\mp^6 - 6m_{Z'}^2 m_\mp^6 - 28m_\pm m_{Z'}^2 m_\mp^5 - 18m_\pm^4 m_\mp^4 + 13m_{Z'}^4 m_\mp^4 \\ &+ 6m_\pm^2 m_{Z'}^2 m_\mp^4 + 20m_\pm m_{Z'}^4 m_\mp^3 + 56m_\pm^3 m_{Z'}^2 m_\mp^3 + 12m_\pm^6 m_\mp^2 + 4m_{Z'}^6 m_\mp^2 - 2m_\pm^2 m_{Z'}^4 m_\mp^2 \\ &+ 6m_\pm^4 m_{Z'}^2 m_\mp^2 + 8m_\pm m_{Z'}^6 m_\mp + 20m_\pm^3 m_{Z'}^4 m_\mp - 28m_\pm^5 m_{Z'}^2 m_\mp - 3m_\pm^8 - 8m_{Z'}^8 + 4m_\pm^2 m_{Z'}^6 \\ &+ 13m_\pm^4 m_{Z'}^4 + 2s^2 m_\pm^2 (m_\mp + m_\pm)^2 - 6m_\pm^6 m_{Z'}^2 + 2s((m_\mp^2 + 2m_\pm m_\mp - m_\pm^2)m_{Z'}^4 \\ &- 2(m_\mp + m_\pm)^2(m_\mp^2 + 3m_\pm^2)m_{Z'}^2 + m_\mp(m_\mp + 2m_\pm)(m_\mp^2 - m_\pm^2)^2] \\ &+ 4g_\chi f m_{Z'} (m_S^2 - s) (- (m_\mp + m_\pm) s^2 + 2(m_\mp + m_\pm)(m_\mp^2 - m_\pm m_\mp + m_{Z'}^2) s \\ &+ 4m_\mp m_{Z'}^2 (m_\mp^2 - m_\pm^2 - 2m_{Z'}^2)) (m_\mp^4 - 2(m_\pm^2 + m_{Z'}^2)m_\mp^2 + sm_\pm^2 + (m_\pm^2 - m_{Z'}^2)^2) \\ &+ 2f^2 (4m_\mp^2 - s) m_{Z'}^2 (12m_{Z'}^4 - 4sm_{Z'}^2 + s^2) (m_\mp^4 - 2(m_\pm^2 + m_{Z'}^2)m_\mp^2 + sm_\pm^2 + (m_\pm^2 - m_{Z'}^2)^2) \left. \right] \\ &- \frac{g_\chi}{\sqrt{s - 4m_\mp^2} \sqrt{s - 4m_{Z'}^2}} \left[\log \left(\frac{2m_\mp^2 - 2m_\pm^2 + 2m_{Z'}^2 - s - \sqrt{s - 4m_\mp^2} \sqrt{s - 4m_{Z'}^2}}{2m_\mp^2 - 2m_\pm^2 + 2m_{Z'}^2 - s + \sqrt{s - 4m_\mp^2} \sqrt{s - 4m_{Z'}^2}} \right) \right. \\ &\times \left[\Gamma_S^2 g_\chi [16m_{Z'}^8 - 8(5m_\mp^2 + 2m_\pm m_\mp + m_\pm^2)m_{Z'}^6 - 2(m_\mp - m_\pm)(5m_\mp^3 - 23m_\pm m_\mp^2 \right. \\ &- 33m_\pm^2 m_\mp - 13m_\pm^3)m_{Z'}^4 + 4(m_\mp^2 - m_\pm^2)^2(7m_\mp^2 + 14m_\pm m_\mp + 3m_\pm^2)m_{Z'}^2 + 6(m_\mp^2 - m_\pm^2)^4 \\ &+ s^2(4m_{Z'}^4 + 4(m_\mp + m_\pm)^2 m_{Z'}^2 + (m_\mp - 3m_\pm)(m_\mp + m_\pm)^3) - 4s(4m_\mp(m_\mp + 2m_\pm)m_{Z'}^4 \end{aligned}$$

with $\kappa_i \equiv m_i^2/m_{Z'}^2$. In the present study, $Z' \rightarrow \chi-\chi_+$ is kinetically blocked because $m_{Z'} < m_+ + m_-$. Considering two annihilating particles in the non-relativistic limit, the cross section is given by

$$\begin{aligned} (\sigma v)_{\chi-\chi_+ \rightarrow \ell\bar{\ell}} &= \frac{g_{\mu\tau}^2 g_\chi^2}{96\pi m_-^2} v^2 \left[1 + \frac{\delta m}{m_-} + \mathcal{O}\left(\frac{\delta m^2}{m_-^2}, \frac{m_{Z'}^2}{m_-^2}, \frac{m_\ell^2}{m_-^2}\right) \right], \\ (\sigma v)_{\chi-\chi_+ \rightarrow \nu_e \bar{\nu}_e} &= \frac{g_{\mu\tau}^2 g_\chi^2}{192\pi m_-^2} v^2 \left[1 + \frac{\delta m}{m_-} + \mathcal{O}\left(\frac{\delta m^2}{m_-^2}, \frac{m_{Z'}^2}{m_-^2}\right) \right], \end{aligned} \quad (\text{E12})$$

where $m_+ = m_- + \delta m$.

4. $\chi-\chi_+ \rightarrow Z'S$

The cross-section is given by

$$\begin{aligned} \sigma_{\chi-\chi_+ \rightarrow Z'S} &= \frac{c_\alpha^2 f^2 g_\chi^2 \sqrt{s - (m_S - m_{Z'})^2} \sqrt{s - (m_S + m_{Z'})^2}}{16\pi s^{3/2} (s - 4m_-^2)^{3/2} m_{Z'}^2} \\ &\left\{ 4\sqrt{s} \coth^{-1} \left(\frac{\sqrt{s}(s - m_S^2 - m_{Z'}^2)}{\sqrt{s - 4m_-^2} \sqrt{s - (m_S - m_{Z'})^2} \sqrt{s - (m_S + m_{Z'})^2}} \right) \right. \\ &\times \left[4m_-(\delta m - m_-)m_{Z'}^6 + 40m_-^4 m_{Z'}^4 + 128m_-^5 (m_- + \delta m)m_{Z'}^2 + s(m_{Z'}^4 - 2m_-(m_- + 9\delta m)m_{Z'}^2) \right. \\ &- 16m_-^3 (7m_- + 4\delta m)m_{Z'}^2 + s^3(m_{Z'}^2 - 2m_-(m_- + \delta m)) + 2s^2(4m_-^4 + 4(2m_- + 3\delta m)m_{Z'}^2 m_- - m_{Z'}^4) \\ &+ m_S^4(8m_-^4 - 2(2m_{Z'}^2 + s)m_-^2 + \delta m(4m_{Z'}^2 - 2s)m_- + sm_{Z'}^2) + 4m_S^2(m_{Z'}^2 - s)[s(m_{Z'}^2 - m_-(m_- + \delta m)) \\ &+ 4m_-(m_-^3 - m_{Z'}^2 m_- + \delta m m_{Z'}^2)] \left. \right] \frac{1}{\sqrt{s - 4m_-^2} \sqrt{s - (m_S - m_{Z'})^2} (s - m_S^2 - m_{Z'}^2) \sqrt{s - (m_S + m_{Z'})^2}} \\ &+ 2 \left[(4m_-^2 - s)[m_-^2 m_S^4 + (sm_{Z'}^2 - 2m_-^2(m_{Z'}^2 + s))m_S^2 + m_-^2(m_{Z'}^2 - s)^2] [m_-^2(2m_{Z'}^2 - s)m_S^4 \right. \\ &- ((4m_{Z'}^4 + 6sm_{Z'}^2 - 2s^2)m_-^2 + sm_{Z'}^2(s - 3m_{Z'}^2))m_S^2 + m_-^2(2m_{Z'}^6 - 9sm_{Z'}^4 + 4s(4m_-^2 + s)m_{Z'}^2 - s^3)] \\ &+ m_- \left[(4(s - m_{Z'}^2)m_-^4 - sm_{Z'}^2 m_-^2)m_S^8 + 4m_-^2(4(m_{Z'}^4 + sm_{Z'}^2 - s^2)m_-^2 + sm_{Z'}^2(3s - 4m_{Z'}^2))m_S^6 \right. \\ &+ 2m_S^4(32sm_{Z'}^2 m_-^6 - 4(3m_{Z'}^6 + sm_{Z'}^4 + 9s^2 m_{Z'}^2 - 3s^3)m_-^4 + sm_{Z'}^2(17m_{Z'}^4 + 10sm_{Z'}^2 - 11s^2)m_-^2 \\ &- 6s^2 m_{Z'}^6 + 4s^3 m_{Z'}^4) - 4m_S^2 m_-^6(32sm_{Z'}^2(m_{Z'}^2 + s) - 4m_-^4(m_{Z'}^8 - 3sm_{Z'}^6 + 8s^2 m_{Z'}^4 + 7s^3 m_{Z'}^2 - s^4) \\ &+ sm_{Z'}^2(4m_{Z'}^6 - 11sm_{Z'}^4 + 22s^2 m_{Z'}^2 - 3s^3)m_-^2 - s^3 m_{Z'}^6) \\ &+ m_-^2(m_{Z'}^2 - s)^2(64sm_{Z'}^2 m_-^4 + 4(s^3 - 11s^2 m_{Z'}^2 + 7sm_{Z'}^4 - m_{Z'}^6)m_-^2 - s(m_{Z'}^3 - sm_{Z'}^2)^2) \left. \right] \\ &\times \frac{1}{(m_-^2 m_S^4 + (sm_{Z'}^2 - 2m_-^2(m_{Z'}^2 + s))m_S^2 + m_-^2(s - m_{Z'}^2)^2)^2} \left. \right\} + \mathcal{O}((\delta m)^2), \end{aligned} \quad (\text{E13})$$

which is expanded by using $m_+ = m_- + \delta m$. Taking into account two annihilating particles in the non-relativistic limit, the cross section is approximated as

$$(\sigma v)_{\chi-\chi_+ \rightarrow Z'S} \simeq \frac{\delta m^2 c_\alpha^2 g_\chi^2 f^2}{32\pi m_-^4} + v^2 \frac{c_\alpha^2 g_\chi^2 f^2}{24\pi m_{Z'}^2} \left[1 + \mathcal{O}\left(\frac{\delta m^2}{m_-^2}, \frac{m_{Z'}^2}{m_-^2}, \frac{m_S^2}{m_-^2}\right) \right] + \mathcal{O}(\delta m^4, v^4), \quad (\text{E14})$$

which is p -wave dominant for $\delta m \ll m_-$.

Appendix F: Kinetic decoupling of χ_{\pm} and S

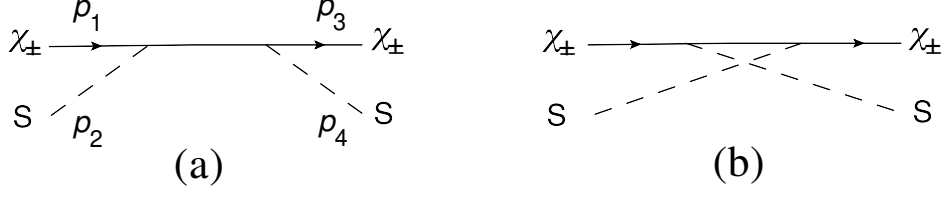


FIG. 13. Feynman diagrams for the $\chi_{\pm} S \rightarrow \chi_{\pm} S$ elastic scattering process, where the corresponding momenta p_i with $i = 1, 2, 3, 4$ are shown.

Even after dark matter freezes out, both S and Z' particles remain in thermal equilibrium with the SM bath through the interactions $S \leftrightarrow Z'Z'$ and $Z' \leftrightarrow \nu_{\mu}\bar{\nu}_{\mu}, \nu_{\tau}\bar{\nu}_{\tau}$. As illustrated in Fig. 4, the interaction $Z' \leftrightarrow e^+e^-$ facilitates the thermal connection between the (γ, e^{\pm}) and $(\nu_{\mu}, \nu_{\tau}, S, Z')$ baths, ensuring that $T = T_{\nu_{\mu}}$ is maintained until the temperature roughly drops below m_e . As the temperature drops, the S particles, which are exponentially suppressed by Boltzmann factors with a vanishing chemical potential, follow the temperature $T_{\nu_{\mu}}$.

Even after chemical freeze-out, dark matter remains in kinetic equilibrium with the SM bath via $\chi_{\pm}S \leftrightarrow \chi_{\pm}S$ elastic scattering. This occurs because the $\chi_{\mp}S \rightarrow \chi_{\mp}S$ elastic scattering rate is proportional to the number density of S , which remains highly relativistic and is not Boltzmann suppressed once the temperature drops below T_f , compared to the process $\chi_{\mp}\chi_{\mp} \rightarrow SS$. We will show that χ_{\pm} with masses ranging from a few GeV to hundreds of GeV decouple from S at temperatures between 210 and 250 MeV. Basically, when studying the kinetic decoupling of χ_{\pm} from S , the S particles can be viewed as part of the thermal bath, sharing the same temperature as the photons.

Fig. 13 depicts the diagrams for elastic scattering $\chi_{\pm} S \rightarrow \chi_{\pm} S$, which are relevant for the kinetic energy transfer between χ_{\pm} and S . The u -channel diagram (on the right) is derived from the s -channel diagram (on the left) through crossing symmetry. For nonrelativistic dark matter, its temperature evolution follows the equation

$$\frac{dT_{\text{DM}}}{dt} + 2HT_{\text{DM}} = -\frac{1}{n} \sum_{i=+,-} 2n_i \gamma_i (T_{\text{DM}} - T) + \dots, \quad (\text{F1})$$

where $n = n_+ + n_-$, and $2\gamma_{\pm}$ is the average rate of kinetic energy transfer from S to χ_{\pm} at temperature T .

The γ_i values can be obtained by reformulating the thermally averaged collision term for elastic

scattering $\chi_{\pm}S \rightarrow \chi_{\pm}S$ using a semi-relativistic Fokker-Planck-like equation [126], expressed as

$$\begin{aligned} \gamma_i &= \frac{1}{6m_i T n_i} \int \prod_{\substack{j=1,2 \\ k=3,4}} d\Pi_j d\Pi_k f_j(T_j) (2\pi)^4 \delta^{(4)}(p_1 + p_2 - p_3 - p_4) |M|_{\chi_{\pm}S \rightarrow \chi_{\pm}S}^2 (-1)^{(p_1 - p_4)^2} \\ &\simeq \frac{1}{6\pi^2 g_i m_i^2 T K_2(m_i/T_{\text{DM}})} \int_{(m_i+m_S)^2}^{\infty} ds \frac{(s - (m_i + m_S)^2)(s - (m_i - m_S)^2)}{4\sqrt{s}} K_1\left(\frac{\sqrt{s}}{T}\right) \\ &\quad \times \int \frac{d\sigma}{d\Omega} m_{\pm} v_{\pm}^2 (1 - \cos\theta) d\Omega, \end{aligned} \quad (\text{F2})$$

with $\gamma_+ \simeq \gamma_-$ and the distributions approximated by

$$f_i = e^{-(E_i - \mu_i)/T_i} (1 \pm f_i) \simeq e^{-(E_i - \mu_i)/T_i} = \frac{n_i}{n_i^{\text{eq}}(T_i)} e^{-E_i/T_i}, \quad (\text{F3})$$

where $n_S = n_S^{\text{eq}}(T)$, $T_S = T$, and $T_+ = T_- \equiv T_{\text{DM}}$.

The squared amplitude, $|M|_{\chi_{\pm}S \rightarrow \chi_{\pm}S}^2$, is summed over initial and final internal degrees of freedom, and

$$\begin{aligned} \int \frac{d\sigma}{d\Omega} m_{\pm} v_{\pm}^2 (1 - \cos\theta) d\Omega &= \frac{f^4}{48\pi(s - m_{\pm}^2)^2} \left[\frac{1}{s^3(m_{\pm}^2 s - (m_{\pm}^2 - m_S^2)^2)} \right. \\ &\quad \left(-2m_{\pm}^2(m_S^2 - m_{\pm}^2)^6 + s^5(5m_S^4 - 62m_S^2 m_{\pm}^2 + 231m_{\pm}^4) \right. \\ &\quad - s(m_S^4 - 22m_S^2 m_{\pm}^2 - 3m_{\pm}^4)(m_S^2 - m_{\pm}^2)^4 + 4s^4(4m_S^6 - 45m_S^4 m_{\pm}^2 + 47m_S^2 m_{\pm}^4 - 102m_{\pm}^6) \\ &\quad + 2m_{\pm}^2 s^3(96m_S^6 - 109m_S^4 m_{\pm}^2 + 18m_S^2 m_{\pm}^4 + 59m_{\pm}^6) \\ &\quad + s^2(4m_S^6 - 87m_S^4 m_{\pm}^2 - 70m_S^2 m_{\pm}^4 + 57m_{\pm}^6)(m_S^2 - m_{\pm}^2)^2 + m_{\pm}^2 s^6 \left. \right) \\ &\quad + \frac{6(s - m_{\pm}^2)}{m_S^4 - 2m_S^2(s + m_{\pm}^2) + (s - m_{\pm}^2)^2} \left(-4m_S^6 + m_S^4(s - 33m_{\pm}^2) + m_S^2(6m_{\pm}^4 + 60m_{\pm}^2 s - 2s^2) \right. \\ &\quad \left. + 31m_{\pm}^6 - 13m_{\pm}^4 s - 19m_{\pm}^2 s^2 + s^3 \right) \log \frac{s(s - 2m_S^2 - m_{\pm}^2)}{m_{\pm}^2 s - (m_{\pm}^2 - m_S^2)^2} \left. \right], \end{aligned} \quad (\text{F4})$$

which is Lorentz invariant even though the right-hand side is expressed in the center-of-mass frame with θ and v_{\pm} representing the scattering angle and velocity of χ_{\pm} , respectively. In Fig. 14, we show the kinetic energy injection rate from the thermal bath into dark matter via elastic scattering $\chi_{\pm}S \leftrightarrow \chi_{\pm}S$, compared to the cosmic cooling rate caused by Hubble expansion. Dark matter becomes kinetically decoupled from the thermal bath when $\gamma(\equiv \gamma_{\pm}) < H$. We find that χ_{\pm} with a mass of several GeV to hundreds of GeV kinetically decouples from S at a temperature roughly between 210 and 250 MeV. Meanwhile, this decoupling temperature is insensitive to m_S , which ranges from several MeV to hundreds of MeV.

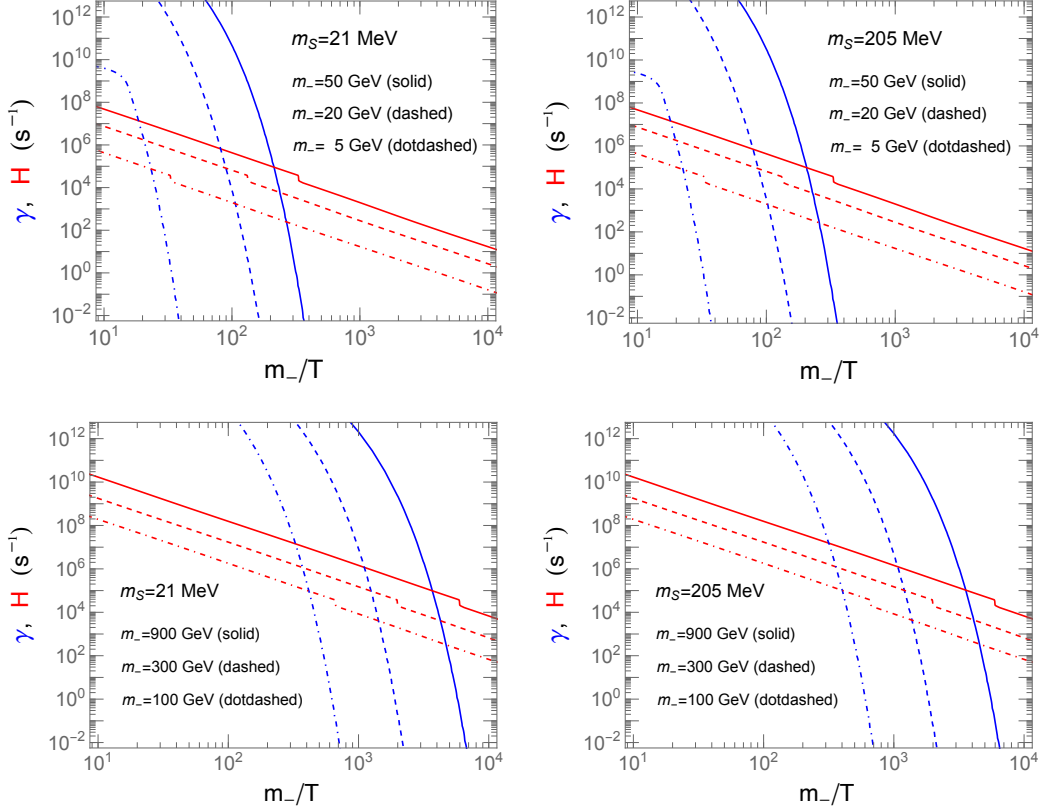


FIG. 14. Comparison of kinetic energy injection rates (blue), $\gamma \equiv \gamma_{\pm}$, from the thermal bath to dark matter via elastic scattering, $\chi_{\pm} S \rightarrow \chi_{\pm} S$, and the cooling rate due to Hubble expansion (red), H . Results are shown for different values of m_{-} , with m_S fixed at 21 MeV on the left and 205 MeV on the right. When $\gamma < H$, dark matter is kinetically decoupled from the thermal bath. All the decoupling temperatures are roughly between 210 and 250 MeV.

Appendix G: Constraints from neutrino telescopes on the neutrino excess caused by dark matter annihilations

The $\chi_{-}\chi_{-}$ pair can annihilate into SS or $Z'Z'$, which subsequently undergo cascade decays into muon or tau neutrinos. In this analysis, we restrict our focus to the kinematic regime $2m_{Z'} < m_S < m_{\mu}$. The differential neutrino flux, arising from DM annihilation, can be expressed as

$$\frac{d\Phi_{\nu}}{dE} \simeq \frac{1}{8\pi m_{-}^2} \left[\sum_{i=S,Z'} \langle \sigma v \rangle_{ii} \left(\frac{dN_{\nu}}{dE} \right)_{ii} \right] \underbrace{\frac{1}{\Delta\Omega} \int_{\Delta\Omega} \int_{\text{l.o.s.}} ds \rho^2(r(s, \psi)) d\Omega}_{\text{J-factor}}, \quad (\text{G1})$$

where $\langle \sigma v \rangle_{ii} \equiv \langle \sigma v \rangle_{\chi_{\mp}\chi_{\mp} \rightarrow ii}$. We have $\langle \sigma v \rangle_{SS} \simeq 9\langle \sigma v \rangle_{Z'Z'}$ in the present model. The J-factor is calculated by integrating the DM density squared along the line of sight (l.o.s.) and over the solid

angle $\Delta\Omega$ that covers the source region. The term $(dN_\nu/dE)_{ii}$ represents the neutrino spectrum per DM annihilation.

We use the original Navarro-Frenk-White (NFW) profile with $\gamma = 1$ [127, 128],

$$\rho(r) = \rho_\odot \left(\frac{r}{r_\odot}\right)^{-\gamma} \left(\frac{1+r/r_s}{1+r_\odot/r_s}\right)^{\gamma-3}, \quad (\text{G2})$$

to describe the DM density distribution in the Galactic halo, where $r_s = 20$ kpc is the scale radius, r is the distance to the GC. We take the DM density $\rho_\odot = 0.35$ GeV in the location of the Sun $r_\odot = 8.5$ kpc in the analysis. The variation of γ can change the inner slope of the profile.

For the DM annihilation process $\chi_-\chi_- \rightarrow SS$, the differential muon-neutrino flux arises from a two-step annihilation process [129–132]. Initially, two DM particles annihilate into a pair of scalar mediators. Each scalar then decays into two Z' particles, with each Z' decay resulting in two neutrinos. Since the neutrinos produced in DM annihilation go through intermediate steps, the spectrum from Z' decays is boosted and becomes broader,

$$\left(\frac{dN_\nu}{dE}\right)_{SS} = \frac{16/5}{m_- \sqrt{1-\epsilon_2^2} \sqrt{1-\epsilon_1^2}} \int_{t_{2,\min}}^{t_{2,\max}} \frac{dx_1}{x_1}, \quad (\text{G3})$$

where

$$\epsilon_2 = \frac{m_S}{m_-}, \quad \epsilon_1 = \frac{2m_{Z'}}{m_S}, \quad (\text{G4})$$

$$t_{2,\max} = \min\left[\frac{1}{2}\left(1 + \sqrt{1-\epsilon_1^2}\right), \frac{2E}{\epsilon_2^2 m_-}\left(1 + \sqrt{1-\epsilon_2^2}\right)\right], \quad t_{2,\min} = \frac{2E}{\epsilon_2^2 m_-}\left(1 - \sqrt{1-\epsilon_2^2}\right), \quad (\text{G5})$$

$$0 \leq E \leq \frac{m_-}{4}\left(1 + \sqrt{1-\epsilon_1^2}\right)\left(1 + \sqrt{1-\epsilon_2^2}\right), \quad x_1 = \frac{2E_1}{m_S}, \quad (\text{G6})$$

with E , and E_1 as the neutrino energies in the center-of-mass frame of the DM pair and the S rest frame, respectively. The factor 16/5 accounts for two distinct effects. First, a single DM annihilation eventually produces eight neutrinos. Second, taking into account neutrino oscillations during propagation, the expected flavor ratio at Earth is approximately 1 : 2 : 2 in the $L_\mu - L_\tau$ model [133, 134].

For $\chi_-\chi_- \rightarrow Z'Z'$, the differential muon-neutrino flux arises from a one-step annihilation process [129–132]. The two DM particles annihilate into a pair of the Z' gauge bosons, and then each Z' decays into two neutrinos, resulting in

$$\left(\frac{dN_\nu}{dE}\right)_{Z'Z'} = 2 \int_{t_{\min}}^{t_{\max}} \frac{dx_0}{x_0 \sqrt{1-\epsilon^2}} \frac{dN_\nu^{Z'}}{dx_0} = \frac{8}{5\sqrt{1-\epsilon^2}}, \quad (\text{G7})$$

where

$$\epsilon = \frac{m_{Z'}}{m_-}, \quad t_{\max} = \min\left[1, \frac{2E}{m_- \epsilon^2}\left(1 + \sqrt{1-\epsilon^2}\right)\right], \quad t_{\min} = \frac{2E}{m_- \epsilon^2}\left(1 - \sqrt{1-\epsilon^2}\right), \quad (\text{G8})$$

$$0 \leq E \leq \frac{m_-}{2} \left(1 + \sqrt{1 - \epsilon^2}\right), \quad x_0 = \frac{2E_0}{m_{Z'}}, \quad (\text{G9})$$

with E_0 being the neutrino energy in the Z' rest frame. Here, the muon neutrino spectrum of a Z' decay into two neutrinos in the $L_\mu - L_\tau$ model is given by $dN_\nu^{Z'}/dx_0 = 2 \times \frac{2}{5} \delta(x_0 - 1)$, where the factor 2 accounts for two neutrinos are produced per decay, while the factor $2/5$ is the flux ratio resulting from oscillation observed on the Earth [134].

The upper limit on $\langle \sigma v \rangle = \langle \sigma v \rangle_{SS} + \langle \sigma v \rangle_{Z'Z'}$ can be derived from the relation,

$$\mu^{90\%} = T_{\text{live}} \Delta\Omega \int dE A_{\text{eff}}(E) \frac{d\Phi_\nu}{dE}, \quad (\text{G10})$$

where $\mu^{90\%}$ is the 90% C.L. upper limit on the expect signal from DM annihilations, $\Delta\Omega$ denotes the solid angle of the search region, A_{eff} is the effective area, and T_{live} represents the live time.

Using these inputs, we derive the upper bounds on $\langle \sigma v \rangle$ from various experiments as follows.

Super-Kamiokande

The upper limit for muon-neutrino excess is determined using the on-off source approach of Super-Kamiokande (SK) [73, 74], based on analyses of SK-I, II, III, and IV data [75]. The maximum neutrino excess is expected in the on-source region, centered around the Galactic center, while the off-source region of the same size is located 180° away in right ascension of equatorial coordinates. Therefore, the difference in neutrino event counts (ΔN^{sig}) between these regions directly indicates DM annihilation signals.

The 90% C.L. upper limit for $\Delta N_{90}^{\text{sig}} (\equiv \mu^{90\%})$ is provided separately for μ -like event samples categorized as FC SubGeV, FC MultiGeV, PC, and UP- μ [74], which correspond to the measured neutrino energy ranges of approximately 0.1 – 1 GeV, 1 – 5 GeV, 5 – 50 GeV, and greater than 50 GeV, respectively [75]. For the SK, the live time is given by

$$T_{\text{live}} = \frac{N_{\text{atm}}}{\int dE A_{\text{eff}}(E) \frac{d\Phi_{\text{atm}}}{dE} \Delta\Omega}, \quad (\text{G11})$$

where $\Delta\Omega = 2\pi(1 - \cos\Psi)$ denotes the solid angle of the on-source region for each event sample, N_{atm} is the number of atmospheric muon neutrinos in the off-source region for each sample (see Table 8.2 of Ref. [74]), which are mainly background events, and the corresponding flux is $d\Phi_{\text{atm}}/dE$ (shown in Fig. 7 of Ref. [75]).

The effective area depends on the fiducial volume of the water Cherenkov detector and the scattering cross section. The latter is roughly proportional to the incident neutrino energy [135]. Assuming the effective area scales as $\sim E^\beta$, then $\beta=0$ to 1 has little effect on the upper limit of $\langle \sigma v \rangle$. This variation is only slightly noticeable at higher m_- . When $\beta = 0$, the limit at $m_- = 300$ GeV

is 1.3 times weaker than with $\beta = 1$, but at $m_- = 1000$ GeV, it is 2.7 times weaker. Here, we use $\beta = 1$.

The data show neutrinos from dark matter in the Milky Way are not significantly above atmospheric background. Using the 90% C.L. upper limit for $\Delta N_{90}^{\text{sig}}$, derived from μ -like event samples in Ref. [74], we establish an upper bound on the dark matter self-annihilation cross section, applicable to the typical velocity range of 140–280 km/s near the Galactic center.

ANTARES

In the indirect detection of dark matter, ANTARES [76, 77] did not observe a signal significantly higher than the background from data collected between 2007 and 2012 (total effective time of approximately $T_{\text{live}} = 1321$ days), thus deriving upper limits for neutrino flux and velocity-averaged annihilation cross sections.

ANTARES adopts two reconstruction algorithms, Λ Fit and QFit, to analyze the data, where $\mu^{90\%}$ that we used is the 90% C.L. upper limit on the $\nu_\mu + \bar{\nu}_\mu$ flux at Earth. We find that Λ Fit provides a stronger constraint than QFit in the region of dark matter masses greater than 250 GeV. Therefore, only the results for Λ Fit are shown in the Fig. 9. The $\mu^{90\%}$ of the Λ Fit and the angular separation (Ψ) of the solid angle can be obtained from Table 3 of Ref. [76], while the effective area can be obtained from its Fig. 1.

IceCube

Using $T_{\text{live}} = 9.28$ years of data (from May 2011 to May 2021), IceCube [78] has significantly improved the detection sensitivity of neutrinos in the low-energy region (10 GeV - 1000 GeV). The accumulation of data has made it possible to more accurately remove the atmospheric neutrino background. In the analysis, we take an opening angle $\Psi \sim 100^\circ$. As illustrated in Fig. 6 of Ref. [78], the signal contribution becomes negligible beyond $\Psi \sim 100^\circ$. Since the annihilation flux scales with the squared density ($\rho^2 \propto r^{-2 \sim -4}$), the signal drops rapidly with distance from the Galactic Center, making the contribution to the J-factor from the region $\Psi \gtrsim 100^\circ$ insignificant.

We approximate the 90% C.L. upper limit $\mu^{90\%} = \hat{n}_s(1 + 1.282/z\text{-score})$ for the $\nu_\mu\bar{\nu}_\mu$ channel using the reported best-fit signal events \hat{n}_s and the corresponding z-score given in Table VI of Ref. [78]. To characterize the detector response, we derive the effective area (A_{eff}) by directly inverting the reported 90% C.L. upper limits.

[1] D. Tucker-Smith and N. Weiner, “Inelastic dark matter,” Phys. Rev. D **64**, 043502 (2001) [arXiv:hep-ph/0101138 [hep-ph]].

- [2] D. Tucker-Smith and N. Weiner, “The Status of inelastic dark matter,” *Phys. Rev. D* **72**, 063509 (2005) [arXiv:hep-ph/0402065 [hep-ph]].
- [3] B. Batell, M. Pospelov and A. Ritz, “Direct Detection of Multi-component Secluded WIMPs,” *Phys. Rev. D* **79**, 115019 (2009) [arXiv:0903.3396 [hep-ph]].
- [4] S. Chang, N. Weiner and I. Yavin, “Magnetic Inelastic Dark Matter,” *Phys. Rev. D* **82**, 125011 (2010) [arXiv:1007.4200 [hep-ph]].
- [5] N. Okada and O. Seto, “Inelastic extra $U(1)$ charged scalar dark matter,” *Phys. Rev. D* **101**, no.2, 023522 (2020) [arXiv:1908.09277 [hep-ph]].
- [6] G. Dalla Valle Garcia, “A minimalistic model for inelastic dark matter,” *Phys. Lett. B* **862**, 139320 (2025) [arXiv:2411.02147 [hep-ph]].
- [7] X. G. Wang and A. W. Thomas, “A Viable New Model for Dark Matter,” [arXiv:2510.24114 [hep-ph]].
- [8] N. Arkani-Hamed, D. P. Finkbeiner, T. R. Slatyer and N. Weiner, “A Theory of Dark Matter,” *Phys. Rev. D* **79**, 015014 (2009) [arXiv:0810.0713 [hep-ph]].
- [9] M. Pospelov and A. Ritz, “Astrophysical Signatures of Secluded Dark Matter,” *Phys. Lett. B* **671**, 391-397 (2009) [arXiv:0810.1502 [hep-ph]].
- [10] D. P. Finkbeiner, T. R. Slatyer, N. Weiner and I. Yavin, “PAMELA, DAMA, INTEGRAL and Signatures of Metastable Excited WIMPs,” *JCAP* **09**, 037 (2009) [arXiv:0903.1037 [hep-ph]].
- [11] R. A. Gustafson, G. Herrera, M. Mukhopadhyay, K. Murase and I. M. Shoemaker, “Cosmic-ray cooling in active galactic nuclei as a new probe of inelastic dark matter,” *Phys. Rev. D* **111**, no.12, L121303 (2025) [arXiv:2408.08947 [hep-ph]].
- [12] A. Berlin, J. W. Foster, D. Hooper and G. Krnjaic, “dSphobic Dark Matter,” [arXiv:2504.12372 [hep-ph]].
- [13] D. Hooper, G. Krnjaic, D. Rocha and S. Roy, “Gamma-Rays and Gravitational Waves from Inelastic Higgs Portal Dark Matter,” [arXiv:2507.22975 [hep-ph]].
- [14] A. Berlin, G. Krnjaic and E. Pinetti, “Reviving MeV-GeV indirect detection with inelastic dark matter,” *Phys. Rev. D* **110**, no.3, 035015 (2024) [arXiv:2311.00032 [hep-ph]].
- [15] G. Krnjaic, D. McKeen, R. Mizuta, G. Mohlabeng, D. E. Morrissey and D. Tucker, “X-rays from Inelastic Dark Matter Freeze-in,” [arXiv:2509.19428 [hep-ph]].
- [16] E. Izaguirre, G. Krnjaic and B. Shuve, “Discovering Inelastic Thermal-Relic Dark Matter at Colliders,” *Phys. Rev. D* **93**, no.6, 063523 (2016) [arXiv:1508.03050 [hep-ph]].
- [17] A. Berlin and F. Kling, “Inelastic Dark Matter at the LHC Lifetime Frontier: ATLAS, CMS, LHCb, CODEX-b, FASER, and MATHUSLA,” *Phys. Rev. D* **99**, no.1, 015021 (2019) [arXiv:1810.01879 [hep-ph]].
- [18] I. V. Voronchikhin and D. V. Kirpichnikov, “Examining scalar portal inelastic dark matter with lepton fixed target experiments,” [arXiv:2505.04290 [hep-ph]].
- [19] G. Krnjaic, D. Rocha and I. R. Wang, “Discovering Dark Matter with the MUonE Experiment,”

- Phys. Rev. Lett. **134**, no.16, 161801 (2025) [arXiv:2409.00170 [hep-ph]].
- [20] G. D. V. Garcia, F. Kahlhoefer, M. Ovchinnikov and T. Schwetz, “Not-so-inelastic Dark Matter,” JHEP **02**, 127 (2025) [arXiv:2405.08081 [hep-ph]].
- [21] A. M. Abdullahi, M. Hostert, D. Massaro and S. Pascoli, “Semi-Visible Dark Photon Phenomenology at the GeV Scale,” Phys. Rev. D **108**, no.1, 015032 (2023) [arXiv:2302.05410 [hep-ph]].
- [22] M. Carrillo González and N. Toro, “Cosmology and signals of light pseudo-Dirac dark matter,” JHEP **04**, 060 (2022) [arXiv:2108.13422 [hep-ph]].
- [23] S. Heeba, T. Lin and K. Schutz, “Inelastic freeze-in,” Phys. Rev. D **108**, no.9, 095016 (2023) [arXiv:2304.06072 [hep-ph]].
- [24] N. Brahma, S. Heeba and K. Schutz, “Resonant pseudo-Dirac dark matter as a sub-GeV thermal target,” Phys. Rev. D **109**, no.3, 035006 (2024) [arXiv:2308.01960 [hep-ph]].
- [25] S. Roy, “Dark Matter and Electroweak Baryogenesis with Spontaneous CP Violation in the Early Universe,” [arXiv:2509.19982 [hep-ph]].
- [26] S. Tulin and H. B. Yu, “Dark Matter Self-interactions and Small Scale Structure,” Phys. Rept. **730**, 1-57 (2018) [arXiv:1705.02358 [hep-ph]].
- [27] S. Adhikari, A. Banerjee, K. K. Boddy, F. Y. Cyr-Racine, H. Desmond, C. Dvorkin, B. Jain, F. Kahlhoefer, M. Kaplinghat and A. Nierenberg, *et al.* “Astrophysical tests of dark matter self-interactions,” Rev. Mod. Phys. **97**, no.4, 045004 (2025) [arXiv:2207.10638 [astro-ph.CO]].
- [28] M. Kaplinghat, S. Tulin and H. B. Yu, “Dark Matter Halos as Particle Colliders: Unified Solution to Small-Scale Structure Puzzles from Dwarfs to Clusters,” Phys. Rev. Lett. **116**, no.4, 041302 (2016) [arXiv:1508.03339 [astro-ph.CO]].
- [29] X. G. He, G. C. Joshi, H. Lew and R. R. Volkas, “NEW Z-prime PHENOMENOLOGY,” Phys. Rev. D **43**, 22-24 (1991)
- [30] X. G. He, G. C. Joshi, H. Lew and R. R. Volkas, “Simplest Z-prime model,” Phys. Rev. D **44**, 2118-2132 (1991)
- [31] W. Altmannshofer, S. Gori, S. Profumo and F. S. Queiroz, “Explaining dark matter and B decay anomalies with an $L_\mu - L_\tau$ model,” JHEP **12**, 106 (2016) [arXiv:1609.04026 [hep-ph]].
- [32] A. Kamada, K. Kaneta, K. Yanagi and H. B. Yu, “Self-interacting dark matter and muon $g - 2$ in a gauged $U(1)_{L_\mu - L_\tau}$ model,” JHEP **06**, 117 (2018) [arXiv:1805.00651 [hep-ph]].
- [33] P. Foldenauer, “Light dark matter in a gauged $U(1)_{L_\mu - L_\tau}$ model,” Phys. Rev. D **99**, no.3, 035007 (2019) [arXiv:1808.03647 [hep-ph]].
- [34] M. Escudero, D. Hooper, G. Krnjaic and M. Pierre, “Cosmology with A Very Light $L_\mu - L_\tau$ Gauge Boson,” JHEP **03**, 071 (2019) [arXiv:1901.02010 [hep-ph]].
- [35] K. Asai, S. Okawa and K. Tsumura, “Search for $U(1)_{L_\mu - L_\tau}$ charged dark matter with neutrino telescope,” JHEP **03**, 047 (2021) [arXiv:2011.03165 [hep-ph]].
- [36] D. Borah, M. Dutta, S. Mahapatra and N. Sahu, “Muon ($g - 2$) and XENON1T excess with boosted dark matter in $L_\mu - L_\tau$ model,” Phys. Lett. B **820**, 136577 (2021) [arXiv:2104.05656 [hep-ph]].

- [37] I. Holst, D. Hooper and G. Krnjaic, “Simplest and Most Predictive Model of Muon $g-2$ and Thermal Dark Matter,” *Phys. Rev. Lett.* **128**, no.14, 141802 (2022) [arXiv:2107.09067 [hep-ph]].
- [38] M. Drees and W. Zhao, “ $U(1)_{L\mu-L\tau}$ for light dark matter, $g_\mu - 2$, the 511 keV excess and the Hubble tension,” *Phys. Lett. B* **827**, 136948 (2022) [arXiv:2107.14528 [hep-ph]].
- [39] T. Hapitas, D. Tuckler and Y. Zhang, “General kinetic mixing in gauged $U(1)_{L\mu-L\tau}$ model for muon $g-2$ and dark matter,” *Phys. Rev. D* **105**, no.1, 016014 (2022) [arXiv:2108.12440 [hep-ph]].
- [40] P. Figueroa, G. Herrera and F. Ochoa, “Direct detection of light dark matter charged under a $L\mu-L\tau$ symmetry,” *Phys. Rev. D* **110**, no.9, 095018 (2024) [arXiv:2404.03090 [hep-ph]].
- [41] K. Asai, K. Hamaguchi, N. Nagata, S. Y. Tseng and J. Wada, “Probing the $L\mu-L\tau$ gauge boson at the MUonE experiment,” *Phys. Rev. D* **106**, no.5, L051702 (2022) [arXiv:2109.10093 [hep-ph]].
- [42] L. Zu, X. Pan, L. Feng, Q. Yuan and Y. Z. Fan, “Constraining $U(1)_{L\mu-L\tau}$ charged dark matter model for muon $g-2$ anomaly with AMS-02 electron and positron data,” *JCAP* **08**, no.08, 028 (2022) [arXiv:2104.03340 [hep-ph]].
- [43] R. Aliberti, T. Aoyama, E. Balzani, A. Bashir, G. Benton, J. Bijnens, V. Biloshytskyi, T. Blum, D. Boito and M. Bruno, *et al.* “The anomalous magnetic moment of the muon in the Standard Model: an update,” *Phys. Rept.* **1143**, 1-158 (2025) [arXiv:2505.21476 [hep-ph]].
- [44] D. P. Aguillard *et al.* [Muon $g-2$], “Measurement of the Positive Muon Anomalous Magnetic Moment to 0.20 ppm,” *Phys. Rev. Lett.* **131**, no.16, 161802 (2023) [arXiv:2308.06230 [hep-ex]].
- [45] D. P. Aguillard *et al.* [Muon $g-2$], “Detailed report on the measurement of the positive muon anomalous magnetic moment to 0.20 ppm,” *Phys. Rev. D* **110**, no.3, 032009 (2024) [arXiv:2402.15410 [hep-ex]].
- [46] G. W. Bennett *et al.* [Muon $g-2$], “Final Report of the Muon E821 Anomalous Magnetic Moment Measurement at BNL,” *Phys. Rev. D* **73**, 072003 (2006) [arXiv:hep-ex/0602035 [hep-ex]].
- [47] T. Aoyama, N. Asmussen, M. Benayoun, J. Bijnens, T. Blum, M. Bruno, I. Caprini, C. M. Carloni Calame, M. Cè and G. Colangelo, *et al.* “The anomalous magnetic moment of the muon in the Standard Model,” *Phys. Rept.* **887**, 1-166 (2020) [arXiv:2006.04822 [hep-ph]].
- [48] C. Davies, “Muon $g-2$,” *PoS LATTICE2024*, 019 (2025) [arXiv:2503.03364 [hep-lat]].
- [49] J. Aalbers *et al.* [LZ], “Dark Matter Search Results from 4.2 Tonne-Years of Exposure of the LUX-ZEPLIN (LZ) Experiment,” *Phys. Rev. Lett.* **135**, no.1, 011802 (2025) [arXiv:2410.17036 [hep-ex]].
- [50] R.L. Workman *et al.* (Particle Data Group), *Prog. Theor. Exp. Phys.* 2022, 083C01 (2022).
- [51] S. Balan, T. Bringmann, F. Kahlhoefer, J. Matuszak and C. Tasillo, “Sub-GeV dark matter and nano-Hertz gravitational waves from a classically conformal dark sector,” *JCAP* **08**, 062 (2025) [arXiv:2502.19478 [hep-ph]].
- [52] B. Holdom, “Two $U(1)$ ’s and Epsilon Charge Shifts,” *Phys. Lett. B* **166**, 196-198 (1986)
- [53] K. Schmitz, Kinetic Mixing in Field Theory (DESY Workshop Seminar, Winter Semester 2009/2010, 2009)

- [54] T. Gherghetta, J. Kersten, K. Olive and M. Pospelov, “Evaluating the price of tiny kinetic mixing,” *Phys. Rev. D* **100**, no.9, 095001 (2019) [arXiv:1909.00696 [hep-ph]].
- [55] F. Jegerlehner and A. Nyffeler, “The Muon $g-2$,” *Phys. Rept.* **477**, 1-110 (2009) [arXiv:0902.3360 [hep-ph]].
- [56] S. R. Mishra *et al.* [CCFR], “Neutrino Tridents and W Z Interference,” *Phys. Rev. Lett.* **66**, 3117-3120 (1991)
- [57] W. Altmannshofer, S. Gori, M. Pospelov and I. Yavin, “Neutrino Trident Production: A Powerful Probe of New Physics with Neutrino Beams,” *Phys. Rev. Lett.* **113**, 091801 (2014) [arXiv:1406.2332 [hep-ph]].
- [58] J. P. Lees *et al.* [BaBar], “Search for a muonic dark force at BABAR,” *Phys. Rev. D* **94**, no.1, 011102 (2016) [arXiv:1606.03501 [hep-ex]].
- [59] M. Bauer, P. Foldenauer and J. Jaeckel, “Hunting All the Hidden Photons,” *JHEP* **07**, 094 (2018) [arXiv:1803.05466 [hep-ph]].
- [60] H. K. Dreiner, J. F. Fortin, J. Isern and L. Ubaldi, “White Dwarfs constrain Dark Forces,” *Phys. Rev. D* **88**, 043517 (2013) [arXiv:1303.7232 [hep-ph]].
- [61] G. Bellini, J. Benziger, D. Bick, S. Bonetti, G. Bonfini, M. Buizza Avanzini, B. Caccianiga, L. Cadonati, F. Calaprice and C. Carraro, *et al.* “Precision measurement of the 7Be solar neutrino interaction rate in Borexino,” *Phys. Rev. Lett.* **107**, 141302 (2011) [arXiv:1104.1816 [hep-ex]].
- [62] N. Aghanim *et al.* [Planck], “Planck 2018 results. VI. Cosmological parameters,” *Astron. Astrophys.* **641**, A6 (2020) [erratum: *Astron. Astrophys.* **652**, C4 (2021)] [arXiv:1807.06209 [astro-ph.CO]].
- [63] J. Edsjo and P. Gondolo, “Neutralino relic density including coannihilations,” *Phys. Rev. D* **56**, 1879-1894 (1997) [arXiv:hep-ph/9704361 [hep-ph]].
- [64] D. G. Cerdeno, T. Delahaye and J. Lavalle, *Nucl. Phys. B* **854**, 738-779 (2012) [arXiv:1108.1128 [hep-ph]].
- [65] P. Gondolo and G. Gelmini, “Cosmic abundances of stable particles: Improved analysis,” *Nucl. Phys. B* **360**, 145 (1991).
- [66] K. C. Yang, “Freeze-out forbidden dark matter in the hidden sector in the mass range from sub-GeV to TeV,” *JHEP* **11**, 083 (2022) [arXiv:2209.10827 [hep-ph]].
- [67] E. W. Kolb and M. S. Turner, *The Early Universe* (Addison-Wesley, Redwood City, CA, 1990).
- [68] S. Vagnozzi, “New physics in light of the H_0 tension: An alternative view,” *Phys. Rev. D* **102**, no.2, 023518 (2020) [arXiv:1907.07569 [astro-ph.CO]].
- [69] E. Di Valentino, O. Mena, S. Pan, L. Visinelli, W. Yang, A. Melchiorri, D. F. Mota, A. G. Riess and J. Silk, “In the realm of the Hubble tension—a review of solutions,” *Class. Quant. Grav.* **38**, no.15, 153001 (2021) [arXiv:2103.01183 [astro-ph.CO]].
- [70] M. Kawasaki, K. Kohri and N. Sugiyama, “MeV scale reheating temperature and thermalization of neutrino background,” *Phys. Rev. D* **62**, 023506 (2000) [astro-ph/0002127].
- [71] R. Iengo, “Sommerfeld enhancement for a Yukawa potential,” [arXiv:0903.0317 [hep-ph]].

- [72] R. Iengo, “Sommerfeld enhancement: General results from field theory diagrams,” JHEP **05**, 024 (2009) [arXiv:0902.0688 [hep-ph]].
- [73] K. Abe *et al.* [Super-Kamiokande], “Indirect search for dark matter from the Galactic Center and halo with the Super-Kamiokande detector,” Phys. Rev. D **102**, no.7, 072002 (2020) [arXiv:2005.05109 [hep-ex]].
- [74] K. Frankiewicz, “Indirect Search for Dark Matter with the Super-Kamiokande Detector”, Ph.D. thesis, National Centre For Nuclear Research, Poland, Apr. 2018.
- [75] E. Richard *et al.* [Super-Kamiokande], “Measurements of the atmospheric neutrino flux by Super-Kamiokande: energy spectra, geomagnetic effects, and solar modulation,” Phys. Rev. D **94**, no.5, 052001 (2016) [arXiv:1510.08127 [hep-ex]].
- [76] S. Adrian-Martinez *et al.* [ANTARES], “Search of Dark Matter Annihilation in the Galactic Centre using the ANTARES Neutrino Telescope,” JCAP **10**, 068 (2015) [arXiv:1505.04866 [astro-ph.HE]].
- [77] C. A. Argüelles, A. Diaz, A. Kheirandish, A. Olivares-Del-Campo, I. Safa and A. C. Vincent, “Dark matter annihilation to neutrinos,” Rev. Mod. Phys. **93**, no.3, 035007 (2021) [arXiv:1912.09486 [hep-ph]].
- [78] R. Abbasi *et al.* [IceCube], “Search for GeV-scale Dark Matter from the Galactic Center with IceCube-DeepCore,” [arXiv:2511.00918 [astro-ph.HE]].
- [79] F. Bergsma *et al.* [CHARM], “Search for Axion Like Particle Production in 400-GeV Proton - Copper Interactions,” Phys. Lett. B **157**, 458-462 (1985)
- [80] M. W. Winkler, “Decay and detection of a light scalar boson mixing with the Higgs boson,” Phys. Rev. D **99**, no.1, 015018 (2019) [arXiv:1809.01876 [hep-ph]].
- [81] G. Bernardi, G. Carugno, J. Chauveau, F. Dicarolo, M. Dris, J. Dumarchez, M. Ferro-Luzzi, J. M. Levy, D. Lukas and J. M. Perreau, *et al.* “Search for Neutrino Decay,” Phys. Lett. B **166**, 479-483 (1986)
- [82] G. Bernardi, G. Carugno, J. Chauveau, F. Dicarolo, M. Dris, J. Dumarchez, M. Ferro-Luzzi, J. M. Levy, D. Lukas and J. M. Perreau, *et al.* “Anomalous Electron Production Observed in the CERN Ps Neutrino Beam,” Phys. Lett. B **181**, 173-177 (1986)
- [83] G. Bernardi, G. Carugno, J. Chauveau, F. Dicarolo, M. Dris, J. Dumarchez, M. Ferro-Luzzi, J. M. Levy, D. Lukas and J. M. Perreau, *et al.* “FURTHER LIMITS ON HEAVY NEUTRINO COUPLINGS,” Phys. Lett. B **203**, 332-334 (1988)
- [84] D. Gorbunov, I. Krasnov and S. Suvorov, “Constraints on light scalars from PS191 results,” Phys. Lett. B **820**, 136524 (2021) [arXiv:2105.11102 [hep-ph]].
- [85] A. V. Artamonov *et al.* [BNL-E949], “Study of the decay $K^+ \rightarrow \pi^+ \nu \bar{\nu}$ in the momentum region $140 < P_\pi < 199$ MeV/c,” Phys. Rev. D **79**, 092004 (2009) [arXiv:0903.0030 [hep-ex]].
- [86] E. Cortina Gil *et al.* [NA62], “Measurement of the very rare $K^+ \rightarrow \pi^+ \nu \bar{\nu}$ decay,” JHEP **06**, 093 (2021) [arXiv:2103.15389 [hep-ex]].
- [87] E. Cortina Gil *et al.* [NA62], “Search for π^0 decays to invisible particles,” JHEP **02**, 201 (2021)

- [arXiv:2010.07644 [hep-ex]].
- [88] J. Beacham, C. Burrage, D. Curtin, A. De Roeck, J. Evans, J. L. Feng, C. Gatto, S. Gninenko, A. Hartin and I. Irastorza, *et al.* “Physics Beyond Colliders at CERN: Beyond the Standard Model Working Group Report,” *J. Phys. G* **47**, no.1, 010501 (2020) [arXiv:1901.09966 [hep-ex]].
- [89] E. Cortina Gil *et al.* [NA62], “The Beam and detector of the NA62 experiment at CERN,” *JINST* **12**, no.05, P05025 (2017) [arXiv:1703.08501 [physics.ins-det]].
- [90] S. Alekhin, W. Altmannshofer, T. Asaka, B. Batell, F. Bezrukov, K. Bondarenko, A. Boyarsky, K. Y. Choi, C. Corral and N. Craig, *et al.* “A facility to Search for Hidden Particles at the CERN SPS: the SHiP physics case,” *Rept. Prog. Phys.* **79**, no.12, 124201 (2016) [arXiv:1504.04855 [hep-ph]].
- [91] C. Ahdida *et al.* [SHiP], “The experimental facility for the Search for Hidden Particles at the CERN SPS,” *JINST* **14**, no.03, P03025 (2019) [arXiv:1810.06880 [physics.ins-det]].
- [92] K. Bondarenko, A. Boyarsky, T. Bringmann, M. Hufnagel, K. Schmidt-Hoberg and A. Sokolenko, “Direct detection and complementary constraints for sub-GeV dark matter,” *JHEP* **03**, 118 (2020) [arXiv:1909.08632 [hep-ph]].
- [93] D. S. Akerib *et al.* [LZ], “Projected WIMP sensitivity of the LUX-ZEPLIN dark matter experiment,” *Phys. Rev. D* **101**, no.5, 052002 (2020) [arXiv:1802.06039 [astro-ph.IM]].
- [94] M. Cirelli, A. Strumia and J. Zupan, “Dark Matter,” [arXiv:2406.01705 [hep-ph]].
- [95] Y. Meng *et al.* [PandaX-4T], “Dark Matter Search Results from the PandaX-4T Commissioning Run,” *Phys. Rev. Lett.* **127** (2021) no.26, 261802 [arXiv:2107.13438 [hep-ex]].
- [96] E. Aprile *et al.* [XENON], “First Dark Matter Search with Nuclear Recoils from the XENONnT Experiment,” *Phys. Rev. Lett.* **131**, no.4, 041003 (2023) [arXiv:2303.14729 [hep-ex]].
- [97] D. N. Spergel and P. J. Steinhardt, “Observational evidence for selfinteracting cold dark matter,” *Phys. Rev. Lett.* **84**, 3760-3763 (2000) [arXiv:astro-ph/9909386 [astro-ph]].
- [98] S. Tulin, H. B. Yu and K. M. Zurek, “Beyond Collisionless Dark Matter: Particle Physics Dynamics for Dark Matter Halo Structure,” *Phys. Rev. D* **87**, no.11, 115007 (2013) [arXiv:1302.3898 [hep-ph]].
- [99] J. J. Sakurai, *Modern Quantum Mechanics* (Addison-Wesley, Reading, MA, 1994).
- [100] F. Kahlhoefer, K. Schmidt-Hoberg, M. T. Frandsen and S. Sarkar, “Colliding clusters and dark matter self-interactions,” *Mon. Not. Roy. Astron. Soc.* **437**, no.3, 2865-2881 (2014) [arXiv:1308.3419 [astro-ph.CO]].
- [101] B. Colquhoun, S. Heeba, F. Kahlhoefer, L. Sagunski and S. Tulin, “Semiclassical regime for dark matter self-interactions,” *Phys. Rev. D* **103**, no.3, 035006 (2021) [arXiv:2011.04679 [hep-ph]].
- [102] F. Kahlhoefer, K. Schmidt-Hoberg and S. Wild, “Dark matter self-interactions from a general spin-0 mediator,” *JCAP* **08**, 003 (2017) [arXiv:1704.02149 [hep-ph]].
- [103] C. A. Correa, “Constraining velocity-dependent self-interacting dark matter with the Milky Way’s dwarf spheroidal galaxies,” *Mon. Not. Roy. Astron. Soc.* **503**, no.1, 920-937 (2021) [arXiv:2007.02958 [astro-ph.GA]].
- [104] H. C. Turner, M. R. Lovell, J. Zavala and M. Vogelsberger, “The onset of gravothermal core collapse

- in velocity-dependent self-interacting dark matter subhaloes,” *Mon. Not. Roy. Astron. Soc.* **505**, no.4, 5327-5339 (2021) [arXiv:2010.02924 [astro-ph.GA]].
- [105] R. Dave, D. N. Spergel, P. J. Steinhardt and B. D. Wandelt, “Halo properties in cosmological simulations of selfinteracting cold dark matter,” *Astrophys. J.* **547**, 574-589 (2001) [arXiv:astro-ph/0006218 [astro-ph]].
- [106] L. Sagunski, S. Gad-Nasr, B. Colquhoun, A. Robertson and S. Tulin, “Velocity-dependent Self-interacting Dark Matter from Groups and Clusters of Galaxies,” *JCAP* **01**, 024 (2021) [arXiv:2006.12515 [astro-ph.CO]].
- [107] O. D. Elbert, J. S. Bullock, S. Garrison-Kimmel, M. Rocha, J. Oñorbe and A. H. G. Peter, “Core formation in dwarf haloes with self-interacting dark matter: no fine-tuning necessary,” *Mon. Not. Roy. Astron. Soc.* **453**, no.1, 29-37 (2015) [arXiv:1412.1477 [astro-ph.GA]].
- [108] T. Ren, A. Kwa, M. Kaplinghat and H. B. Yu, “Reconciling the Diversity and Uniformity of Galactic Rotation Curves with Self-Interacting Dark Matter,” *Phys. Rev. X* **9**, no.3, 031020 (2019) [arXiv:1808.05695 [astro-ph.GA]].
- [109] D. Harvey, R. Massey, T. Kitching, A. Taylor and E. Tittley, “The non-gravitational interactions of dark matter in colliding galaxy clusters,” *Science* **347**, 1462-1465 (2015) [arXiv:1503.07675 [astro-ph.CO]].
- [110] M. Bradac, S. W. Allen, T. Treu, H. Ebeling, R. Massey, R. G. Morris, A. von der Linden and D. Applegate, “Revealing the properties of dark matter in the merging cluster MACSJ0025.4-1222,” *Astrophys. J.* **687**, 959 (2008) [arXiv:0806.2320 [astro-ph]].
- [111] S. W. Randall, M. Markevitch, D. Clowe, A. H. Gonzalez and M. Bradac, “Constraints on the Self-Interaction Cross-Section of Dark Matter from Numerical Simulations of the Merging Galaxy Cluster 1E 0657-56,” *Astrophys. J.* **679**, 1173-1180 (2008) [arXiv:0704.0261 [astro-ph]].
- [112] H. Sieber, D. Banerjee, P. Crivelli, E. Depero, S. N. Gninenko, D. V. Kirpichnikov, M. M. Kirsanov, V. Poliakov and L. Molina Bueno, “Prospects in the search for a new light Z' boson with the NA64 μ experiment at the CERN SPS,” *Phys. Rev. D* **105**, no.5, 052006 (2022) [arXiv:2110.15111 [hep-ex]].
- [113] Y. Kahn, G. Krnjaic, N. Tran and A. Whitbeck, “ M^3 : a new muon missing momentum experiment to probe $(g - 2)_\mu$ and dark matter at Fermilab,” *JHEP* **09**, 153 (2018) [arXiv:1804.03144 [hep-ph]].
- [114] M. Cirelli, E. Del Nobile and P. Panci, “Tools for model-independent bounds in direct dark matter searches,” *JCAP* **10**, 019 (2013) [arXiv:1307.5955 [hep-ph]].
- [115] P. W. Graham, R. Harnik, S. Rajendran and P. Saraswat, “Exothermic Dark Matter,” *Phys. Rev. D* **82**, 063512 (2010) [arXiv:1004.0937 [hep-ph]].
- [116] J. Li, L. Su, L. Wu and B. Zhu, “Spin-dependent sub-GeV inelastic dark matter-electron scattering and Migdal effect. Part I. Velocity independent operator,” *JCAP* **04**, 020 (2023) [arXiv:2210.15474 [hep-ph]].
- [117] N. Anand, A. L. Fitzpatrick and W. C. Haxton, “Weakly interacting massive particle-nucleus elastic scattering response,” *Phys. Rev. C* **89**, no.6, 065501 (2014) [arXiv:1308.6288 [hep-ph]].

- [118] A. Y. Potekhin, A. F. Fantina, N. Chamel, J. M. Pearson and S. Goriely, “Analytical representations of unified equations of state for neutron-star matter,” *Astron. Astrophys.* **560**, A48 (2013) [arXiv:1310.0049 [astro-ph.SR]].
- [119] S. Goriely, N. Chamel and J. M. Pearson, “Further explorations of Skyrme-Hartree-Fock-Bogoliubov mass formulas. XII: Stiffness and stability of neutron-star matter,” *Phys. Rev. C* **82**, 035804 (2010) [arXiv:1009.3840 [nucl-th]].
- [120] N. B. Zhang and B. A. Li, “Constraints on the muon fraction and density profile in neutron stars,” *Astrophys. J.* **893**, 61 (2020) [arXiv:2002.06446 [astro-ph.HE]].
- [121] R. Garani, Y. Genolini and T. Hambye, “New Analysis of Neutron Star Constraints on Asymmetric Dark Matter,” *JCAP* **05**, 035 (2019) [arXiv:1812.08773 [hep-ph]].
- [122] J. L. Feng, J. Smolinsky and P. Tanedo, “Dark Photons from the Center of the Earth: Smoking-Gun Signals of Dark Matter,” *Phys. Rev. D* **93**, no.1, 015014 (2016) [erratum: *Phys. Rev. D* **96**, no.9, 099901 (2017)] [arXiv:1509.07525 [hep-ph]].
- [123] M. Blennow, S. Clementz and J. Herrero-Garcia, “Pinning down inelastic dark matter in the Sun and in direct detection,” *JCAP* **04**, 004 (2016) [arXiv:1512.03317 [hep-ph]].
- [124] J. Lundberg and J. Edsjo, “WIMP diffusion in the solar system including solar depletion and its effect on earth capture rates,” *Phys. Rev. D* **69**, 123505 (2004) [arXiv:astro-ph/0401113 [astro-ph]].
- [125] R. Garani and J. Heeck, “Dark matter interactions with muons in neutron stars,” *Phys. Rev. D* **100**, no.3, 035039 (2019) [arXiv:1906.10145 [hep-ph]].
- [126] T. Binder, L. Covi, A. Kamada, H. Murayama, T. Takahashi and N. Yoshida, “Matter Power Spectrum in Hidden Neutrino Interacting Dark Matter Models: A Closer Look at the Collision Term,” *JCAP* **11**, 043 (2016) [arXiv:1602.07624 [hep-ph]].
- [127] J. F. Navarro, C. S. Frenk and S. D. M. White, “A Universal density profile from hierarchical clustering,” *Astrophys. J.* **490**, 493 (1997) [astro-ph/9611107].
- [128] J. F. Navarro, C. S. Frenk and S. D. M. White, “The Structure of cold dark matter halos,” *Astrophys. J.* **462**, 563 (1996) [astro-ph/9508025].
- [129] G. Elor, N. L. Rodd and T. R. Slatyer, “Multistep cascade annihilations of dark matter and the Galactic Center excess,” *Phys. Rev. D* **91**, 103531 (2015) [arXiv:1503.01773 [hep-ph]].
- [130] K. C. Yang, “Search for Scalar Dark Matter via Pseudoscalar Portal Interactions: In Light of the Galactic Center Gamma-Ray Excess,” *Phys. Rev. D* **97**, no.2, 023025 (2018) [arXiv:1711.03878 [hep-ph]].
- [131] K. C. Yang, “Hidden Higgs portal vector dark matter for the Galactic center gamma-ray excess from the two-step cascade annihilation, and muon $g - 2$,” *JHEP* **08**, 099 (2018) [arXiv:1806.05663 [hep-ph]].
- [132] K. C. Yang, “A potentially detectable gamma-ray line in the Fermi Galactic center excess — in light of one-step cascade annihilations of secluded (vector) dark matter via the Higgs portal,” *JHEP* **07**, 148 (2020) [arXiv:2001.04946 [hep-ph]].

- [133] M. Maltoni, T. Schwetz, M. A. Tortola and J. W. F. Valle, “Status of global fits to neutrino oscillations,” *New J. Phys.* **6**, 122 (2004) [arXiv:hep-ph/0405172 [hep-ph]].
- [134] S. Palomares-Ruiz and S. Pascoli, “Testing MeV dark matter with neutrino detectors,” *Phys. Rev. D* **77**, 025025 (2008) [arXiv:0710.5420 [astro-ph]].
- [135] Y. Ashie *et al.* [Super-Kamiokande], “A Measurement of atmospheric neutrino oscillation parameters by SUPER-KAMIOKANDE I,” *Phys. Rev. D* **71**, 112005 (2005) [arXiv:hep-ex/0501064 [hep-ex]].